Making Semiconductor Single Photon Emitters Faster and Brighter

by

Brandon Demory

A dissertation submitted in partial fulfillment
of the requirements for the degree of
Doctor of Philosophy
(Electrical Engineering)
in the University of Michigan
2017

Doctoral Committee:

Associate Professor Pei-Cheng Ku, Co-Chair
Associate Professor Hui Deng, Co-Chair
Assistant Professor Julie Biteen
Professor L. Jay Guo
Professor Theodore Norris

Brandon J. Demory
bdemory@umich.edu
ORCID iD: 0000-0002-9674-958X

This thesis is dedicated to my family, friends, cohort, and all those who inspired me along the way to keep going.

Acknowledgements

I would like to thank my research adviser, Professor Pei-Cheng (P.C.) Ku for giving me an opportunity to pursue my doctoral studies under his guidance. The opportunity to work on the three fronts of a project, simulation, fabrication, and experimental measurements, is invaluable. I appreciate the guidance and support provided along the way, while you constantly pushed me to be my best and put my best foot forward.

In addition, to my co-adviser Professor Hui Deng, thank you for the outside perspective on my engineering work. You always made sure that I understood the concepts and physics behind the work. I was fortunate to have two great advisers in my corner.

I would also like to thank my wife, Danielle and my family for always being there for me. Your countless calls of support and encouragement are what allowed me to get through the difficult thought exercises or the long nights in the lab. Even though we were in different states, it felt like you were by my side. I am forever thankful to have such a great support network I can call on at any time.

Lastly, I would like to thank my friends and my cohort. The transition to graduate school and full time research over the last few years was not trivial. Having people who could show me the ropes and teach me all of the things outside of the books was priceless. Thank you Michael, Chih-Wei, Chu-Hsiang, Jingyang, and Yao Hong for always keeping our office a friendly space. Thank you Heather for helping me with course work along the way. Thank you Forest for being there for me outside of the classroom. And to the countless others, thank you for your contribution to my degree progress, whether it was academic, extracurricular, or professional. You all helped me get here to this point.

Table of Contents

List of Figures

Abstract

Single photon emitters are critical resources for quantum science and technologies. More specifically, on-demand single-photon emission (SPE) from semiconductor quantum dot (QD) structures is crucial for quantum cryptography and low-power communications. Group III-nitride (III-N) QDs are a high interest QD solution because of their potential for SPE beyond cryogenic temperatures, enabling a more practical system. However, in contrast to the III-arsenic QDs which possess a radiative lifetime typically <1ns, the operating speed for isolated III-N QDs is limited to only tens of megahertz, due to the strong piezoelectric field in strained III-N heterostructures, causing longer radiative lifetimes on the order of tens of nanoseconds. Coupling the emission from III-N QD structures to an optical cavity such as a photonic crystal or a metallic cavity can reduce the radiative lifetime and simultaneously improve the emission intensity. For shorter wavelength III-N QDs, a metallic cavity is a better enhancement solution than a dielectric cavity because of the large fabrication tolerance, broad spectral enhancement window, and reduced fabrication complexity. In addition to improving the emission process,

increasing the extraction efficiency of generated photons is desired for device integration. Light extraction from semiconductor QDs is limited by the high index contrast between the air and the semiconductor. Moreover, the far field emission pattern of the exiting emission is broad and not ideal for further optical coupling. Integrating lenses and reflectors with the QD structure increases the emission extraction efficiency and condenses the far field pattern, creating a more ideal far field pattern for optical coupling into an optical waveguide.

In this work, our aim is to develop conventional methods for improving semiconductor QDs' speed and brightness by taking advantage of wafer-scale fabrication techniques. First, a self-aligning silver film cavity was investigated for enhancement of the spontaneous emission from III-N QDs. Using e-beam evaporation, the silver film encased the QD pillar without additional post processing. With the appropriate film thickness, the silver localized surface plasmon resonance is tuned to overlap the QD emission wavelength. Optical spectroscopy measurements of the QDs before and after the cavity showed an order of magnitude reduction in the emission lifetime, simultaneously coupled with an order of magnitude increase in the emission intensity. Additionally, the QDs become uniform in quantum efficiency from the improved radiative process caused by the high cavity quantum efficiency. Next, we demonstrate through similar optical

spectroscopy measurements on a dense array of QDs, that emitter lifetimes on the order of tens of picoseconds can be achieved by changing the geometry of the silver film cavity and removing the top of the silver film.

To improve the QD light extraction efficiency and light collection, an integrated parabolic nano lens and reflector system was designed. The SiN integrated optics resulted in a four to six times improvement in the collectable emission compared to the bare QD pillar, with ~80% of the far field emission pattern within the 0.5NA zone, which is more ideal for waveguide coupling. Furthermore, the same lens is applied to a multicolor GaN/InGaN light-emitting diode (LED), improving the light extraction efficiency to 70% across the visible spectrum. Lastly, we propose in future work a multi-layered open top cavity structure capable of reducing the emitter lifetime below 10 picoseconds. These results contribution to the foundations for room temperature, high speed, directional, on-chip, single photon emitters.

Chapter 1

Introduction

Single photon emitters are critical resources for quantum science and technologies. More specifically, on-demand single-photon emission (SPE) from semiconductor quantum dot (QD) structures is crucial for quantum cryptography and low-power communications [1]. Compared to a variety of single-photon emitter materials including atomic systems [2], molecules [3], trap ions, colloidal QDs [4, 5], and nitrogen vacancies in diamonds [6, 7], epitaxially grown semiconductor QDs intrinsically offer a higher repetition rate [8, 9], which is a desirable criteria for high-speed operations. Group III-nitride (III-N) QDs are a high interest QD solution because of their potential for SPE beyond the cryogenic temperature range [8-11], enabling a more practical system. However, in contrast to the III-arsenic QDs which possess a radiative lifetime typically <1ns, the operating speed for isolated III-N QDs is limited to only tens of megahertz, due to the strong piezoelectric field in strained III-N heterostructures, causing longer radiative lifetimes on the order of tens of nanoseconds [12]. The radiative lifetime issue can be

addressed by increasing the emitter's local density of states (LDOS), reducing the radiative lifetime. Coupling the emission from III-N QD structures to an optical cavity such as a photonic crystal [13-15] or a metallic cavity [16-18] has previously been demonstrated to increase the LDOS, reduce the radiative lifetime, and simultaneously improve the emission intensity. For our shorter wavelength III-N QDs, a metallic cavity is a better enhancement solution than a photonic crystal cavity because a photonic crystal cavity has small fabrication tolerances [14, 15, 19], a narrow spectral enhancement window [20], and increased fabrication complexity. Thus, a metallic cavity solution was chosen and studied in this work to overcome these issues.

In this thesis, my aim two-fold: to modify and enhance III-N semiconductor QD and QD light-emitting diode (LED) emission by exploiting the emitter-plasmon interactions through the localized surface plasmon resonance of metallic nanostructures, and to improve the emission extraction efficiency and condense the far field emission patterns into smaller numerical apertures using integrated lenses and reflectors. With these fundamental improvements, semiconductor based single photon sources (SPSs) will be one-step closer to realization and practical applications.

In this Chapter, I will start my discussion with an overview of III-N QDs properties in section 1.1. Next, I will give an overview on localized surface plasmons in section 1.2;

the geometric and material dependence of the plasmon resonance frequency in section 1.3; then its effect on the optical properties of the emitter including intensity, lifetime, and efficiency in section 1.4; lastly shaping the far field in section 1.5. To summarize, I will briefly conclude and outline this thesis in section 1.6.

1.1 Overview of III-Nitride Quantum Dots

III-N semiconductor QDs have garnered interest, due to their potential for operation outside of cryogenic temperatures. Unlike III-arsenic or III-P semiconductor QDs, III-N QDs have large exciton binding energies. This is due mainly to the small dielectric constant ϵ_s. For the bulk GaN material, ϵ_s is approximately 5.3, which is approximately a factor of two less than InP (9.6) or GaAs (10.9). From the inverse squared relationship between the exciton binding energy and the dielectric constant, the reduced dielectric constant results in a four to five times larger exciton binding energy for GaN, of about 26-28-meV. This value is larger than the room temperature thermal energy (kT energy), which is 25.7-meV, indicating that the excitons are stable at room temperature. The large exciton binding energy combined with large QD-barrier band offsets in III-N QDs, making them a promising solution for cryo-free operation [21]. For our InGaN QDs, single photon emission has been recorded up to 90K thus far [21]. However, room

temperature (300K) single photon emission has been demonstrated in 2014 in GaN QDs [10] and in InGaN/GaN QDs [22].

1.1.1 III-Nitride Emission Wavelength

The tertiary III-N compound, InGaN, allows for a tunable direct bandgap across the visible spectrum. Unlike the III-Ar or III-P materials, which are limited from about red to infrared emission wavelengths, $In_xGa_{(1-x)}N$ can generate from ultraviolet to infrared wavelength emission. As the indium concentration is increased, the emission wavelength is red-shifted towards the InN bandgap. This is very useful as it is compatible with conventional silicon avalanche photo diodes (APDs) used for detection of visible emission, and it can be used for creating semiconductor devices that are compatible with visible spectrum, such as displays.

1.1.2 Origin of the Long Lifetimes

III-Nitride QDs have long radiative recombination lifetimes due to the piezoelectric field in the material. The piezoelectric field modifies the bandgap, tilting the band structure. The effect is called the quantum-confined Stark effect (QCSE). Normally, for a typical QD or quantum well structure without the QCSE, the band diagram along the

crystal axis is flat. The electron and hole wave functions are confined to the center of the band valley, and their wave function overlap is large. However, with the QCSE, which is present in III-Nitride structures due to the compressive strain in the InGaN [23], the electron and hole wave functions become spatially separated. The spatial separation reduces the wave function overlap, which increases the radiative recombination lifetime. In addition, this changes the effective bandgap of the material, resulting in a longer emission wavelength. Engineering the strain in InGaN/GaN QD nanopillars for optoelectronic applications has been investigated extensively in our group [21, 23-26].

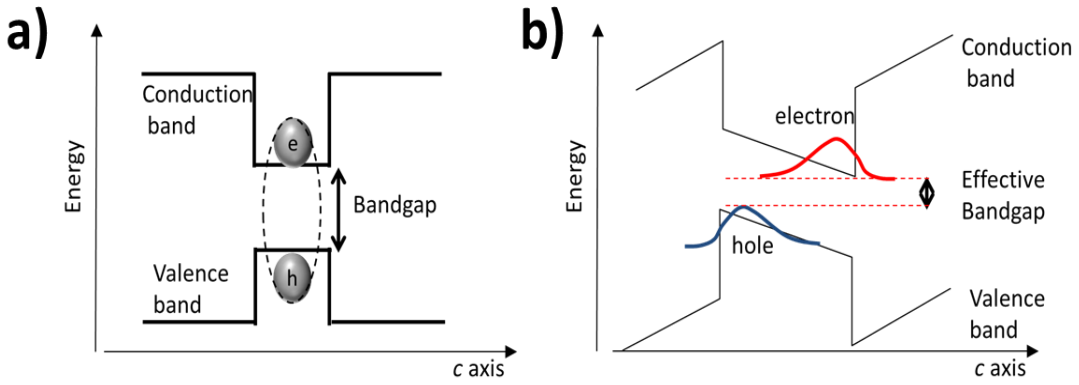

Figure 1-1 Band diagrams for typical semiconductor tertiary structures. (a) Band diagram for a standard QD structure. The electron and holes are well confined in the active region and have strong interaction due to the large overlap. (b) The tilted band diagram due to the QCSE in InGaN/GaN QDs. The electron and hole wave functions are spatially separated, which weakens their interaction, causing the longer radiative lifetime. The effective bandgap is also smaller than the actual material bandgap.

1.2 Overview of Localized Surface Plasmons

Metallic nanostructures have been investigated extensively because of their ability to strongly interact with electromagnetic radiation. The sea of free electrons allows metals to resonate upon the proper electromagnetic excitation. Localized surface plasmons (LSPs) are an example of this resonance. LSPs are non-propagating excitations of the electrons in the conduction band of the metal due to an electromagnetic field [27]. LSPs are a derivative of the scattering of radiation off a sub-wavelength conductive object. The resonance depends on the magnitude of the driving field force on the electrons and the geometrically dependent restoring force in the particle. This resonance, known as the localized surface plasmon resonance (LSPR), leads to field amplification both inside and outside of the particle surface [27]. The geometric dependence of LSPs allows for direct light excitation and does not require phase matching techniques that are necessary for Surface Plasmon Polariton excitation. Another benefit of the geometrical dependence is the tunability of LSPs [28, 29], which will be explained in more details later. The applications of LSPs are vast and include nano-antennas [30, 31], emission enhancement of a nearby emitter [32-34], and low threshold lasers [35]. Each of these applications takes advantage of the high field enhancements generated near the metallic particles. The tunability of the resonance condition of LSPs makes them a prime candidate of

investigation for coupling photons from emitters to produce enhanced emission. While several reports have investigated coupling between emitters and metallic particles, the experimental setup is often complex and involves metal particles on probes. Integration of the metal particle with the emitter into a device is the groundwork for creating fast on-chip emitters.

1.3 Polarizability of a Spherical Particle

The LSPR is dependent upon the object shape, material composition, and local environment. The resulting resonance wavelength condition, enhancement and loss magnitudes, and the number of resonances from the structure are directly affected by these components. This will be shown directly from the formulas below.

LSPR is a direct consequence of Maxwell's equations and the complex dielectric response of metal. For a spherical particle placed in a constant electric field, the solution for the Electric potential $\emptyset$ can be computed analytically. From the resulting potentials, the electric field E inside and outside of the particle can be derived using $\boldsymbol{E} = -\nabla\phi$.

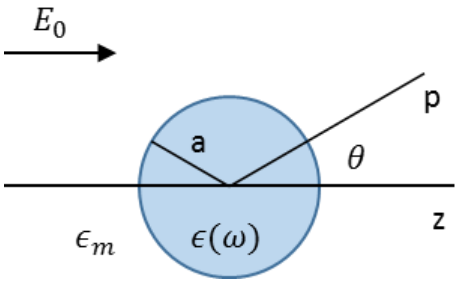

Figure 1-2 Homogeneous sphere placed into a constant Electric field, E_0. The sphere has a radius 'a' and dielectric constant $\epsilon(\omega)$ in a surrounding medium with dielectric constant ϵ_m. The induced dipole moment **p**, is at an angle θ measured from the z-axis.

The resulting potentials are of the following form:

$$\emptyset_{in} = -\frac{3\epsilon_m}{\epsilon(\omega)+2\epsilon_m} E_0 \cos\theta \qquad (1\text{-}1)$$

$$\emptyset_{out} = -E_0\, r \cos\theta + \frac{\boldsymbol{p}\cdot\boldsymbol{r}}{4\pi\epsilon_0\epsilon_m r^3} \qquad (1\text{-}2)$$

$$\boldsymbol{p} = \epsilon_0\epsilon_m\alpha\boldsymbol{E}_0 \qquad (1\text{-}3)$$

$$\alpha = 4\pi a^3 \frac{\epsilon(\omega)-\epsilon_m}{\epsilon(\omega)+2\epsilon_m} \qquad (1\text{-}4)$$

The potential outside of the sphere resembles a superposition of an applied field with a dipole source located at the center of the particle [27]. Defining the second term of $\emptyset_{out}$ in terms of a dipole moment inside of a sphere and introducing the polarizability α, we arrive at the polarizability equation. The polarizability exhibits a resonance when the denominator $|\epsilon(\omega)+2\epsilon_m|$ reaches a local minimum, which reduces to $Re[\epsilon(\omega)] = -2\epsilon_m$, for a small or slowly changing $Im[\epsilon(\omega)]$. This condition is called the Fröhlich condition [27]. At that condition, the induced dipole in the sphere, **p**, which depends on the polarizability and the external electric field, theoretically approaches infinity, which

translates to the resonance of the particle. The polarizability parameter, α, allows for many degrees of freedom in choosing the resonance wavelength based on the composition of the environment and the spherical particle. Resonance across the visible spectrum is achieved using different metallic nanoparticles [29, 36].

1.3.1 Optical Properties of Resonant Spheres

Due to the polarizability of a particle, it may scatter and absorb radiation with an effective cross section much larger than the cross section of the particle itself. For a particle, the scattering cross section C_{scat} and absorption cross section C_{abs} are given as $C_{scat} = \frac{k^4}{6\pi}|\alpha|^2$ and $C_{abs} = kIm[\alpha]$, respectively with $C_{ext} = C_{scat} + C_{abs}$ [37]. The Extinction cross section can be calculated independently as

$$C_{ext} = \frac{9\omega}{c}\epsilon_m^{\frac{3}{2}} V * \frac{\epsilon_2}{[\epsilon_1 + 2\epsilon_m]^2 + \epsilon_2^2} \qquad (1\text{-}5)$$

with $\epsilon(\omega) = \epsilon_1 + \epsilon_2$. Again, the surrounding medium is very important for determining the resonance peak. For a sphere with polarizability α from equation (1-4), scattering is maximized at the resonance condition $Re[\epsilon(\omega)] = -2\epsilon_m$. Although the analytical formulas above are specific for a spherical geometry, the extinction cross section can be modified with any shape geometry.

1.3.2 Material Dependent Resonance Tunability

In the polarizability equation (1-4), the resonance condition, $Re[\epsilon(\omega)] = -2\epsilon_m$ is dependent on the dielectric constant of the metal and the surrounding medium [28]. Therefore, gold, silver, chrome, silica, or glass spheres in the same environment would all exhibit different peak wavelengths in the extinction cross section, due to the different frequency dependent dielectric behavior. In Figure 1-3, as the dielectric constant of the environmental medium is increased, the resonance wavelength of the silver nanoparticle is red-shifted. Point a is in air, and the points labeled b are in an indexed matched oil of n=1.44. For each successive line under point b, the index of the fluid is increased by 0.04. The same sphere placed in different dielectric mediums will exhibit different LSPRs, due to the dependence on the medium in the polarizability equation. These are vital components for choosing the proper metal material for the wavelength range of interest [29].

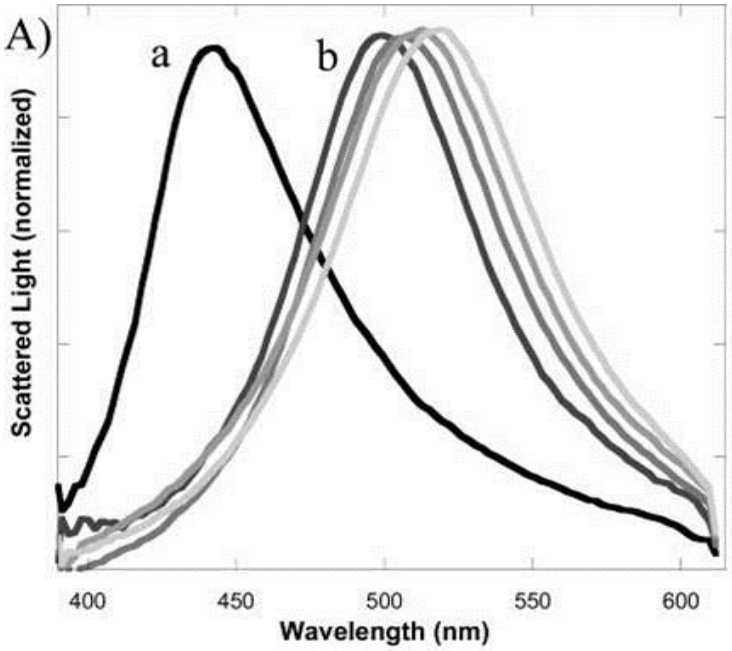

Figure 1-3 Spectral shift for individual (roughly spherical) silver nanoparticles. The particle spectrum is shown as it is shifted from (a) air to (b) 1.44 index oil, and successive oil treatments in 0.04 index incremental increases [29].

1.3.3 Geometric Dependence of Resonance Wavelength

The geometric shape of the particle influences the resonance wavelength. Several geometric shapes, including rods, cones, triangle, bowties, pentagons, etc. have been widely studied for their different responses from spherical particles [28, 30, 31, 36]. Figure 1-4 shows an example of the geometric dependence of the silver resonance wavelength. The same material is able to achieve different resonances across the visible spectrum due to the shape. Larger spherical particles, where the quasi-static approximations start to break down, have more terms in the polarizability and affect the

spectral location of the resonance [27, 37]. The main effect for Drude and noble metals i.e. (Gold and Silver), is that the resonance wavelength is red-shifted with increasing size. This fact is important for tuning the resonance in cavity structures shown in later chapters as the structures are on the order of 100's of nm.

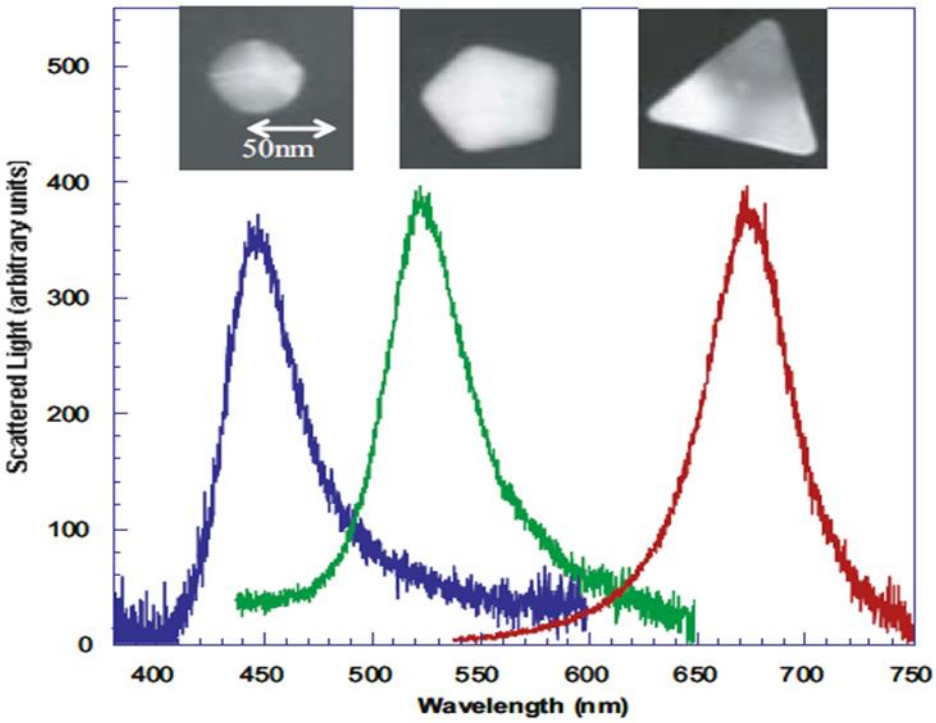

Figure 1-4 Scattering spectra of single silver nanoparticles in the shape of a circle, pentagon, and triangle, measured in a dark-field configuration [28].

1.3.4 Multi-Layered Shells and Elliptical Shells

In addition to the material and geometric dependence, the polarizability can be engineered using metallic shell layers on dielectric cores. This introduces hybrid

electron-hole oscillations resulting in two modes of different frequencies [38]. The equation for the polarizability of a two-layer sphere composed of a dielectric core and metallic shell is given by

$$\alpha = 4\pi a_2^3 \frac{(\epsilon_2(\omega)-\epsilon_m)(\epsilon_1+2\epsilon_2(\omega))+f(\epsilon_1-\epsilon_2(\omega))(2\epsilon_2(\omega)+\epsilon_m)}{(\epsilon_2(\omega)+2\epsilon_m)(\epsilon_1+2\epsilon_2(\omega))+2f(\epsilon_1-\epsilon_2(\omega))(\epsilon_2(\omega)-\epsilon_m)} \qquad (1\text{-}6)$$

where $\epsilon_2(\omega)$, ϵ_1, $and\ \epsilon_m$ are the permittivity of the metal shell, dielectric core, and surround medium respectively. The particle radius is a_2, and the fill factor 'f' is the ratio of the volume of the inner sphere to the outer sphere. A fill factor of zero is a solid sphere or the same material in the core and shell layers ($\epsilon_1 = \epsilon_2$). When the fill factor is zero, equation (1-6) reduces to the well-known polarizability equation (1-4) described in Chapter 1.3. The additional degree of freedom in the fill factor allows for a broader resonance tuning capability. The denominator contains multiple terms with more degrees of freedom, such that multiple solutions satisfy the resonance condition, resulting in multiple resonances for the same structure. This hybridization of resonances is similar to spin degeneracy splitting of energy levels [39]. The lowest energy resonance is the strongest and is red shifted in wavelength as shown in the schematic in Figure 1-5. Using metallic shells instead of solid metallic particles can exhibit resonances red-shifted significantly from their solid spherical counterparts, enabling resonances across the visible spectrum.

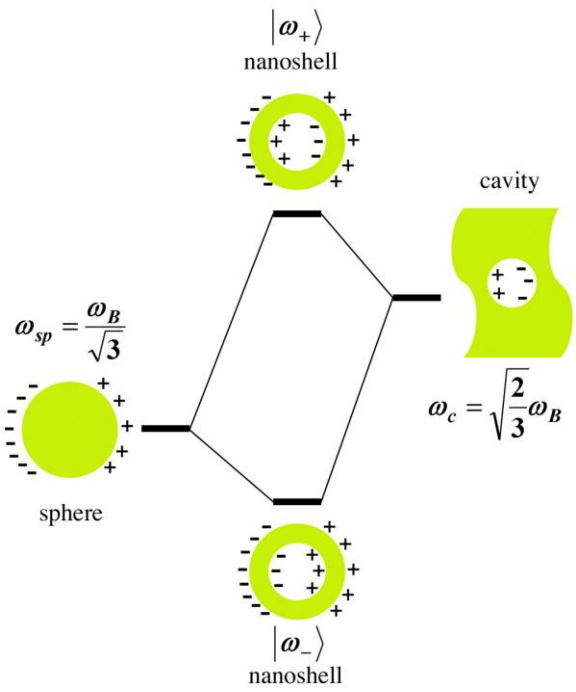

Figure 1-5 An energy-level diagram showing the plasmon hybridization in metal nanoshell structures. The resulting two states are interaction between the solid sphere mode and the cavity void mode. The symmetric state is the lowest energy state and the antisymmetric state is the highest energy state [39].

The polarizability of particle shapes that deviate from the spherical geometry can be calculated by taking into account the geometrical factor of the shape [28, 37]. An ellipse, for example, will have different resonances for the major and minor axis. Shapes that are more complicated may require numerical calculations for the polarizability but follow the same aforementioned trends as spherical particles.

1.4 Coupling between Emitters and Localized Plasmons

In order to understand how an emitter is affected by a metallic structure nearby, we study how the emission is changed with a change in the local environment. An emitter has a spontaneous emission rate in free space, denoted as γ_{free}. When that same emitter is placed in a different environment, such as a different material with a different dielectric constant, a cavity structure, or near a mirror reflector, the spontaneous emission rate is changed. The new spontaneous emission rate, γ_{new}, is related to the original spontaneous emission rate by the Purcell factor, F_p [40], through the equation $\frac{\gamma_{new}}{\gamma_{free}} = F_p$, where

$$F_p = \frac{3\lambda^3 Q}{4\pi^2 V} \qquad (1\text{-}7)$$

The Purcell factor depends on the material dependent emission wavelength λ, where $\lambda = (\lambda_c/n)$, the Quality factor Q, which is a measure of the resonance's bandwidth to center frequency, and the modal volume V, which measures the volume of the emission mode. Since the wavelength is typically fixed, the Q/V ratio determines the magnitude of the Purcell factor and the spontaneous emission rate enhancement. Thus, a large Purcell factor is needed to create a large spontaneous emission rate enhancement.

In addition to a change in the spontaneous emission rate, which is directly related to the emitter decay rate or total lifetime, there are changes in the emission intensity from the emitter as well. When a metallic particle is brought in proximity to an emitter, there

are three variables which affect the change in the fluorescence: excitation rate, emitter quantum efficiency (QE), and collection efficiency [33]. The collected emission from the emitter by the observer is the product of those three terms,

$$S^{em} = \gamma^{exc} * \eta * \xi \qquad (1\text{-}8)$$

The fluorescence change can be engineered through controlling the effect of the three variables.

1.4.1 Spontaneous Emission Enhancement

The excitation rate in the emission equation is the driving field seen by the emitter, and it is proportional to the dipole moment and the electric field around the emitter, $\gamma_0^{exc} \propto \left|\vec{p} \cdot \vec{E}_0\right|^2$. In the presence of a scattering object, the local electric field is a sum of the incident field and the scattered field, $E_{tot} = E_0 + E_s$. Hence, the excitation rate of a dipole in the presence of a scatterer is given by

$$\gamma^{exc} \propto \left|\vec{p} \cdot \left[\vec{E}_0(\omega_1) + \vec{E}_s(\omega_1)\right]\right|^2 \qquad (1\text{-}9)$$

where ω_1 is the excitation frequency. For metallic particles, it has been shown that at resonance, large field enhancements can be achieved near the surface of a particle or particle couple such as a dimer [28-31, 34, 41-43]. Placing the emitter in that area will increase the excitation rate of the dipole as described above [44]. As the dipole emitter

sees a larger driving electric field, it will produce a larger oscillation, which results in more emission intensity S^{em}.

The decay rate of the dipole, of which the spontaneous emission rate is a factor, is a function of the local density of states (LDOS). The total decay rate is given by $\gamma_{tot} = \gamma_0 + \gamma_{NR}$, where γ_0 is the original radiative decay rate or spontaneous emission rate and γ_{NR} is the intrinsic non-radiative decay rate for the emitter. In the absence of a scatterer, such as a metallic particle, the LDOS is solely a material property. The dispersion curve for a dielectric material is given by $\omega = \frac{c}{n}k$, where ω is the light frequency, c is the speed of light, n is the index of refraction of the medium, and k is the wave vector. When a metal particle is introduced, the LDOS is modified by the introduction of new decay channels into the metallic particle [27]. The two new channels, radiative and non-radiative, given by the rates γ_{rad} & γ_{abs} respectively, alter the original radiative decay rate of the dipole, γ_0. The new radiative rate is given by $\gamma_{rad} = F_p * \gamma_0$ [40], and the new total decay rate is $\gamma_{tot}^{new} = \gamma_{rad} + \gamma_{abs} + \gamma_{NR}$. Radiative enhancement or quenching of the rate is determined by dipole and metal particle orientation [41-43]. Proper orientation of the emitter with respect to the metallic particle is necessary to achieve large decay rate enhancements.

The emitter QE is the ratio of the radiative decay rate to the total decay rate of the

emitter [4].

$$\eta = \frac{\gamma_{rad}}{\gamma_{tot}} \tag{1-10}$$

It measures how efficiently excited electron-hole pairs recombine to emit photons. For an emitter with an initial QE of one, every excited electron-hole pair will emit one photon. In this case, a metal particle in the vicinity of the emitter will always lower the QE, as metallic particles have their own non-radiative decay channels through absorption. However, for emitters like our III-N QD pillars formed from top-down dry etching, where the initial QE is less than 1, due to some initial intrinsic non-radiative decay channels via defect and surface recombinations, coupling to LSPR of the metal particle can actually raise the QE of the emitter if the Purcell factor is large enough. In this case, improving the QE will result in more collectable emission S^{em}.

The collection efficiency measures the percentage of the total collectable emission within a given collection direction and angle. During the actual measurement of the QDs, we typically sample a small percentage of the emission in a given angle and direction. Higher numerical aperture collection lenses will increase the amount of emission collected in one direction, but without an integrating sphere setup, emission going in other directions will not be collected. Therefore, the collection efficiency is always less than or equal to unity. The total emission into the collection direction must be increased

to improve the collection efficiency of the system while only measuring from one direction. Emission can be increased by placing a mirror or reflector behind the emitter plane to redirect more emission into the collection direction. The emission from the QD does not change, but the emission in the collection direction increases. Thus, the total emission S^{em} as measured by the observer is increased. Similarly, we can use a metal scatterer in proximity of the QD emitter to change the direction of the emission and the far field distribution; so that, in the exact same setup with and without the scatterer, the collection efficiency will be improved with the scatterer present [45, 46].

The emission intensity enhancement or fluorescence enhancement is measured using the ratio, S^{em}/S_0^{em} with and without the metal structure [33]. There are several ways to improve the emission intensity: enhance the driving field seen by the emitter, improve the QE of the emitter, or adjust the emission in the far field as described above. Up to this point, we have considered a generic metal scatterer or cavity structure as the way of modifying these parameters. In order to achieve the excitation enhancement and QE enhancement, we must first optimize the metal scatterer to produce those effects at the correct wavelength. Poor optimization of the antenna quantum efficiency (AQE) of the metal scatterer could lead to emission quenching.

1.4.2 Antenna Efficiency of Coupling

The antenna efficiency or cavity AQE is a measure of how much the system prefers to radiate. Within a metallic structure, the excited oscillating electrons of a localized surface plasmon can either emit a photon at the resonance wavelength (radiation) or recombine in an intraband or interband transition with no emission (absorption) [27]. Radiation is the source of the radiative decay rate enhancement. As more of the enhancement is due to the radiative channel instead of the non-radiative channel, the structure is said to have higher AQE. The equation for the AQE is,

$$\eta_a = \gamma_{rad}/(\gamma_{rad} + \gamma_{abs}) \tag{1-11}$$

which is given by the ratio of the enhanced radiative decay rate to the sum of the enhanced radiative decay rate and enhanced absorption rate of the structure. This efficiency does not take into account the intrinsic non-radiative decay rate, γ_{NR}, as it is only a function of the cavity and not the emitter. This equation shows that structures with high decay rate enhancements (Purcell factors) or low decay rate enhancements can have the same AQE. With the equation for the initial emitter QE,

$$\eta_0 = \frac{\gamma_{rad0}}{\gamma_{rad0}+\gamma_{NR}} \tag{1-12}$$

the equation for the final emitter QE with a cavity structure,

$$\eta = \frac{\gamma_{rad}}{\gamma_{rad}+\gamma_{abs}+\gamma_{NR}} \tag{1-13}$$

and the antenna efficiency η_a, we can find the emitter QE ratio. The emitter QE ratio

$$\frac{\eta}{\eta_0} = \frac{1}{\frac{1-\eta_0}{F_p}+\frac{\eta_0}{\eta_a}} \tag{1-14}$$

is a function of the AQE and Purcell factor. For an emitter with an initial QE of one, the emitter QE ratio reduces to η_a and the final QE is just the AQE. If the Purcell factor is large enough such that $(1-\eta_0) \ll F_p$, then the final QE reduces to the AQE as well. Thus, if the AQE is higher than the initial QE and the Purcell factor is large enough, we can achieve an emitter QE ratio greater than one, indicating improvement in the QE of the system. This is why high AQE is a critical design factor and highly desired for our design.

1.4.3 Optimizing Emission Enhancement

The excitation enhancement and QE enhancement are dependent on three key factors: the overlap of the LSPR wavelength with the emission wavelength, the dipole orientation with respect to the metal structure, and the distance between the dipole and the metal structure. Each factor additionally affects the AQE directly. Choosing an emitter that emits within the resonance wavelength maximizes the decay rate enhancement. Operating off resonance has minimal interaction between the localized surface plasmon and the photon from the dipole. The emitter QE in equation (1-14) is

maximized by optimizing the Purcell factor and the AQE. There is a tradeoff between these two parameters **as generally a higher Purcell factor leads to lower AQE**. The inverse relationship is explained mostly by the increase in the radiative enhancement and absorption losses with decreasing distance between the emitter and the metal cavity. The exact relationship also depends on the metal structure geometry and material composition.

The orientation of the emitter with respect to the structure plays a large role in the resonance condition. This has been widely studied with spherical particles and dimers [42, 43]. The emission from one dipole orientation can be suppressed while the perpendicular orientation can be enhanced. This is analogous to how propagating surface plasmons are supported by TM modes instead of TE modes. Proper alignment is important for optimizing the AQE.

Lastly, the electric field enhancement due to a metallic structure is maximized near the surface and decays with distance away from the structure. Similarly, the excitation enhancement for the incident electric field acting on an emitter is maximized as the emitter is brought closer to the metal surface. However, bringing the emitter infinitely close to the metal structure quenches the emission and rapidly reduces the AQE [47]. This has been demonstrated with a dipole and a metallic sphere [33].

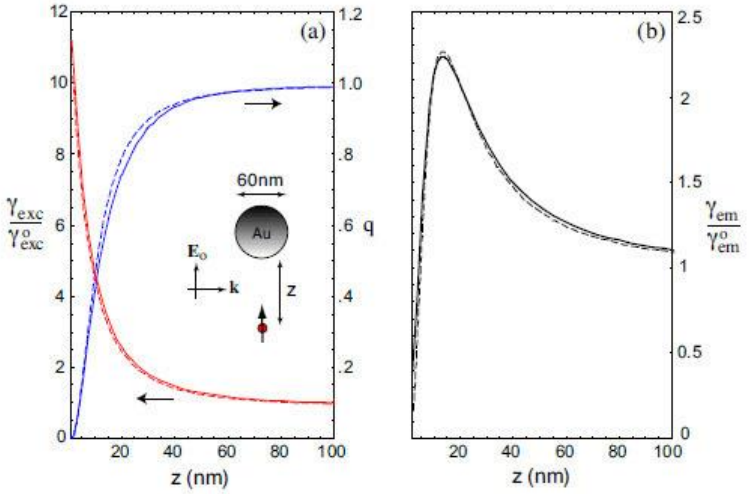

Figure 1-6 Fluorescence enhancement near a 60-nm gold particle excited by a 650-nm wavelength dipole. The plot shows a) the Quantum yield or QE in blue and the excitation rate enhancement in red. b) Emission enhancement versus dipole distance to metal particle. The emission wavelength and excitation wavelength are assumed the same. Here, the solid curves are exact solutions based on the MMP method and the dashed curves are approximations [33].

As the dipole is moved closer to the metal particle, the excitation enhancement continues to increase, due to the enhanced local electric field. However, the QE decreases due to the increased absorption from the particle. The Purcell factor increases, but after a point the majority of emission is lost to absorption, so there is significantly less collectable signal and the emission enhancement drops rapidly. Therefore, a balance must be achieved between Purcell factor or fluorescence enhancement and AQE in order to retain collectable emission.

The relationships between the variables of the emission enhancement equation require careful tuning of the structural properties of the metallic cavity. This section explains the complex nature of the relationship between emission enhancement, excitation enhancement, and decay rate enhancement. In order to demonstrate the effectiveness of our cavity structures, we have to design the experiment in a way such that we can determine how each part of the equation is affected. The experimental design for this is explained in Chapter 2.

1.5 Controlling the Emission in the Far Field

Up to this point, we have considered the three components of the emitter emission equation, the excitation, the QE, and the collection efficiency. A metallic cavity or scatterer can improve these values to result in more emission or emission enhancement from the emitter. However, once the emission is generated, we need a way to couple it to collection optics or subsequent waveguides with minimal losses to future proof the device for single photon communications.

At the macro scale, lenses and mirrors are common optics components used for controlling emission direction, shaping beams, and collimating emission for coupling between components [48, 49]. As long as the focal length of a positive lens is known, it

can be used to focus light to a point, or collimate light from a point source located at the focal point.

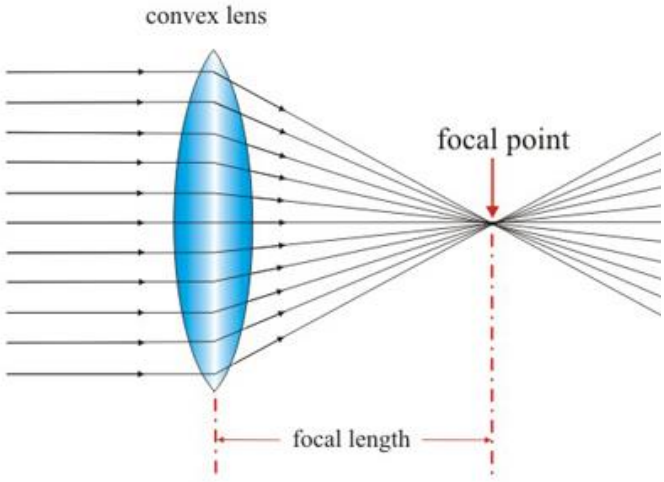

Figure 1-7 Ray tracing diagram of a convex (positive) lens showing collimated light focuses at the focal point of the lens located a distance equal to the focal length from the center of the lens. Due to time reversal symmetry, light originating from the focal point would be collimated by the lens.

A specific reflector type of interest is a parabolic shape, due to its focusing properties. Like a spherical structure as shown in Figure 1-7, a parabolic reflector will collimate light originating at its focal point, but with reduced spherical aberration. A parabolic reflector with collimate the light from a point source better than a spherical reflector.

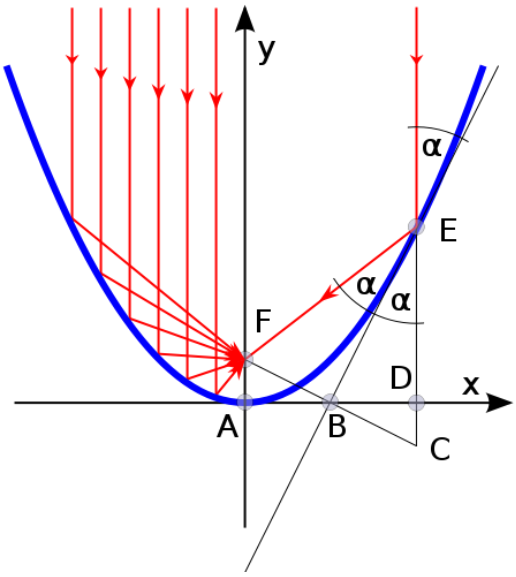

Figure 1-8 A ray tracing diagram for a parabolic reflector. Collimated rays are focus to the focal point F, regardless of where they intersect the parabola.

The concept of the lens and reflector can be shrunk down to the micron and nanometer length scale. These parabolic lenses can be integrated on top the emitter structure to collimate emission exiting from the top surface [50, 51]. Simultaneously, a reflector can be placed at the bottom surface of the structure to redirect emission towards the lens, essentially doubling the light output [52, 53]. The other benefit of the parabolic structure is due to the curved shape. The light rays hitting the parabolic interface with the air are perpendicular to the lens's curved surface, aiding with light extraction [54]. This is an advantage over the planar surface interface, as the high index of refraction limits the natural acceptance cone for light rays to leave the material into the air, resulting in most of the light being in total internal reflection. Combining these optical structures with our

semiconductor emitters will help to improve light extraction efficiency. However, working at these length scales, we must engineer ways to overcome the fabrication challenges of lens emitter alignment and making parabolic shapes. Chapter 5 will explain the solutions to these issues.

1.6 Thesis Overview

This thesis focuses on manipulating the geometry of GaN/InGaN nanopillar emitters and silver films in order to exploit the LSPR properties of the structures. In addition, by introducing nanolens optics and reflectors, the light extraction from these nanopillars can be improved for both electrical and optical applications. The thesis is organized as follows: Chapter 1 introduces the III-N QDs, the concepts of the localized surface plasmon resonance wavelength, coupling between metallic structures and emitters, and using nano lenses to improve light extraction. Chapter 2 proposes the closed top silver film cavity, from its simulation, to fabrication and experimental demonstration. It also demonstrates cavity coupled single photon emission and explains the calculations for the experimental Purcell factor. Chapter 3 introduces the rotational deposition technique, the resonance wavelength matched emitter-cavity system, and the QE calculation. This creates the foundation for the open top cavity calculations. Chapter 4 proposes the open

top silver film cavity structure that can generate radiative decay rate enhancements of ~1000x, effectively homogenizing the QE of an array of QDs. The procedure for fabricating the cavity structure using a wafer scale process and its experimental measurements are also explained here. Chapter 5 demonstrates the improvement in the emission intensity into the far field with the integration of micron scale parabolic lenses on top of the nano pillar emitters. Using a resist reflow and dry etching process, parabolic lenses are formed in a dielectric layer covering the nanopillars resulting in a ~6x intensity improvement in the 0.5NA collection zone. Chapter 6 concludes the thesis, laying the foundation for some future work for cavity emitter coupling, including the alternating layer metallic-dielectric open top cavity, which has similar expected radiative decay rate enhancement to the open top silver cavity, but with higher AQE and lower losses.

Chapter 2

Plasmonic Enhancement of Single Photon Emission from Site-Controlled GaN/InGaN Quantum Dots

2.1 Introduction

As percentage of the world's population using the internet and communication devices steadily increases, vast amounts of data needs to be communicated efficiently, quickly, and securely. Whether across a computer chip or around the globe, the photon has proven itself as formidable information carrier, due to its efficiency and data capacity. The quantum nature of photons is an added benefit that has been explored, in the laboratory, to show secure communications [55-57] and quantum information processing ability [55, 58-60]. The efficiency of switching light at the single photon level can lower the energy requirements for information exchange. Hence, the road to advancing photon communications is ensuring the efficient generation, processing, and receiving of single photons.

Semiconductor QDs are desirable single photon emitters due to the potential for electrical modulation and integration with existing electronic and optoelectronic components. Group III-N QDs are of high interest because of their potential for SPE beyond the cryogenic temperature range [10, 11]. While major advances have been made in III-N QD processing and fabrication, photon polarization control [26], and achieving operational temperatures near room temperature [10, 11, 22], III-N QDs still suffer from the issue of low radiative recombination rates (< 1GHz). For applications such as Quantum Key Distribution (QKD), data rates of at least 1-10Gbps are desirable [58]. In addition, to generate indistinguishable single photons, it is required that the radiative lifetime T_1 be less than the emitter dephasing time T_2 [58, 61], which decreases rapidly with increasing temperature. In order to address the long radiative lifetime issue associated with III-N QDs, coupling the QDs to a cavity is investigated.

In this chapter, the results of a silver film cavity coupled to InGaN/GaN QD are presented. Using a silver film cavity, the average lifetime reduction and emission intensity enhancement factors for the QDs were found to be 15 and 10.9, respectively. The enhancement in the lifetime and intensity are due to coupling to the localized surface plasmon as illustrated by the contrasting results with the aluminum cavity film. Finally, enhanced single photon emission is measured from a QD coupled to the silver film

cavity.

2.2 The Plasmonic Nano-Cavity Advantage

When coupling a QD to a cavity, dielectric optical cavities [14, 62] and plasmonic nano-cavities [7, 63] are typically investigated for enhancing the spontaneous emission rate from the dipole emitter. For an emitter with a linewidth less than the cavity linewidth, the Purcell factor of the cavity enhances the radiative decay rate. In order to achieve the picosecond time scale or tens of GHz repetition rate, for a typical III-N emitter with a lifetime of ~1ns, a Purcell factor of about 100 – 1000 is needed. In equation (1-7), for a specific material and wavelength, the Q/V ratio determines the magnitude of F_p. Dielectric optical cavities, due to the physical constraint on the optical modal volume V by the diffraction limit, rely on large Q factors in order to achieve large Purcell factors. Whereas, plasmonic nano-cavities take advantage of the ultra-small modal volume from plasmonic confinement in order to generate a large Purcell factor.

With an optical cavity, increasing the Q factor to drive large enhancement results in challenging spatial alignment and spectral alignment, as the cavity bandwidth becomes narrower and the enhancement bandwidth window shrinks. Contrarily, with a plasmonic nano cavity, the spectral enhancement bandwidth is larger for a given Purcell factor

compared to a dielectric cavity, due to the lower Q factor given that spatial alignment is maintained in the system.

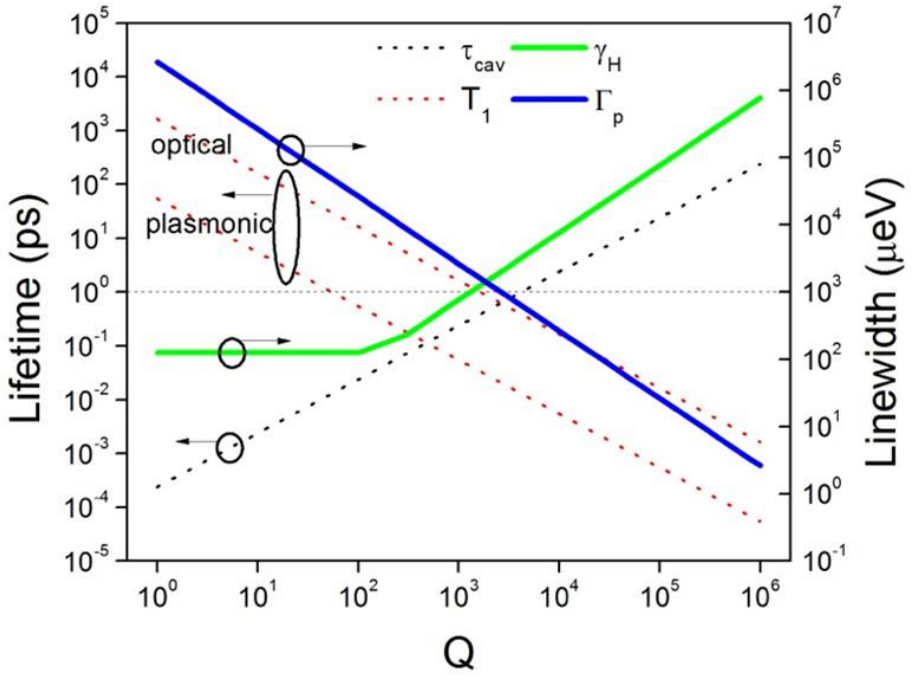

Figure 2-1 The relationship between the radiative lifetime T_1, cavity photon lifetime τ_{cav}, homogeneously broadened linewidth γ_H, and cavity linewidth Γ_p as functions of the cavity Q factor. Two mode volumes are considered: $(\lambda/2n)^3$ and $(\lambda/6n)^3$ for optical and plasmonic cavities, respectively. The horizontal 1-ps line indicates the goal lifetime. The intersection of the red T_1 curves and the 1-ps line represent the lowest Q allowed. The red curve must intersect the 1-ps line first before any other lines from the left side. Otherwise, the minimum cavity T_1 will be greater than 1ps.

As demonstrated in Figure 2-1, there are several physical advantages of the metallic nano-cavity. First, the magnitude of the Q factor necessary to achieve the picosecond

lifetime range is much less than the optical cavity, which means that the spectral enhancement window is larger. This is important because the entire emitter linewidth much fit within the cavity linewidth. Second, at that lower Q factor value, the cavity linewidth is larger than the emitter linewidth; so, the entire emitter spectrum is enhanced. Lastly, the photon cavity lifetime is shorter than the emitter lifetime. This ensures that all the emitted photons have exited the cavity before the next emitted photon, reducing the chance for reabsorption, stimulated emission, or other strong coupling regime effects. For the Q factor necessary in the dielectric cavity case, we are operating much closer to the regime in which the above stated conditions are not true. Thus, for reaching this high enhancement goal and beyond, the plasmonic nano-cavity is the optimum choice.

2.2.1 InGaN/GaN Quantum Dot Structures

The plasmonic resonances of the conventional metals used in plasmonic coupling typically fall between the ultraviolet and the visible wavelength range [64]. To ensure spectral overlap between the QD and the cavity, nitride semiconductors were explored as the optimal candidates. They have direct bandgaps from 0.7 – 6.2 eV, and tunable alloys allow us to work in the visible range to match silver or gold resonances very well. Thus, InGaN/GaN semiconductor QDs were chosen for this work.

The InGaN/GaN QDs were fabricated using a top down approach. An InGaN single quantum well wafer capped with GaN was epitaxially grown by metal-organic chemical vapor deposition (MOCVD) on (0001) sapphire. First, a 1.5-μm thick GaN layer was grown on the sapphire substrate. Then, a single 3-nm InGaN quantum well was grown and capped with a 10-nm thick GaN layer. All layers were unintentionally n-typed doped at a concentration of approximately 3 x 10^{16} (cm^{-3}). The emission wavelength of the wafer was 470nm. Next, the pillar diameters and positions were defined and patterned using the JEOL JBX-6300FS E-beam lithography tool with PMMA 950 A2 resist. A Chrome hard mask of 60 – 80-nm was deposited after development of the PMMA. It is an etching mask for the dry etching of GaN using inductively coupled plasma reactive ion etching (ICP-RIE). Dry etching creates the nano-pillar structure with the InGaN QD. Lastly, the remaining Cr hard mask was removed using the Chrome etchant Cr-14. A cross section schematic of the fabrication process is shown below in Figure 2-2.[1]

[1] Fabrication of the QDs was performed by Chu-Hsiang Teng.

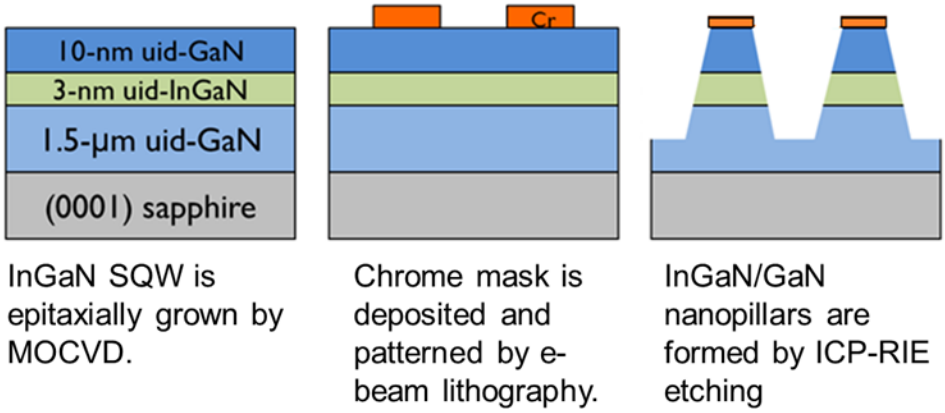

Figure 2-2 Schematic of the InGaN/GaN nano-pillar fabrication procedure. The diameter of the Chrome cylinder determines the top pillar diameter. The pillars taper at a 72° angle due to the etching chemistry.

The epitaxial stack creates the confinement in the vertical direction, while the air/InGaN interface generates the lateral confinement for the excitons through strain relaxation [65]. More detailed studies of the QD pillars including the fabrication procedures, optical properties, and verification of single photon emission by second order correlation measurements can be found in Lee [65] and Zhang [21, 23, 24]. The size and dimensions of the nano-pillars used were characterized by scanning electron microscope (SEM). Our fabrication technique allows for tunable pillar diameters; however, for this experiment, pillars with a QD diameter of ~28-nm and a height of 135-nm were used. Figure 2-3(b) shows an SEM image of an ordered array of 28-nm diameter QD pillars used in this experiment. The fabrication procedure results in ordered and uniform QDs.

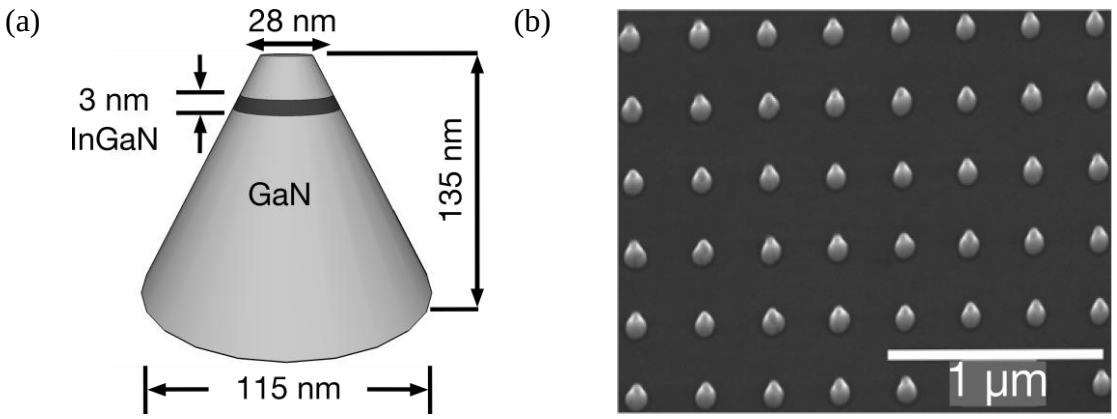

Figure 2-3 QD pillar geometry. (a) Schematic of the QD pillar dimensions used for this experiment. The QD diameter is 28-nm. (b) SEM image of a dense array of 28-nm QD diameter pillars with 300-nm spacing. The dots are ordered and uniform for locating the same QD at different measurements [66].

2.3 The Silver Film Closed Top Cavity Design

The silver cavity was designed using a conformal layer coating of the pillar structures. Silver film coatings have been studied before to enhance the emission from Quantum Wells (QWs) including InGaN QWs [67, 68]. The layered film approach was chosen instead of an antenna structure as the enhancement mechanism due to the fabrication challenges of positioning the antenna close enough to the QD layer. Another advantage is that the film layer would self-align to the pillar structure using conventional e-beam evaporation techniques, so there is no concern about the QD dimension or position being an issue. A dielectric spacer layer between the pillar and the silver film was also included in the design as an extra layer to help tune the cavity absorption loss.

Since the QW wafer has an emission wavelength of about 470-nm, the silver film cavity was designed to have a resonance wavelength within the window of 400-nm- 500-nm. The QD pillars emit at a shorter wavelength than the wafer due to the strain relaxation effect, so the cavity design was tweaked accordingly.

2.3.1 Cavity Simulation Calculated Parameters

Lumerical FDTD Solutions was used to design and simulate the silver film cavity structure [69]. A dipole source was used to represent the QD emission at the center of the QD cylindrical layer. In Lumerical, the ratio of the power radiated by the dipole source in different environments is equivalent to the ratio of the decay rates in the two environments, as given by $\frac{P}{P_0} = \frac{\gamma^{tot}}{\gamma_0^{tot}}$ [32]. All decay rates are normalized by the nominal decay rate for a dipole in the constant dielectric material it is placed [69], which in this case is InGaN with an assumed index of refraction of 2.51. Therefore, we can compare the effect of the cavity structure on the radiative decay rate, by comparing the dipole's radiated power in the two simulations: the pillar structure with and without the cavity layers.

The AQE of the cavity structure was calculated by measuring the power radiated from the dipole in the cavity simulation and comparing that to the power that makes it

past the cavity structure into the far field. This is done by placing a box around the dipole within the pillar and placing a box outside of the pillar and silver cavity. These monitor boxes calculate the power that crosses through them. The fraction of the power that makes it to the outer box, which is the far field, is the AQE for the cavity.

The total decay rate enhancement is calculated by taking the dipole power ratio between the two simulations. This total enhancement is the sum of the radiative decay rate enhancement or Purcell factor and the enhanced absorption rate due to the cavity γ_{abs}. Calculating the fraction of the power that makes it outside of the structure and dividing by the radiated power in the control simulation, gives the Purcell factor of the cavity. Here, we assume in the control simulation that the decay rate is purely radiative, in order to simplify the calculation. Because the actual QD pillar does have intrinsic non-radiative decay channels, more calculations must be done to compare the experimental lifetime changes to the simulated decay rate changes directly.

The collection efficiency is calculated from the far-field projection of the fields above the pillar. A collection aperture whole angle of 70° is assumed due to the NA of the lens in the experimental setup. The ratio of the power in the experimental collection aperture of 70º to the total power above the structure in a 180° angle in the far-field is the collection efficiency. To calculate this, a power monitor is placed above the pillar and

cavity structure than spans across the entire simulation cell and the near fields, $\vec{E}$ and $\vec{H}$, are measured. From $\vec{E}$ and $\vec{H}$ near-fields on the monitor, the far field projection is calculated [69]. The collection efficiency for the two structures is calculated, and the ratio of the collection fraction in the cavity simulation to the collection fraction in the control simulation, ξ/ξ_0, is the collection efficiency enhancement. Note, that this is an experimental setup parameter, as using different NA lenses will change the collection aperture angle. So, while the collection efficiency enhancement does not affect the decay rates, it will affect the collectable emission and the experimentally measured emission intensity enhancement.

The excitation enhancement is the local $\vec{E}$ field enhancement at the QD due to the laser excitation on the sample. Due to the metal cavity surround the QD pillar, there will be an enhancement in the local $\vec{E}$ field seen by the QD with the same incident laser power on the sample without the metal layer. This enhancement is a function of the driving laser wavelength and the pillar geometry. In our experimental setup, a 390-nm wavelength femtosecond pulsed laser with a spot focused of 30-μm, incident at a 55° angle from normal incidence is used to excite the QDs. To simulate this laser's local $\vec{E}$ field at the QD, we used a 390-nm plane wave source at the corresponding angle. A plane wave approximation was used due to the size of the QD being ~1000 times smaller than

the laser spot size. The electric fields were recorded and the intensity for both simulations were calculated. Comparing the local field intensity at the QD in the cavity and the QD without a cavity, the resulting excitation enhancement due to the 390-nm wavelength driving laser was 20.1 times.

With the Purcell factor, AQE, collection efficiency, and excitation enhancement simulated, the emission intensity enhancement can be plotted for different initial QD quantum efficiencies using the equation,

$$\frac{S^{\mathrm{em}}}{S_0^{em}} = \frac{\xi}{\xi_0} * \frac{\gamma^{exc}}{\gamma_0^{exc}} * \frac{1}{\frac{1-\eta_0}{F_p}+\frac{\eta_0}{\eta_a}} \qquad (2\text{-}1)$$

substituting (1-14) into (1-8). Since the initial QD QE is unknown, this is a fitting parameter to the experimental data.

2.3.2 The Aluminum Oxide and Silver Cavity

For the cavity simulation, silver was used as the metal layer due to its plasmon resonance proximity to the emission wavelength. Johnson and Christy data was used to model the silver permittivity [64]. Aluminum oxide (Al_2O_3) was used as the spacer layer due to the availability of conformal deposition using atomic layer deposition (ALD) in our fabrication facility with the Oxford ALD tool. The index of refraction for our Al_2O_3 was measured to be n= 1.66 through ellipsometry, which was used in the simulations. The

GaN and InGaN layers were treated to have an index of refraction of 2.4 and 2.51, respectively in the simulation. The pillar height was 135-nm, the top diameter 25-nm, and the QD diameter was 28-nm.

The starting point for the simulations was a 20-nm layer of Al_2O_3 and a 30-nm silver film thickness. This spacer thickness gives a reasonable amount of clearance between the emitter and the metal to minimize the quenching effects. The resulting structure resembles a core-shell particle. The X-Z cross section is in Figure 2-4.

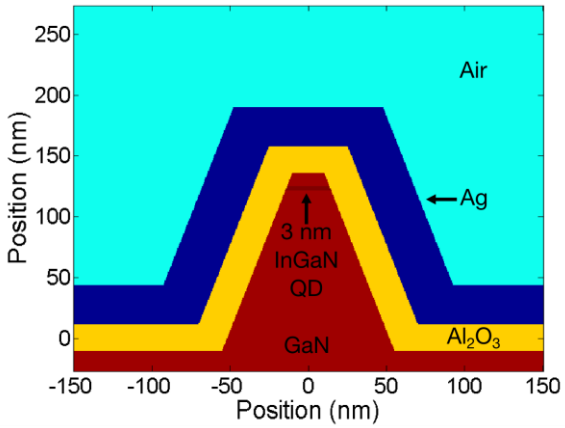

Figure 2-4 The X-Z cross section of the silver cavity with the Al_2O_3 spacer. The top diameter is 25-nm, the Al_2O_3 spacer thickness is 20-nm, and the Ag film thickness is 30-nm. The location of the InGaN QD is indicated near the top of the GaN pillar. The cavity is radially symmetric [66].

With a core-shell structure, there is hybridization of the LSPR mode [70], resulting in a splitting of the resonance into two at different wavelengths [39, 71]. The high-energy

resonance is due to an oscillation across the core within the inner surface of the metal shell [39]. In this structure, this results in a surface plasmon at the Ag-Al_2O_3 layer interface, which can be confirmed by solving for the plasmon wavelength from the dispersion relation of a surface plasmon polariton at the interface between a metal and a dielectric using the Ag parameters and the Al_2O_3 index of 1.66. The solution surface plasmon wavelength is approximately 390-nm, which agrees well with the high-energy peak in Figure 2-5(a). In addition, we can see it does not change much with metal thickness, which is because the inner metal distance to the QD does not change. The low-energy resonance peak is a result of the oscillation across the outer shell surface. This is the lowest order mode of oscillation and has the broader of the two peaks.

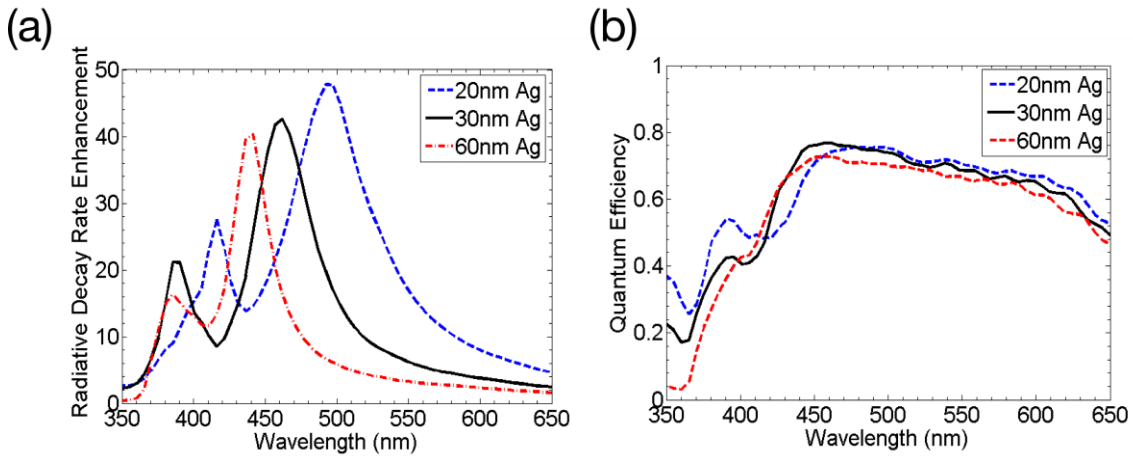

Figure 2-5 Simulated radiative decay rate enhancement or Purcell factor for silver thicknesses of 20, 30, and 60-nm. The resonance peak of the cavity blue shifts as the silver thickness is increased. (b) Cavity AQE of the decay rate enhancement for silver thicknesses of 20, 30, and 60-nm. The values are the fraction of the total decay rate

enhancement that is due to radiative enhancement. The lower-energy resonance always has higher QE [66].

From this starting point, we varied the metal thickness to see the effect on the resonance wavelength, the Purcell factor, and AQE. By increasing the Ag film thickness from 20-nm to 60-nm, the low-energy resonance is blue shifted towards the high-energy resonance peak. In the limit as the metal thickness approaches infinity, the two resonances converge to a single resonance for a metallic void, which should fall in between the two split resonances [39]. As the metal becomes thicker, the wavelength shift of the resonance peak is about 60-nm and the Purcell factor is relatively constant, as it only decreases by about 10%. Around 450-nm wavelength, the cavity has a high AQE of about 70% −80%, which shows that most of the enhancement from this cavity is radiative. Here, the Al_2O_3 layer was included in the control simulation. Its effect on the Purcell factor is about a factor of two; so, if we compared the bare pillar to the cavity coated pillars, the Purcell factor is about 2 times as large as reported in Figure 2-5.

In addition to metal thickness, we varied the spacer dielectric thickness to understand its effect on the Purcell factor, AQE, and resonance wavelength. In these simulations, since the spacer layer is varied, it is not included in the control simulation. Therefore, in Figure 2-6(a), for the 20-nm spacer thickness and 30-nm Silver thickness,

the Purcell factor is about two times the value (~80) reported in Figure 2-5(a) (~40), although it is the same structure.

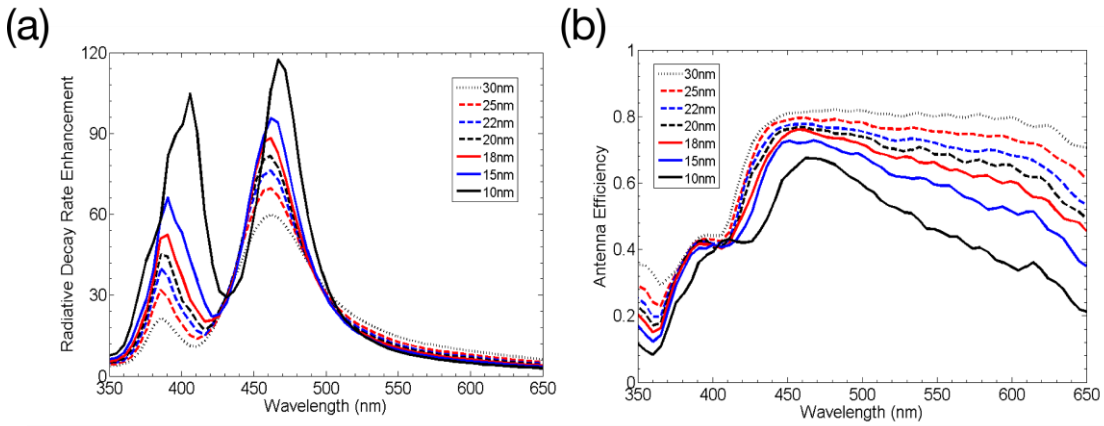

Figure 2-6 Simulated radiative decay rate enhancement or Purcell factor for varying Al_2O_3 spacer thicknesses and a constant silver thicknesses of 20-nm. The resonance peak of the cavity red shifts slightly as the oxide thickness is decreased. (b) Cavity AQE of the decay rate enhancement for varying Al_2O_3 thicknesses from 10-nm to 30-nm. The values are the fraction of the total decay rate enhancement that is due to radiative enhancement. The lower-energy resonance efficiency increases as the spacer thickness increases.

As the oxide thickness is decreased, the Purcell factor increases, due to the reduced thickness between the metal and the QD. In addition, there is a slight red shift in the resonance wavelength as the spacer thickness decreases, due to the increase in the effective index of the core. If we treat the structure with the core-shell approximation, decreasing the spacer thickness increases the effective index of the core, as the ratio of Al_2O_3 to InGaN is dropping. This effect is balanced by the fact that decreasing the radius

also blue shifts the resonance wavelength. Therefore, the resulting wavelength shift is very small, and most of the spacer thicknesses have the same resonance wavelength.

As the spacer thickness is reduced from 20-nm to 10-nm, the Purcell factor is increased by almost 50%. The drawback to the thinner spacer is the reduction in AQE. To ensure that we have a high enough QE enhancement, the 20-nm thick spacer was chosen for the experiment with the 30-nm thick silver film.

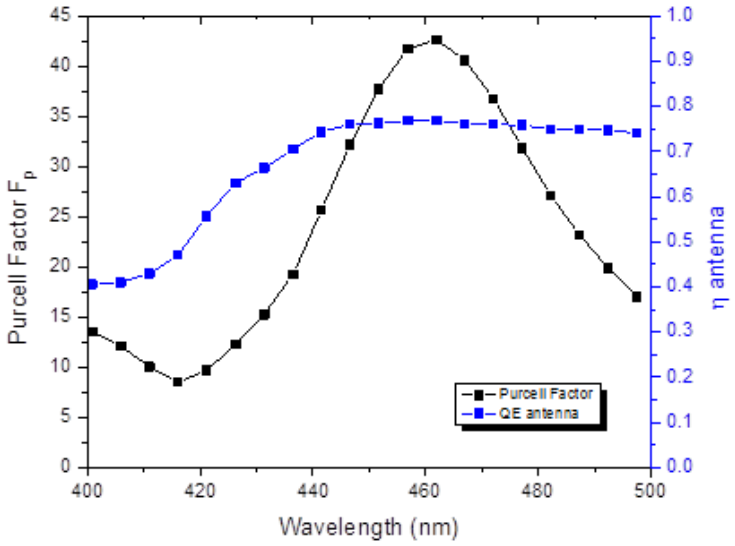

Figure 2-7 Simulated radiative decay rate enhancement or Purcell factor and AQE for the 20-nm thick Al_2O_3 spacer and 30-nm thick Silver cavity on a 25-nm diameter QD. The resonance peak is at about 465-nm wavelength and the corresponding AQE is >70%.

Using the cavity design specifications, the excitation intensity enhancement and

collection efficiency enhancement were calculated. The excitation intensity enhancement for the 390-nm wavelength laser and cavity with these film thicknesses was 20.1 times. The collection efficiency enhancement ratio was calculated per wavelength and is plotted in Figure 2-8.

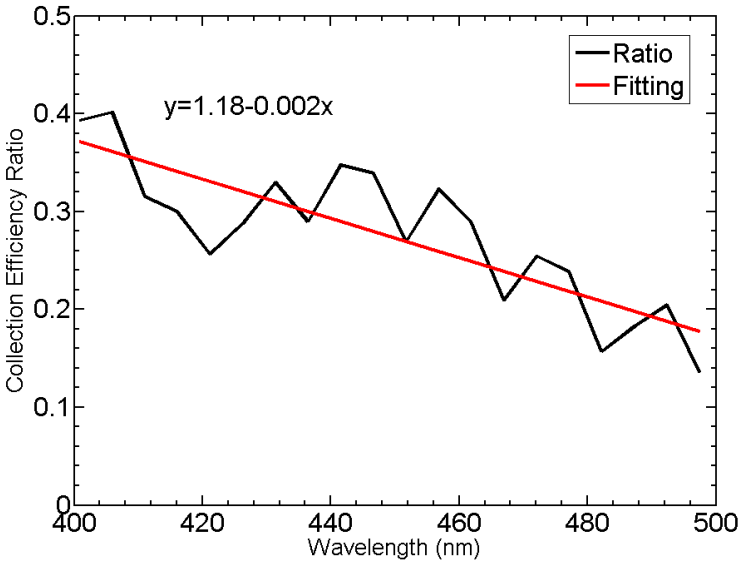

Figure 2-8 Simulated collection efficiency ratio for the 20-nm thick Al_2O_3 spacer and 30-nm thick Silver cavity. The collection angle for the far field is a full cone angle of 70°. This is a ratio of the cavity coated QD to the bare QD.

The ratio decreases with wavelength because the larger emission wavelengths in this structure emit more outside of the 70° collection cone. The cavity structure scatters light away from the center of the collection cone, which is reflected by the fractional ratio.

The emission intensity enhancement ratio can be calculated with the simulation data

for this cavity using equation (2-1). Because the initial QE of the InGaN QDs is unknown, the equation is plotted for several initial QE values in order to establish the trends.

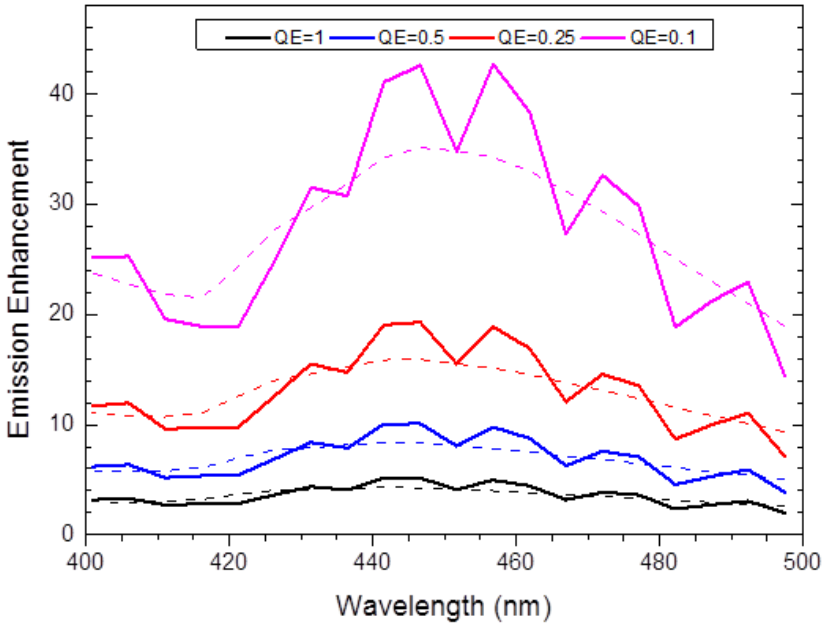

Figure 2-9 Simulated Emission Intensity Enhancement ratios for the 20-nm Al_2O_3, 30-nm silver cavity over the emission window for varying initial emitter QEs. This is comparing the oxide coated pillar to the pillar in the cavity. The fluorescence enhancement ratio is a product of the Excitation enhancement ratio, the collection efficiency ratio, and the QE ratio. The solid lines are the raw simulation values, and the dotted lines correspond to using the fitted collection efficiency ratio instead of the raw data for the product. The lower the initial QE, the more fluorescence enhancement that is expected.

Emitters that have a lower initial QE experience larger emission intensity enhancement with a metallic cavity than an emitter with a high initial QE. This can be

shown by examining the QE ratio in equation (1-14). Since $F_p > 1$, the first term in the denominator is less than 1. When $\eta_a > \eta_0$, then the second term in the denominator is also less than 1. And, as long as both terms are sufficiently smaller than 1, then their sum is less than 1 and the QE ratio is greater than one. Regardless of the InGaN QD initial QE, the excitation enhancement is constant due to its dependence on the 390-nm laser wavelength, and the collection efficiency ratio is independent of the initial QE. Therefore, the QE ratio is the most important term in the emission intensity enhancement for determining the fluorescence enhancement in this study.

2.4 Demonstration of the Al_2O_3 Silver Film Cavity

The simulations of the cavity parameters showed promising fluorescence enhancement for this film structure. While the fabrication procedures for the InGaN/GaN QDs are well documented [65], the cavity fabrication required adjusting to conventional deposition techniques in order to achieve the desired Silver film coverage.

2.4.1 Cavity Fabrication

The silver cavity fabrication process is a two-step process. The nano pillars are initially coated with a 20-nm Al_2O_3 spacer layer by ALD (Oxford ALD). ALD allows for

highly conformal deposition by depositing one atomic layer a time across the sample surface. The layer was deposited at 200°C, its thickness was confirmed by ellipsometry, and the index of refraction was measured to be 1.66.

After the dielectric spacer, the 30-nm silver layer was deposited using e-beam evaporation at a deposition rate of 1Å/s. The low deposition rate was used to help reduce roughness and ensure that the target thickness was not overshot because of the silver thickness dependent resonance wavelength. Sputtering was also considered as a silver deposition method due to its ability to coat vertical sidewalls; however, the roughness of the silver film measured from evaporation using Atomic Force Microscopy was measured to be less than 0.45-nm. Figure 2-10 shows the cavity deposition schematic.

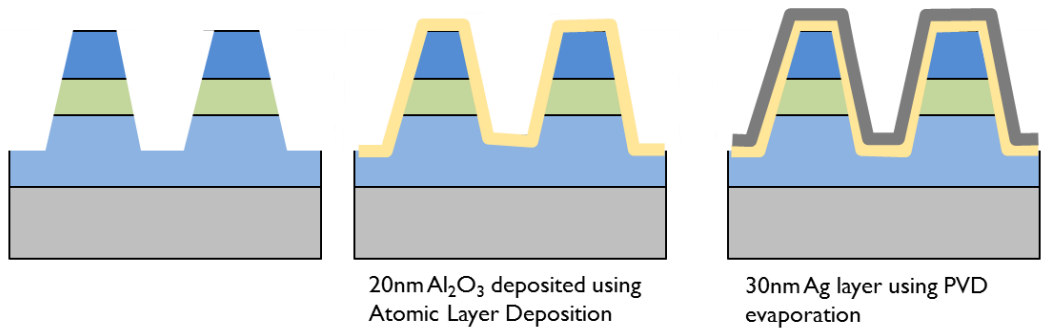

Figure 2-10 Fabrication sequence of the silver cavity layers. Al_2O_3 is deposited using ALD to ensure conformal coating. Then, silver is deposited using physical vapor deposition in an e-beam evaporator.

While the e-beam evaporated silver gave low substrate roughness using normal

incidence deposition, the 72° sidewall angle of the nanopillar caused issues with depositing the film on the pillar surface.

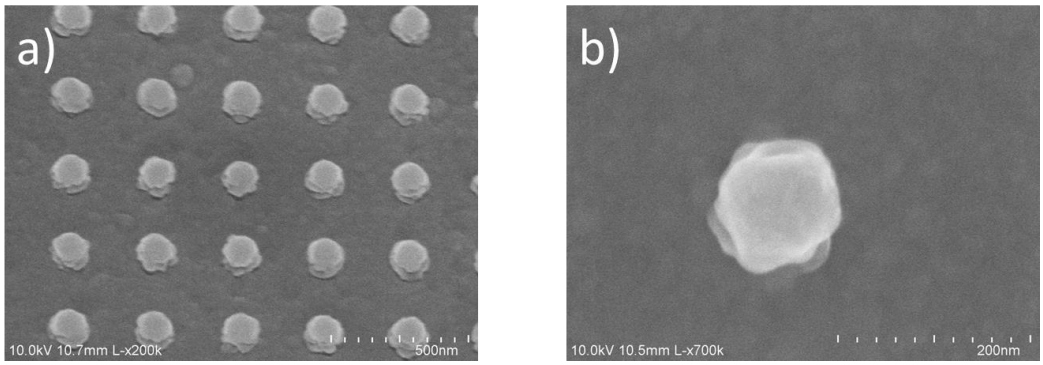

Figure 2-11 SEM images of the InGaN/GaN QD nanopillars coated in the silver film cavity using normal incidence e-beam evaporation of the silver layer. (a) A 45° angle tilted SEM image of a 24-nm diameter QD dense array with 300-nm pitch. (b) A single 24-nm diameter QD located in a sparse array with a 5-μm pitch.

Because the deposition was normal to the surface, there was a lot of layering of silver particles on the sidewall instead of a conformal deposition. This coverage deviated significantly from the desired simulation design and posed an issue. The sidewall effectively had a varying silver thickness profile along its surface, with film discontinuity at the bottom surface of the pillar seen in Figure 2-11(a).

To overcome the issue on the pillar sidewall, angled deposition was employed. Inside the evaporation chamber, the sample was mounted onto a wedge with an angle of 60° degrees. The distance from the silver source to the sample surface was reduced by

about 1 inch. Angled deposition changes the sample of the sample with respect to the incident material flux so that the pillar sidewall was effectively at an 18° angle for deposition. However, with angled deposition, there is shadowing on the opposite side of the nanopillar by the nano pillar itself. The sample is rotated 180° halfway through the deposition to ensure that all the sidewalls of the pillars are coated and the shadowing effects are minimized.[2]

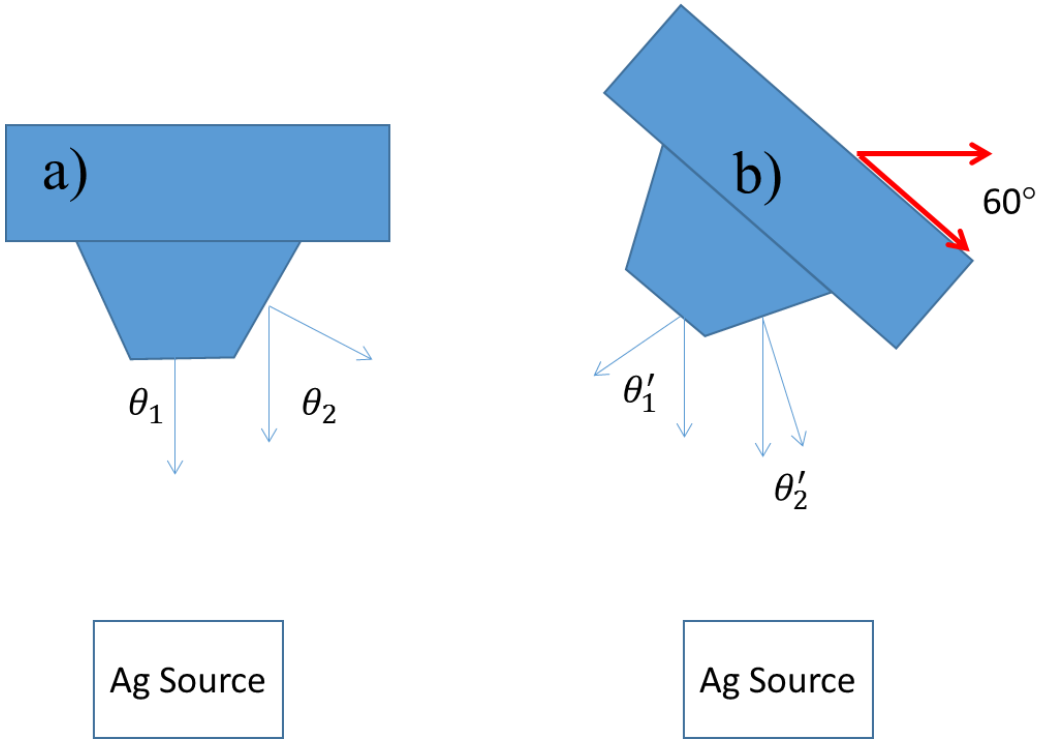

Figure 2-12 The sample configuration in the e-beam evaporator chamber. (a) The sample orientation mounted at normal incidence to the material flux. The angle between the surface and the source is determined by the nanopillar angles. (b) The sample orientation mounted on the 60° wedge. The angles of the pillar top and pillar sidewall are adjusted by

[2] Ugo Otuonye provided the angle stage for angled deposition.

the wedge angle.

With the reduced angle between the sidewall and the source, the deposition coverage was greatly improved and the roughness on the sidewall of the nanopillar was reduced. To adjust for the wedge angle and the sample rotation, the cosine rule was used to determine the new deposition thickness necessary in this configuration:

$$\frac{t_1}{t_2} = \frac{\cos\theta_1}{\cos\theta_2} \qquad (2\text{-}2)$$

Initially, 307Å of silver was deposited on one side of the sample. Then, the sample was rotated 180° and another 307Å of silver was deposition on the other side of the sample. The deposition rate was 5Å/s. This approach resulted in the 30-nm thick silver coverage on all portions of the sample.

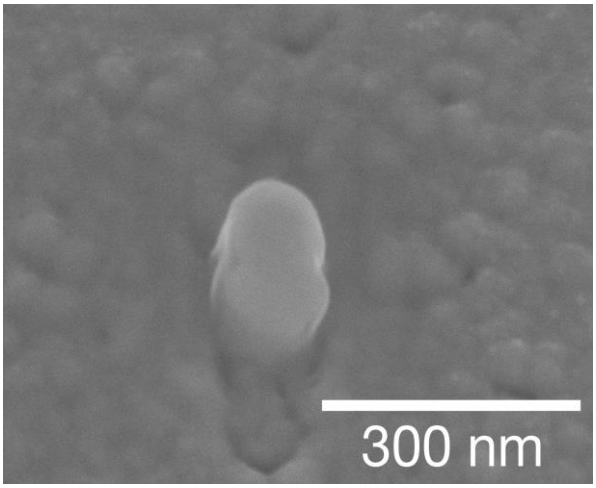

Figure 2-13 A single 28-nm diameter QD pillar from a sparse array coated in Silver using the 60° wedge and rotation method. The shadowing is near the base of the pillar, where the metal thickness is reduced. The sidewall roughness is reduced significantly and the

film continuity is improved [66].

The angled deposition approach does increase the roughness in the silver on the flat portion of the substrate, as seen in Figure 2-13, but the improvement in the pillar coverage is significant. There is reduced roughness on the nanopillar sidewall and the film is continuous down the sidewall. There is some shadowing at the base of the pillar along the rotation axis, but this is minimized due to the rotation itself. Overall, this approach worked better for the cavity coverage on the pillars and was used in the actual experiment.

2.4.2 Cavity Performance Measurements

Photoluminescence (PL) and Time-Resolved Photoluminescence (TRPL) measurements were taken with a confocal microscopy setup for single QD spectroscopy, to optically characterize the QDs and the cavity.[3] Figure 2-14 shows the setup schematic. In this setup, each QD was optically excited from the front (metal) side of the sample with a 390-nm wavelength femtosecond pulsed laser focused to a 30-μm spot, incident 55° from normal incidence. The PL signal was collected using a 40x 0.6NA objective on

[3] Tyler Hill and Lei Zhang assisted with the optical measurements.

the same side as the incident laser light. All the measurements were performed at 10 K with liquid helium cooling. The details of the optical setup are explained in Zhang [21]. A CCD camera was used to visualize the location on the sample, and a motorized stage was used for sample movement. For single photon emission verification, a Hanbury Brown and Twiss (HBT) interferometer setup was located behind a flip mirror. The pinhole located at the focal length of the lens pair was used for isolating the emission from a single QD pillar in an array, since the laser spot size excites several pillars. The QD lifetime was measured with an APD.

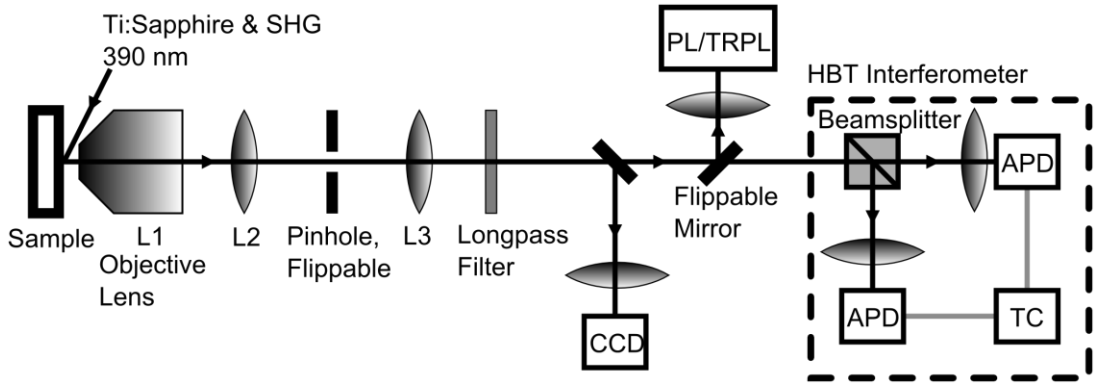

Figure 2-14 Single QD spectroscopy setup. The pinhole allows for isolation of the emission from a single QD nanopillar [24].

The sample was divided into three sections for the experiment: the control Al_2O_3 section, the silver section, and the aluminum section. The control section was for intensity calibration between different fabrication steps and measurement days. It was

unchanged throughout the experiment. The Ag section is the experimental cavity used to show the SPE enhancement due to the LSPR coupling. The Al section was used to rule out the source of the enhancement due to non-LSPR effects such as metal reflection. There is no expected LSPR for Al in the QD emission range, even though Ag and Al have similar reflectivity in that window. Thus, if the enhancement is due to metal reflection, both metals should give comparable results for emission intensity.

The experimental flow is as follows. First, Al_2O_3 was deposited on all three sections. The QDs were measured with the Al_2O_3 layer as the initial data point to rule out the effects of surface passivation from ALD on the bare pillars. Then, the saturation intensity of the QDs was found. This is the excitation intensity such that with a higher excitation intensity, there is no increase in the emission intensity measured. The dot is effectively saturated with carriers. For this sample, that value was 707 W/cm^2. Individual QDs from each section had their PL and TRPL measured at 283 W/cm^2 (2000μW) and again at 707 W/cm^2 (5000μW). Finally, the Ag and Al films were deposited on their respective sections, and the measurements were repeated again on the same QDs measured before deposition.

The PL and TRPL emission spectra for a single QD measured at both excitation powers with and without the Ag cavity as shown below. Because of the ordered nature of

the array, we can ensure we are measuring the same dot at different stages of fabrication.

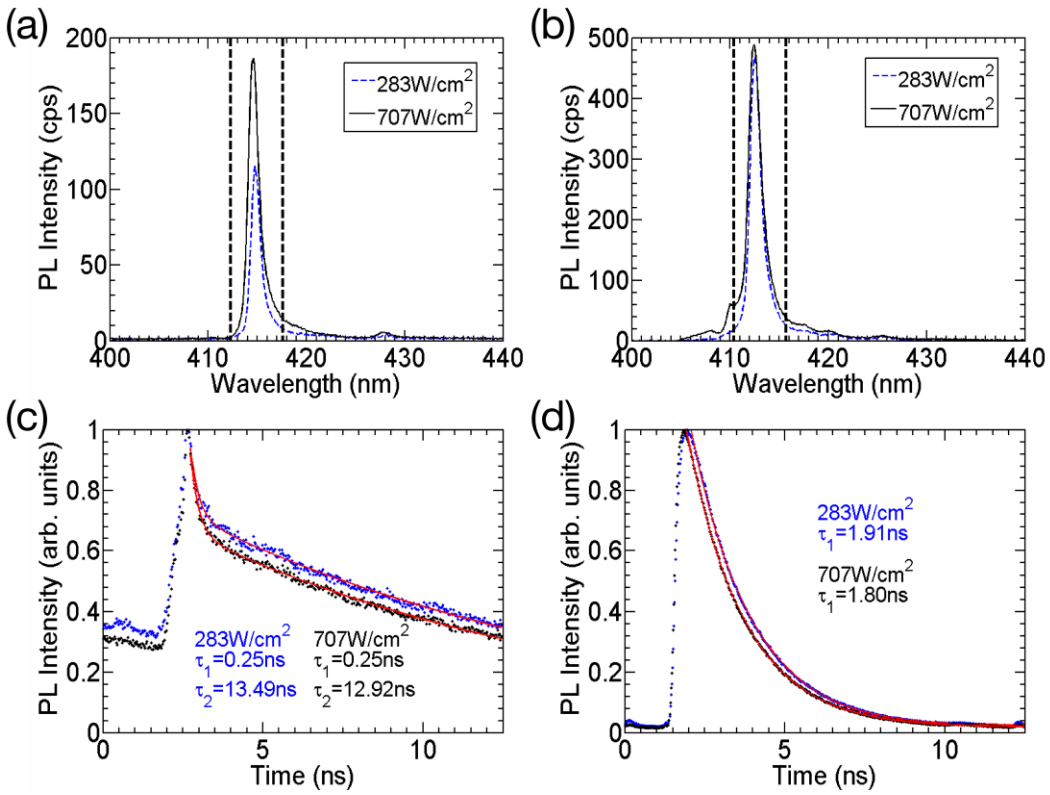

Figure 2-15 Optical measurements of a single QD taken at 10 K before and after the deposition of the silver cavity for two excitation intensities, 283 W/cm^2 (blue) and 707 W/cm^2 (black). (a) PL intensity taken initially and (b) the enhanced PL intensity after the cavity fabrication. The dotted lines indicate the position of the spectral filter used for the TRPL and later autocorrelation measurements. (c) TRPL intensity taken initially was fit with a bi-exponential function. The functional weighting of τ_1 and τ_2 are 0.23 (0.71) for 283 W/cm^2 and 0.26 (0.66) for 707 W/cm^2. (d) The TRPL intensity taken after the cavity deposition. Here, $\tau =$ 1.91ns and 1.80ns at the respective excitation intensities. The weighting of the second exponential term was negligible; thus, only one lifetime is given [66].

The Ag cavity caused an improvement in the integrated intensity of the exciton PL

by 4.28 and 3.25 times, respectively, at the excitation intensities. Even though there is significant spectral mismatch between the emission wavelength and the cavity resonance in Figure 2-7, the broad nature of the resonance still causes enhancement. For the TRPL, the QDs exhibited two distinct lifetime components before the Ag deposition: a shorter component on the order of ~250ps, and a longer component on the order of nanoseconds, which was associated with the exciton emission. This was confirmed later in the $g^2(0)$ lifetime fittings and from the cavity lifetime, which is still longer than the ~250ps component. Because of the two-step nature of the data, the TRPL data was fitted with a bi-exponential function to quantify the magnitude of each lifetime component in the collected signal. The function weights of τ_1 and τ_2 are 0.23 (0.71) with lifetimes of 0.25ns and 13.5ns for 283 W/cm^2 and 0.26 (0.66) with lifetimes of 0.25ns and 12.9ns for 707 W/cm^2. From the weighting, we can see that the short lifetime component only accounts for about ⅓ of the emission intensity. After the cavity deposition, there was only one TRPL lifetime of 1.91ns (1.80ns) respectively, as the weight for the second less was less than 1%, signifying a single exponential. The lifetime reduction ratio for the QD was calculated using only the long lifetime component, since that component dominated the bi-exponential. For this QD, the lifetime reduction ratio at 283 W/cm^2 was 7.1 $\pm$ 0.02 times, and at 707 W/cm^2, it was 7.2 $\pm$ 0.02 times.

The same measurement procedure was repeated for several QDs in each of the three sections and the PL intensity enhancement ratio versus the TRPL lifetime reduction ratio was plotted on a log-log plot for the lower excitation intensity of 283 W/cm^2.

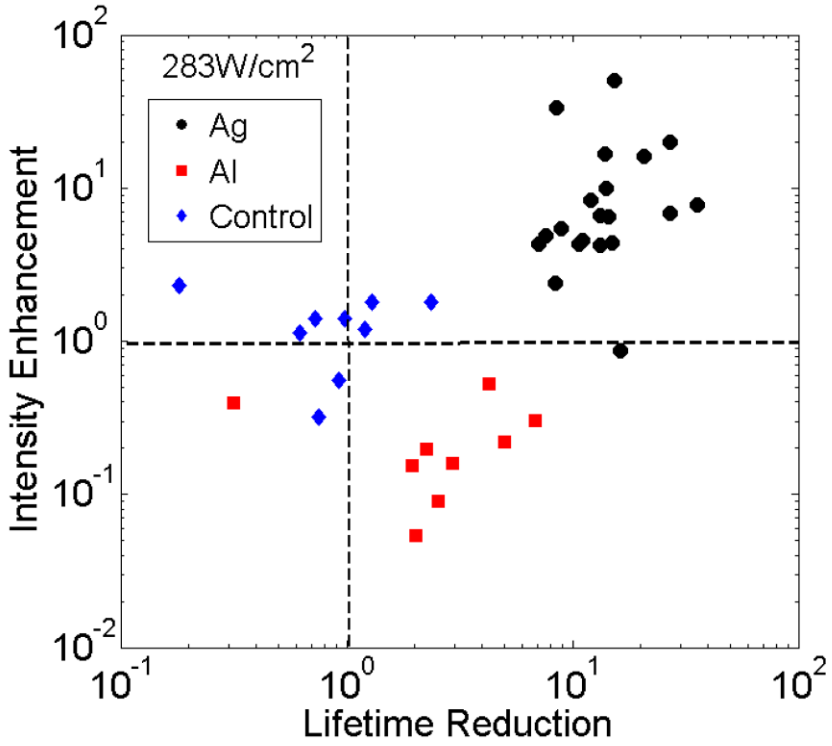

Figure 2-16 Lifetime reduction and PL intensity enhancement on a log-log plot for each individual QD measured in the three sample sections with an excitation intensity of 283 W/cm^2. The (black) circles represent the Ag cavity data, the (red) squares represent the Al cavity data, and the (blue) diamonds represent the control (Al_2O_3) data. Values less than 1 indicate a reduction in intensity or the lifetime increasing, respectively. The dotted lines represent no change for the axis parameter, and their intersection indicates the point of an unchanged dot [66].

From Figure 2-16, the effect of the Ag and Al cavities can be seen clearly. The control

section had some slight variation, but remained mostly unchanged between measurements as the data clustered around one for both ratios. The intersection of the dotted lines corresponds to an unchanged dot, which is where the control data is centered. With the Ag cavity, there was simultaneous intensity enhancement and lifetime reduction, as the data is centralized in the upper right quadrant, signifying enhancement of the spontaneous emission rate. In the Al cavity, there is the expected lifetime reduction associated with placing a metal structure near an emitter, but there is also intensity reduction. The data is localized to the lower right quadrant. The Al has more losses and does not have a resonance in this wavelength range, so there is no intensity enhancement.

The average intensity enhancement taken from the 20 QDs measured in the Ag section is 10.9 $\pm$ 2.6 times with an average lifetime reduction of 15.0 $\pm$ 1.6 times. The larger lifetime reduction ratio compared to the intensity enhancement ratio is attributed to the additional nonradiative recombination from the Ag cavity in the form of absorption, since the AQE is less than unity. The averages of the results in the Al section were 0.23 $\pm$ 0.04 times for the intensity ratio and 3.13 $\pm$ 0.61 times for the lifetime ratio. The contrast between the Ag and Al results ruled out the mirror effect as the enhancement source. For the control section, some of the QDs showed slight changes in the lifetime. Over time, the shorter lifetime component of the QD from the bi-exponential fitting

becomes more weighted. The origins of the shorter lifetime component and its changes over time are unknown and are under worth studying in future work. In addition, the initial exciton lifetimes of interest are on the order of the repetition time of the laser (12.5ns). Because of this, the fitting of the longer lifetime component is more susceptible to fluctuations between measurement days, which can result in perceived lifetime variations that may not be physical. Overall, the control section stayed consistent between measurements.

The Purcell factor, the lifetime reduction ratio, and the intensity enhancement ratio determine how good the cavity is and how it compares to the simulation. Since we only experimentally have the latter two factors, we need to arrange equation (2-1) in terms of those factors to solve for the F_p. By substituting into equation (1-14) the lifetime components for the quantum efficiencies, we can get:

$$\frac{\eta}{\eta_0} = F_p \times \frac{\tau_{tot}^{new}}{\tau_{tot}^{0}} \qquad (2\text{-}3)$$

where τ_{tot}^{new} is the measured lifetime after the cavity and τ_{tot}^{0} is the initially measured long lifetime component from the bi-exponential fitting. This allows us to relate the QE ratio into terms that we have measured.

In order to remove the excitation intensity enhancement from equation (1-14) and the Purcell factor calculation, the saturation intensity was measured experimentally. If the

QD is pumped at its saturation intensity, then the enhanced electric field at the QD location due to the metal structure will not affect the number of generated carriers, since the carriers are already saturated. To calculate the saturation intensity, the excitation intensity was swept across three orders of magnitude up to 1500 W/cm^2, and the emission intensity was measured for individual QDs in each section.

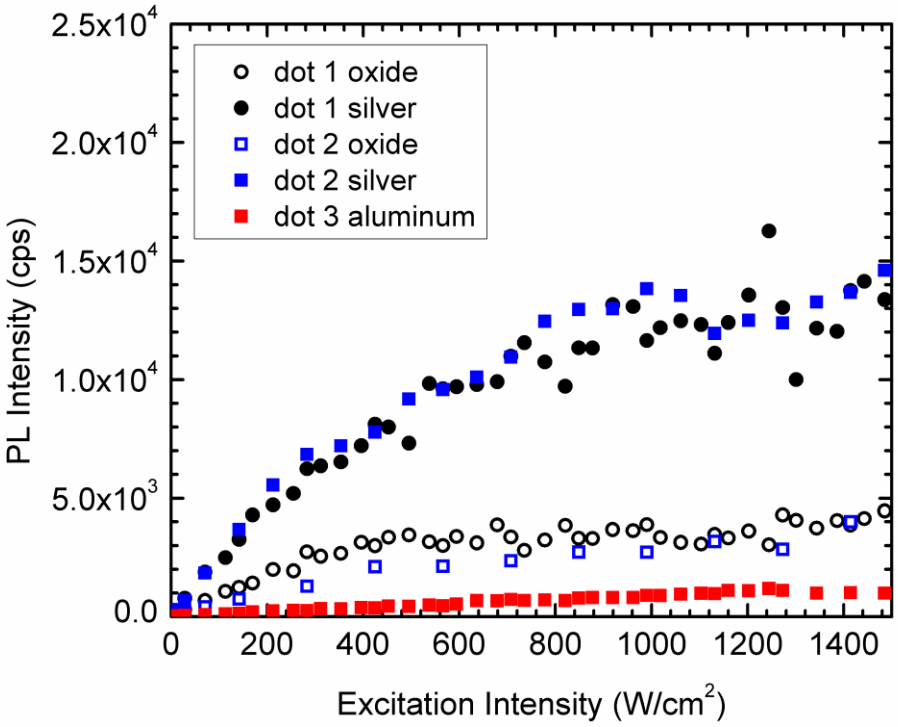

Figure 2-17 PL intensity saturation curves for two individual QDs measured before (open marker) and after (filled marker) the Ag cavity deposition. The saturation curve for the Al coated QD in (red) as a reference. The two different integrated intensity saturation levels in the Ag QDs demonstrate the enhanced radiative decay process [66].

From this measurement, the saturation intensity was established to be 707 W/cm^2, as the integrated intensity for the oxide coated QDs levels off around that excitation intensity. This is why the data was taken at two intensities for each QD, to ensure that the saturation point was included.

With the saturation intensity established, we studied its effect on the PL intensity ratio.

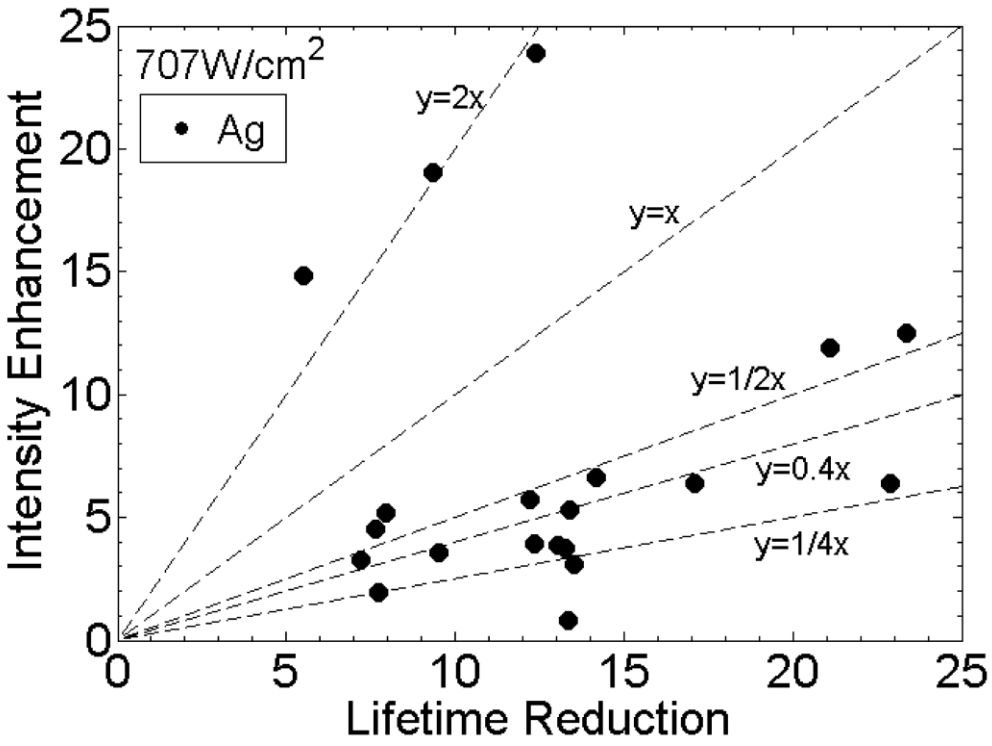

Figure 2-18 PL intensity enhancement versus lifetime reduction ratio for each Ag cavity QD measured at the saturation intensity of 707 W/cm^2. Values less than 1 indicate a reduction in the intensity or the lifetime increasing, respectively. Dotted guidelines show the intensity enhancement ratio ‘y’ as a function of the lifetime reduction ratio ‘x’ [66].

When excitation enhancement is removed by pumping above saturation (at 707 W/cm^2), the average PL intensity enhancement ratio was decreased by about 30% from 10.9 $\pm$ 2.6 times to 7.33 $\pm$ 1.32 times. This makes sense as the electric field enhancement seen as the lower pumping intensity of 283 W/cm^2 is now compensated by saturating the QDs initially. Using the linear guidelines on Figure 2-18, the data appears to fall into two distinct groups: QDs that have fractional intensity enhancement of the lifetime reduction, and QDs that have intensity enhancement scale greater than the lifetime reduction, by roughly a factor of two.

The first regime is to be expected of a metallic cavity, because the AQE is less than 1. For this Ag cavity, around the emission wavelength of 411-nm, the simulated AQE is 0.47 from Figure 2-7. Part of the lifetime reduction is due to metal losses such Joule (heat) losses, which contributes to the low AQE. If the initial QD QE is close to unity, then the final QE in the cavity will approach the upper bound, which is the cavity AQE. Since most of the QDs initially were very bright, this could imply that the initial QEs were relatively high. Thus, the fractional relationship is to be expected.

In the second regime, having the scalar intensity change implies that the QDs either have a low initial QE or were not fully saturated at the excitation intensity of 707 W/cm^2.

Compared to the other QDs in this section, those three QDs were relatively dim initially, making the low initial QE hypothesis a high possibility. So, the cavity improves the final QE of the QDs and the intensity enhancement is the result. Even with the metal losses, a net QE improvement is possible for poor emitters.

Pumping the QDs at the saturation intensity accounts for the excitation enhancement ratio in equation (2-1). However, because we are using pulsed excitation instead of a continuous wave source, we must consider the laser repetition rate and its effect on the exciton occupation probability in the QDs. Hence, equation (2-1) is rewritten with consideration for the experimental parameters as:

$$\frac{\mathrm{S^{new}}}{S^0} = \frac{\xi^{new}}{\xi^0} * \frac{f^{new}(I)}{f^0(I)} * \frac{R^{new}}{R^0} * \frac{\eta^{new}}{\eta^0} \qquad (2\text{-}4)$$

Here, 'S' is the emission intensity S^{em}, 'ξ' is the collection efficiency, '$f(I)$' is the QD exciton occupation probability, 'R' is the effective QD fill rate, and 'η' is the emitter QE. The new factors here are 'f(I)' and 'R'. The factor f(I) is the probability that the QD is excited into its excitonic state when the QD is empty and the laser pulse hits. f(I) will increase with the excitation intensity, 'I_{exc}', at the QD and will reach unity at the saturation intensity 'I_{sat}', $f(I_{sat}) = 1$, once the excitonic state is filled and not given enough time to decay.

The product ($R \times \eta$), is the rate in which the QD generates photons. To understand

'R', we first consider the continuous wave excitation case. Under continuous wave excitation, R is simply the inverse of the QD lifetime τ_{tot}. The QD cannot be refilled until the exciton decays. Under pulsed excitation, R is a function of the laser repetition rate and is limited by the repetition rate R_{laser}. Because the QD can only be refilled if it is empty when the laser pulse hits, the PL intensity measured depends on both R_{laser} and τ_{tot}. For a QD with a lifetime much shorter than the laser repetition time ($1/R_{laser}$), the QD is always empty at the time of the new laser pulse. In this case, R is simply R_{laser}, which is (1/12.5ns) for our setup. However, for a QD with a lifetime comparable or much longer than the repetition time of the laser, the effective repetition time (1/R) is written as a weighted sum of the repetition interval

$$\frac{1}{R} = \sum_{n=1}^{\infty} \left(p_n \times \frac{n}{R_{laser}} \right) \qquad (2\text{-}5)$$

where 'n' is the n-th repetition interval during which the QD decays and p_n is the associated probability of decay during that interval. The area under the exponential decay fitting TRPL data for the lifetime determines p_n for each interval. The R ratio (R^{new}/R^0) at 283 W/cm^2 for the silver QDs ranged between $1.4-3.2$, and at saturation (707 W/cm^2) the R ratio range was between $1.4-2.8$.

With the R ratio and the fact that at saturation the QD exciton occupation probability ratio is unity, the Purcell factor is calculated for each of the Ag cavity QDs. For this

calculation, resulting Purcell factor is the lower bound, since we ignored the collection efficiency ratio, which is less than one from simulation. At saturation, the average Purcell factor for the 20 QDs was 46 $\pm$ 9.0 with a fractional error of less than 5% for each individually calculated Purcell factor. The Purcell factor of each dot is plotted in Figure 2-19. Since, there is an association between initial QD brightness and intensity enhancement, the Purcell factors are in order of the QD's initial PL intensity. Sorting the values this way, it is easy to see that indeed the dimmest initial QDs have the largest Purcell factors. Also, included above the PL intensity is the PL peak photon energy in eV. As the QD diameter decreases, the photon energy increases, due to the diameter dependent strain. Although the entire QD array is designed around one diameter, there is slight variations of $\pm$2-nm. Smaller QDs have a larger surface-to-volume ratio, which contributes to lower QEs due to enhanced surface recombinations. Therefore, the smaller dots have a lower QE and receive more Purcell enhancement.

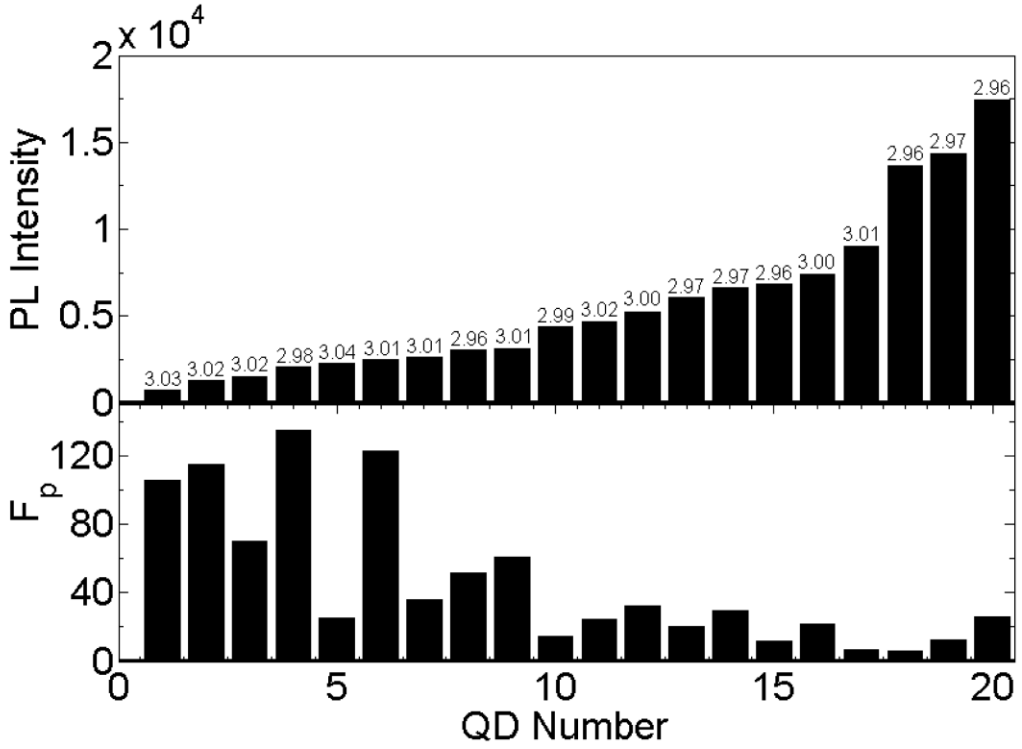

Figure 2-19 Initial measured PL intensity for the oxide coated QDs and the calculated Purcell factor in the Ag cavity at the saturation intensity of 707 W/cm^2. The dots are in order of PL emission intensity collected initially from left to right. Numerical labels above the bars correspond to the PL peak energy in eV. The dimmest dots have the largest photon energy, indicative of the smaller QD size. Smaller QDs received the largest enhancement and have a larger Purcell factors [66].

According to the numerical calculations, small variations in the QD diameter and thickness of 10% (2.8-nm) of the intended value do not result in as large a change in the enhancement as observed in Figure 2-19. Thus, the origin of the correlation between the variation in the Purcell factor and the initial QD QE is uncertain and is a study for future investigation.

2.4.3 Cavity Enhanced Single Photon Emission

For the InGaN QDs made by this top dot method, previously we have demonstrated single photon emission by the autocorrelation measurement up to 90 K [21]. However, we had not recorded enhanced single photon emission through cavity coupling. In this experiment, in addition to the characterization of the PL and TRPL changes with the Ag cavity, the effect on the single photon emission was studied. To verify that the InGaN nanodisks within the nanopillars are indeed true QDs, we performed a second-order correlation (g^2) measurement. Using the HBT interferometer setup, photons that are emitted from the QD are split between a two arms: a start arm and a stop arm. When a photon is detected at one of the two arms, a timer is initiated that stops when a photon is detected at the second arm. Due to the nature of the photon, if the QD is a true SPS, then the single photon cannot be detected simultaneously at both detectors. Thus, at a time delay of zero or zero nanoseconds between detections, the value of the autocorrelation should be zero.

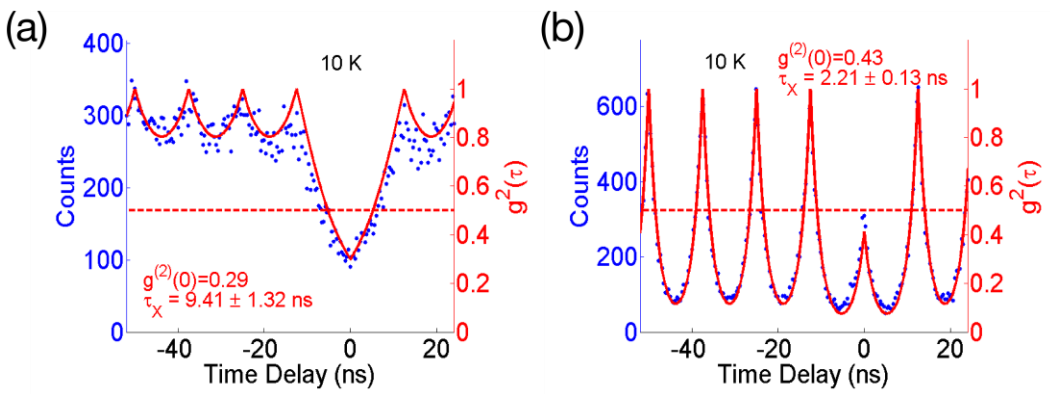

Figure 2-20 Autocorrelation g^2 measurements for the QD examined in Figure 2-15 at 10 K. (a) g^2 measurement of the QD before the addition of the cavity, measured with an excitation intensity of 707 W/cm^2. The data is shown without background subtraction. The fitting (solid red) gives a $g^2(0)$ values of 0.29 and a lifetime $\tau = 9.41 \pm 1.32$ ns. (b) Autocorrelation taken with the Ag cavity, showing maintained single photon emission and a $g^2(0)$ value of 0.43 with a reduced lifetime of $\tau = 2.21 \pm 0.13$ ns. [66].

The emission from the QD was spectrally filtered along the dotted lines in Figure 2-15 for this measurement in order to reduce the contribution from the non-excitonic emission. The data was fit following the formulism in Zhang [21]. The QD initially started as a single photon emitter, indicated by the $g^2(0)$ of 0.29, which is less than the accepted value of 0.5. There is clear photon antibunching without background subtraction. The measurements in Figure 2-20(a) & (b) look different due to the different lifetimes. Initially the QD has a long lifetime, so in between the laser repetitions over 12.5ns, the signal does not fully decay to the background value in Figure 2-20(a). In Figure 2-20(b), as the lifetime is not much shorter than the repetition time, the decay to the background

value between laser pulses is more pronounced. Inside the cavity, the $g^2(0)$ value increased to 0.43, but it is still below 0.5. The increase in the $g^2(0)$ value is due to the enhancement of the background emission that overlaps with the exciton spectrum. The base of the PL spectrum in Figure 2-15(b) within the spectral filter is still very broad, and it contaminates the measurement. From the autocorrelation measurements, the exciton lifetime can be fit to a single exponential. The lifetime fittings agree with the magnitude of the lifetimes measured from the TRPL measurement and reaffirm the conclusion that the long lifetime component in Figure 2-15(c) is the correct lifetime. The single photon emission is enhanced and preserved by the Ag cavity.

2.5 Summary

In summary, we demonstrated single photon emission coupled to a silver film cavity structure. Taking advantage of the tapered nanopillar shape in the cavity design, the silver cavity was self-aligning with the QDs. By introducing the angled deposition procedure, we were able to reduce sidewall roughness and improve film coverage along the side of the nanopillars. Even with spectral mismatch between the QDs and the cavity LSPR, order of magnitude enhancements were observed in the emission intensity and lifetime reduction. The average Purcell factor of the cavity taken from the 20 QDs measured with

the cavities was 46. These results are significant as they show the simultaneous enhancement of many QDs with a single cavity coating across a large area, which has a large practical significance over other methods that involve a cavity to be placed around individual dots. In addition, lifetimes on the order of ~1ns were demonstrated, indicating we are approaching the gigahertz repetition rate.

While we were able to demonstrate the QD-cavity coupling, our current setup had a few limitations. The wavelength mismatch and the taper of the nanopillar reduced the maximum Purcell factor achievable with this structure. The goal of the picosecond time scale requires more engineering of the enhancement for a larger Purcell factor. In the upcoming chapters, the cavity wavelength matching the emission wavelength is addressed, and the cavity design is adjusted to increase the expected Purcell factor by two orders of magnitude. Resonance wavelength matching leads to improved emission intensity enhancement. The open top cavity builds upon the silver film cavity design in this chapter and takes advantage of the nanopillar wet etching technique to bring the silver closer to the QD without significantly reducing the AQE.

Chapter 3

Silver Cavity Fabrication Improvements: Increasing the Emission Intensity Enhancement

3.1 Introduction

In Chapter 2, we demonstrated that the silver film cavity can be deposited on a sample with conventional deposition techniques and used to couple the emission from the QDs to the LSPR of the silver cavity. Due to the broadband resonance of a metallic cavity, there was still resonance enhancement with the emission wavelength mismatch to the resonance. In order to better characterize the strength of the cavity, overlapping the emission wavelength and resonance wavelength is key. In this chapter, the focus is on improving the wavelength overlap, improving on the silver film deposition coverage, and increasing the Purcell factor of the cavity.

Since the emission wavelength of the QDs at the intended diameter of 25-nm is fixed at 411-nm with the previous wafer sample, matching the emission wavelength to the resonance wavelength requires another sample with a longer emission wavelength. By

increasing the indium concentration in the epitaxial wafer, the emission wavelength can be red-shifted. However, due to the larger indium concentration, the internal QE of the emitters is reduced. There is more strain in the system with the larger lattice mismatch, which affects the radiative recombination efficiency. Thus, the QDs from this wafer will have a longer decay lifetime, and an even larger Purcell factor will be necessary to achieve the picosecond timescale.

The coverage of the silver cavity film on the nanopillars is critical for its performance, as the thickness of the cavity controls the resonance condition and surface roughness lowers the AQE of the cavity. Depositing silver using the angle deposition approach improved the silver sidewall coverage on the pillar structure, but due to the single rotation, left the sample with rotation induced shadowing along the rotation direction, as seen in Figure 2-13. In order to overcome this rotation induced shadowing, constant rotation would be required. A rotational stage, with angle adjustment was built in order have the sample constantly rotating during deposition. This improved the silver coverage by reducing the self-induced shadowing.

As previously demonstrated in Chapter 2.3.2, changing the oxide spacer thickness affects the total enhancement from the cavity. This is due to the reduction in the distance between the metal layer and the emitter. In order to get a larger Purcell factor out of the

new cavity design, the spacer layer thickness was reduced from 20-nm to 10-nm of Al_2O_3. Even with half of the spacer layer, an AQE of >60% can still be achieved with the cavity design.

Adjusting these three parameters in this experiment resulted in improved emission intensity enhancement with larger pillar structures, demonstrating the improved coupling through wavelength matching.

3.2 Resonance Wavelength Matching

The effect of the reduced spacer thickness on the cavity resonance wavelength was characterized initially before the indium composition in the wafer was designed, to ensure better wavelength matching. Using Figure 2-6 as a starting point, the Purcell factor and AQE of a 30-nm thick silver and 10-nm thick Al_2O_3 cavity was studied for QD nanopillars with diameters of 25-nm, 28-nm, and 32-nm. The larger diameters were also considered due to the as they have a higher fabrication yield. From the measurement of the sample with the 10-nm Al_2O_3 layer taken during the experiment, it was very clear that the 32-nm diameter nanopillars were the smallest diameter that we could reliably identify and measure repeatedly for measurement comparisons. The data was taken with large excitation intensity (1.415 kW/cm^2) to ensure that the arrays could be seen.

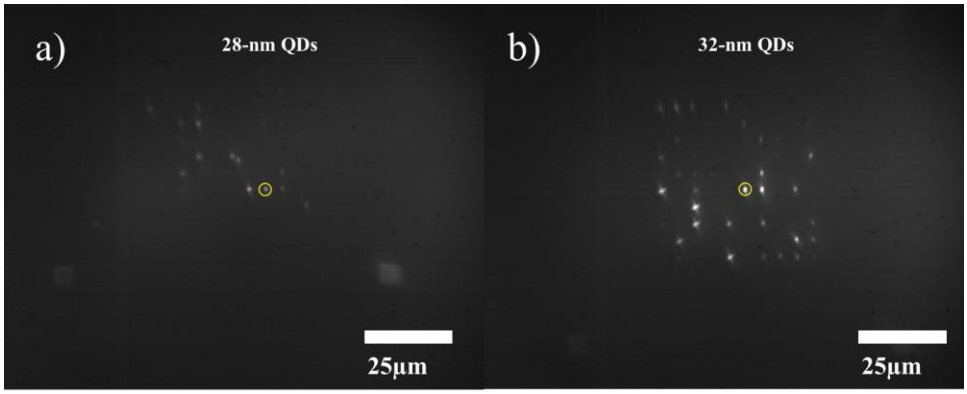

Figure 3-1 CCD camera images of the arrays of the nanopillars from the higher indium concentration wafer taken at 1.415 kW/cm^2. (a) An array of 28-nm diameter nanopillars. Most nanopillars do not emit, so it is difficult to determine the array position. (b) An array of 32-nm diameter nanopillars. This is the smallest size that has identifiable pillars in the grid for comparative measurements. The yellow circle corresponds to the focus of the pinhole in the confocal setup in Figure 2-14.

With an increase in the diameter, the expected Purcell factor decreases, as the structure is larger and the metal film is further away from the center of the emitter. Increasing the diameter by 7-nm to 32-nm leads to a two-fold reduction in the Purcell factor. So, ~30-nm is the largest diameter that should be considered with this type of cavity structure for significant enhancement. Even with the reduced spacer thickness, the expected AQE for the three diameters is >60% at the resonance peak. The AQE increases with diameter in Figure 3-2, due to the lowered metal losses in a larger structure.

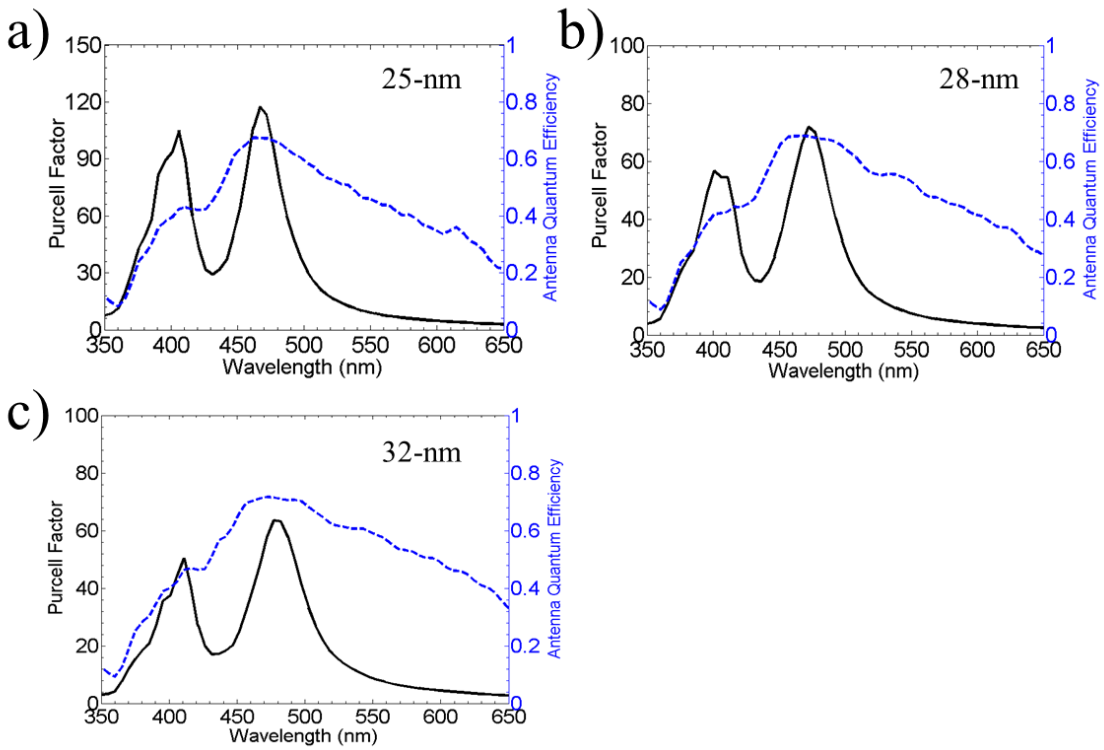

Figure 3-2 Simulated Purcell factor and AQE for the 30-nm silver, 10-nm Al_2O_3 film cavity on varying pillar diameters of (a) 25-nm, (b) 28-nm, and (c) 32-nm, respectively. The Purcell factor decreases with diameter while the AQE increases with diameter. The resonance peak wavelength is relatively constant with diameter.

For the 32-nm diameter nanopillar, the resonance wavelength peak is about 480-nm and the expected Purcell factor is ~60 with an AQE of ~72%. The resonance peak wavelength is relatively constant with diameter, as the diameter change is less than 10-nm and the change in the effective index of refraction of the pillar and spacer layer under the silver is small. Based on the simulation design, the desired emission wavelength for the nanopillar structures is 480-nm. An X-Z cross section of the

re-designed cavity layers compared to the original cavity structure is shown in Figure 3-3. The metal thicknesses are the same; only the spacer thickness is reduced. Compared to the previous simulation parameters in Chapter 2, at the emission wavelength, which is indicated by the red arrow, we expect a six times increase in the Purcell factor from ~10 to ~60 and a 53% increase in the AQE from 0.47 to 0.72.

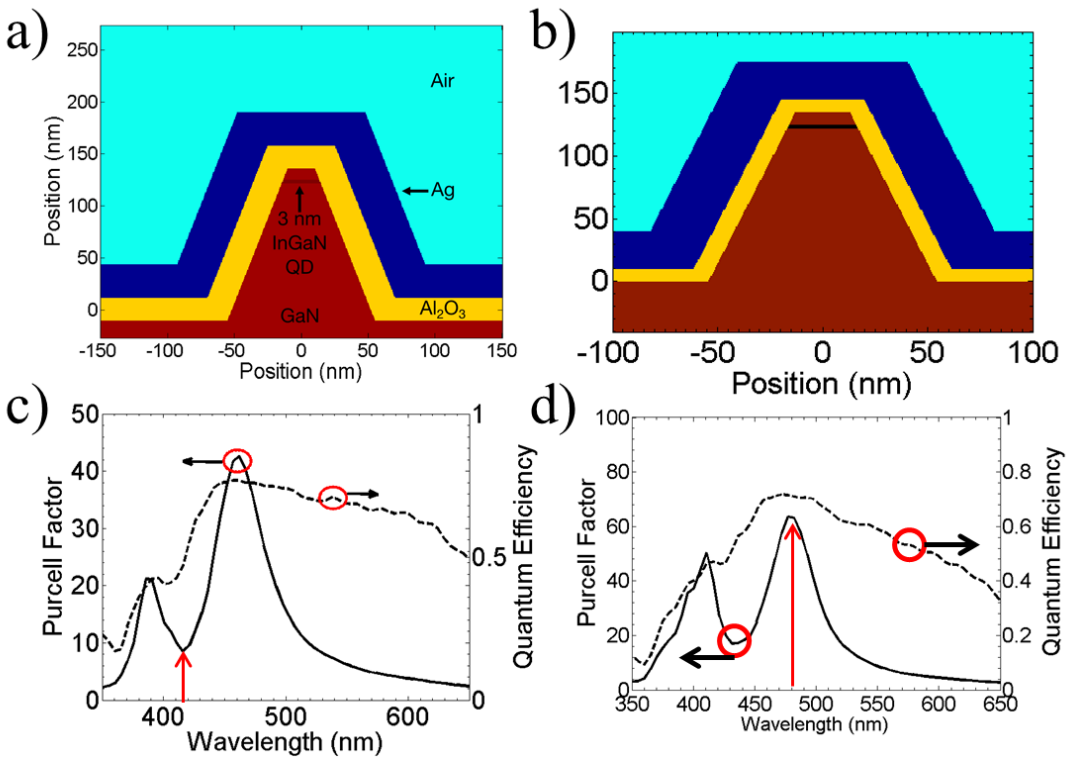

Figure 3-3 Comparison of the original silver cavity to the new silver cavity with the thinner Al_2O_3 spacer layer. (a) X-Z schematic of the original 30-nm Ag, 20-nm Al_2O_3 cavity on a 25-nm diameter QD. (b) X-Z schematic of the new 30-nm Ag, 10-nm Al_2O_3 cavity on a 32-nm diameter QD. (c) Simulated Purcell factor and AQE for the 30-nm silver, 20-nm Al_2O_3 film cavity on 25-nm diameter QD. (d) Simulated Purcell factor and AQE for the 30-nm silver, 10-nm Al_2O_3 film cavity on 32-nm diameter QD. The red arrows correspond to the emission wavelength used in the experiment.

3.3 Angled Rotational Deposition

Angled deposition of the silver layer helped to fix the sidewall coverage of the nanopillar structures, but introduced the issue of shadowing. For sparsely placed nanopillars, like the previous experiment, the effects of shadowing are minimal, since there are no adjacent structures. There was only self-shadowing along the rotational axis due to two deposition steps. However, for a denser array of QD nanopillars with spacing less than a few microns, the neighboring nanopillars start to block the incoming metal flux, resulting in complete gaps in the metal coverage. To fix this issue, rotation was added to the deposition in order to minimize the duration of shadowing along any given axis.

The rotational stage was fabricated using metal machining and 3-D printing. For rotation, a servo motor and battery were used. They were fitted into sockets on a 3-D printed stage. Attached to the motor was a glass slide for sample mounting and a 100-ohm potentiometer for rotational velocity control. [4]

[4] Chih-Wei Chien performed the stage 3-D printing.

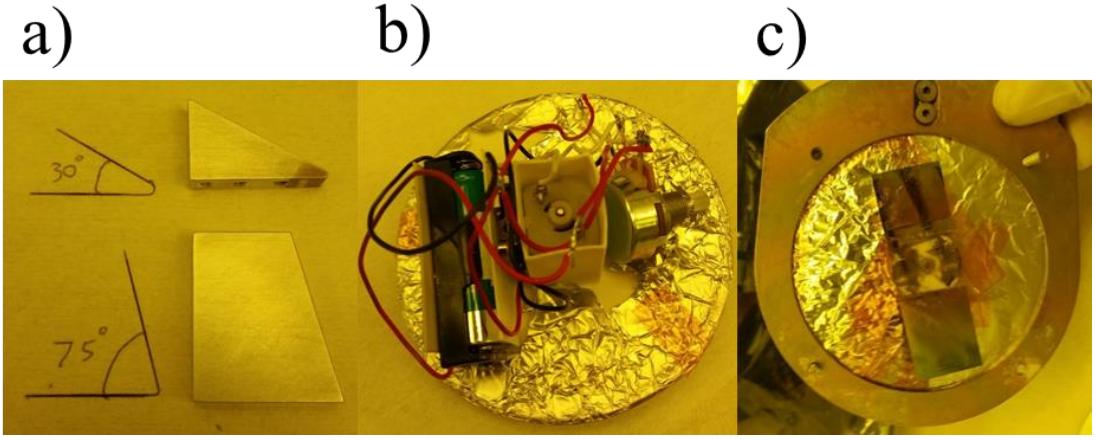

Figure 3-4 Parts of the rotational stage. (a) The machined steel triangles for angle mounting. (b) The 3-D printed stage wrapped in aluminum foil. There are slots for the servomotor, battery holder, and potentiometer. (c) The bottom side of the stage loaded into the metal carrier. The glass slide is the mounting point for the sample. The stage is secured by clamps into the carrier.

The entire 3-D printed stage was loaded onto a metal carrier and secured by clamps. The stage itself was wrapped in aluminum foil to help with heat dissipation during deposition, as the 3-D printed material is sensitive to heat. The metal carrier is mounted using an angled wedge to a holder that fits in the deposition chamber slot. Two angle wedges were fabricated with machined steel for different deposition angles. The entire structure allows the user to set the deposition angle and rotational speed by the potentiometer.[5]

[5] Angle wedges machined by the Physics department machine shop.

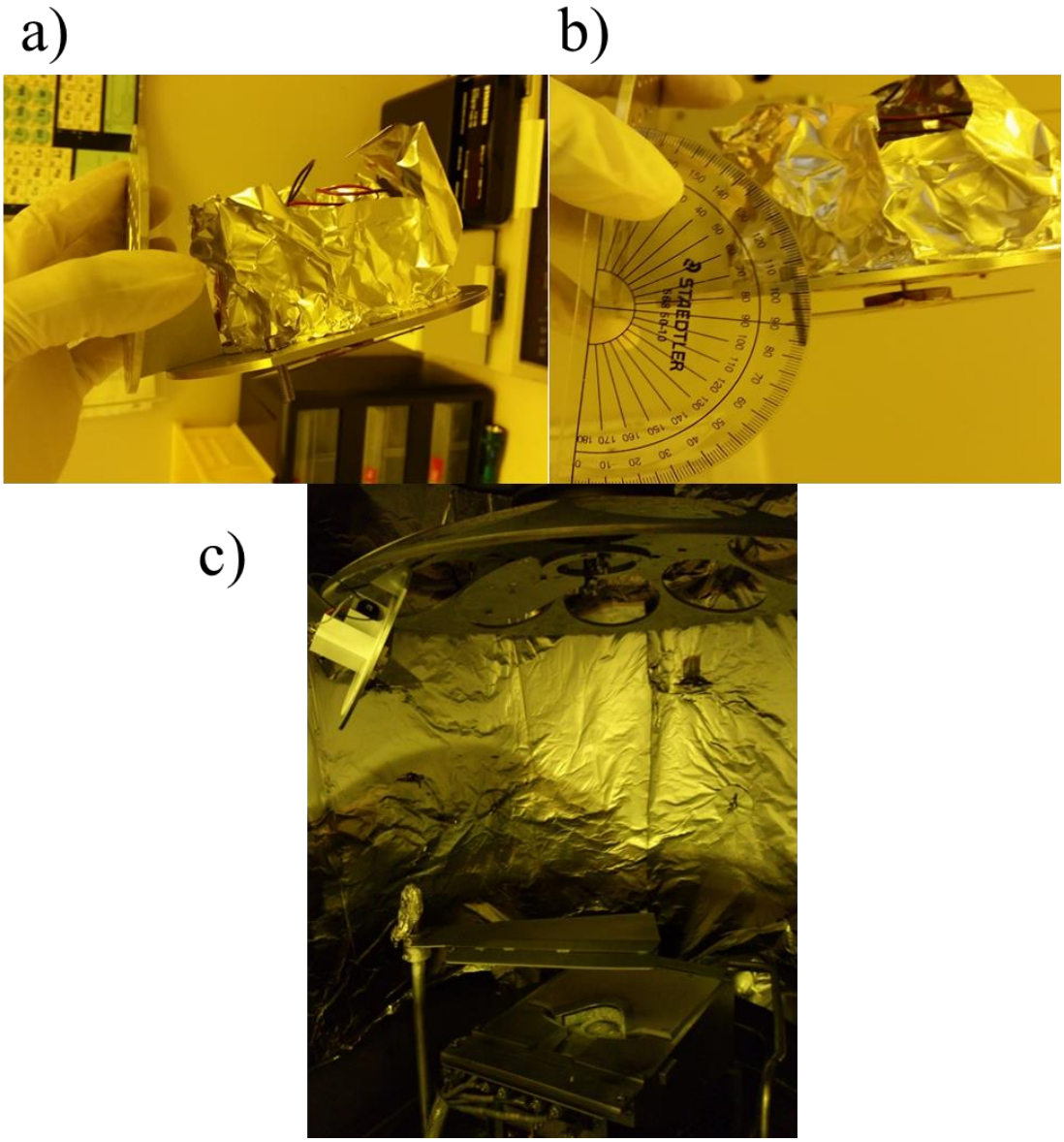

Figure 3-5 The assembled rotational stage, angled mount, and chamber mount. (a) The raised foil protects the circuit components during deposition with the high angle mount (75°). (b) Protractor measurement of the angle, confirming the 75° mount is 75°. (c) Illustration of the rotational assembly mounted into the evaporator chamber. This was a test fit in the chamber, so the stage is not wrapped in protective foil.

For this angled rotational deposition experiment, the 30° mount was used. The

resulting angle of the sample on the mount was ~60°. The speed of rotation was set for 1-2 rotations per second. Since the rotational velocity is controlled by potentiometer turns, this rate used for each deposition is approximate. Due to the reduced throw distance of the material to the sample mounting point, the programmed deposition thickness was adjusted accordingly to ensure that 30-nm of silver was deposited. Figure 3-6 shows a comparison of 30-nm of silver deposited on dense arrays by the angle deposition approach with one rotation halfway through and the rotational deposition approach with 1-2 revolutions per second (rps).

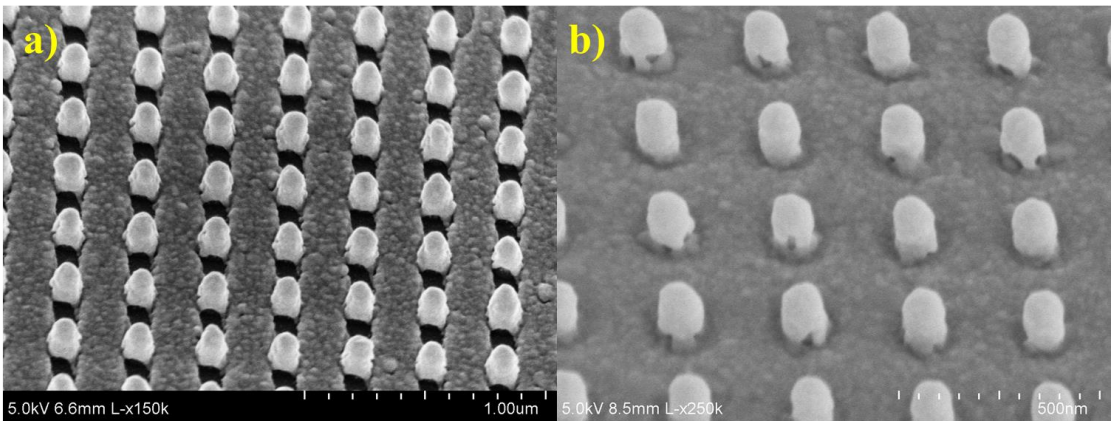

Figure 3-6 SEM images comparing the silver deposition technique on dense arrays. 30-nm of silver is deposited in both cases at an angle of 60°. (a) The angled deposition approach with a rotation halfway through the deposition. The initial pillars were tapered sidewall. (b) The rotational angled deposition approach with 1-2rps. The initial pillars were vertical with 90° sidewalls.

In (a) the initial pillars were tapered and in (b) the initial pillars were vertical. The most

noticeable improvement with the rotational deposition is the reduction in the inter-pillar shadowing. The coverage on the substrate portion is smoother with rotational deposition. Due to the use of vertical pillars, there is some film discontinuity at the base of the pillars, but this is not an issue with the tapered pillars using this technique. In both cases, the nanopillar sidewall is well coated, so the rotational deposition improvements are mainly saving time during deposition and improving the substrate coverage.

3.4 Measurement of the Wavelength Matched Cavity

To test the new wavelength matched cavity, we employed a similar methodology as in Chapter 2.4. The indium concentration in the active region was selected such that the emission wavelength for the nanopillars in the diameter range of 20nm−40nm would be close to 480-nm. Measurements were taken before and after cavity deposition on the same dots to compare the PL Intensity and the TRPL lifetime.[6]

3.4.1 Cavity Fabrication Procedures

The cavity was fabricated using a two-step procedure. First, the 10-nm Al_2O_3 layer was deposited at 200°C using ALD at a rate of 1.05Å/s. Then the silver film was

[6] Tyler Hill assisted in the optical measurements.

deposited in the Cooke E-beam evaporator using the rotational angled stage. The mounting angle of the sample was ~60° and the stage was rotating at a rate of 1-2rps. The programmed deposition thickness of 368Å was calculated such that 30-nm of silver was deposited across the pillar surface. The sample was split into two sections: one for control measurements and one for the silver deposition. Aluminum was not used in this experiment as a comparison, since its effect was previously studied [66].

3.4.2 Measuring the Wavelength Matched Cavity

The QD measurements were performed using the same spectroscopy setup as in Figure 2-14, with the exception of a few filters that were changed to accommodate the new longer emission wavelength. The initial measurements were taken after the Al_2O_3 layer deposition to rule out the contribution of surface passivation. Then, the saturation intensity was identified for the sample of 32-nm diameter QDs. The saturation intensity was 1.415 kW/cm^2, which is double the intensity value necessary for the other wafer. This is attributed to the increased defect density with an increased indium concentration. The PL Intensity measurements were taken with a streak camera, and the TRPL measurements were taken with an APD. Twenty QDs were measured in the control section and twenty QDs were measured in the metal section.

Before proceeding with the metal deposition, the emission wavelength of the 32-nm diameter nanopillars was confirmed using the streak camera, in case cavity design changes needed to be made. This measurement was taken at 1.415 kW/cm^2, since that was the saturation excitation intensity. In addition, lower excitation intensities increased the integration time significantly, as the sample was very dim.

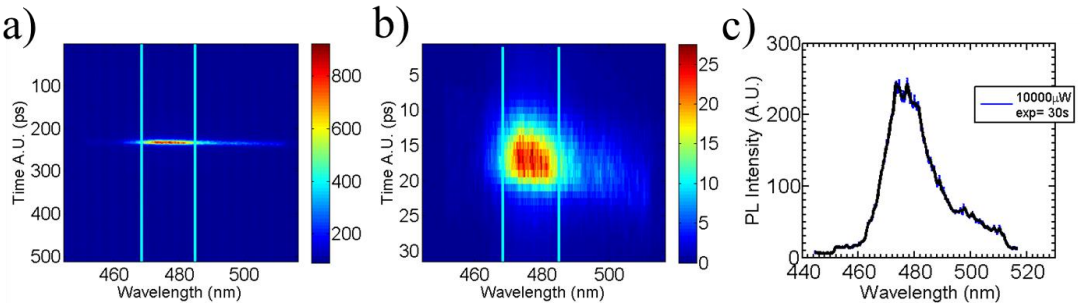

Figure 3-7 PL Intensity measured from a single 32-nm QD nanopillar coated in 10-nm of Al2O3 at an excitation intensity of 1.415 kW/cm^2 or 10000 μW of power focused into a 30-μm diameter spot. (a) The Raw data measured by the streak camera from a 30 second integrated of the emission intensity. (b) Background subtracted data normalized by the exposure time of 30 seconds. (c) PL Intensity spectrum after background subtraction, exposure time normalization, and a moving average to remove spikes. The PL Intensity wavelength is about 480-nm.

The emission spectrum wavelength is localized around 480-nm. The streak camera data is processed, as the exposure time is long and there are significant background counts. The raw data is shown in Figure 3-7(a). After background subtraction and normalization by the 30-second integration time, we arrive at Figure 3-7(b). The data is

summed around the vertical axis to get the total counts per wavelength and a moving average is applied to get the resulting trace in Figure 3-7(c). This procedure is repeated for each of the 40 QDs measured, with varying integration time to account for intensity differences. While the TRPL lifetime can be measured with a streak camera, the lifetimes of the QDs were on the order of tens of nanoseconds, which is longer than the streak camera time ranges for measurement. This is why APDs were used for the TRPL measurements.

Figure 3-8 shows the integrated PL intensity for the 17 QDs measured in the metal section with and without the silver cavity taken at 1.415 kW/cm^2. Only 17 dots are shown because 3 QDs could not be identified after fabrication. The integrated PL intensity is calculated by summing up the PL intensity counts in the post-processed streak camera trace like Figure 3-7(c). The dots are arranged in a histogram to see if there were any trends.

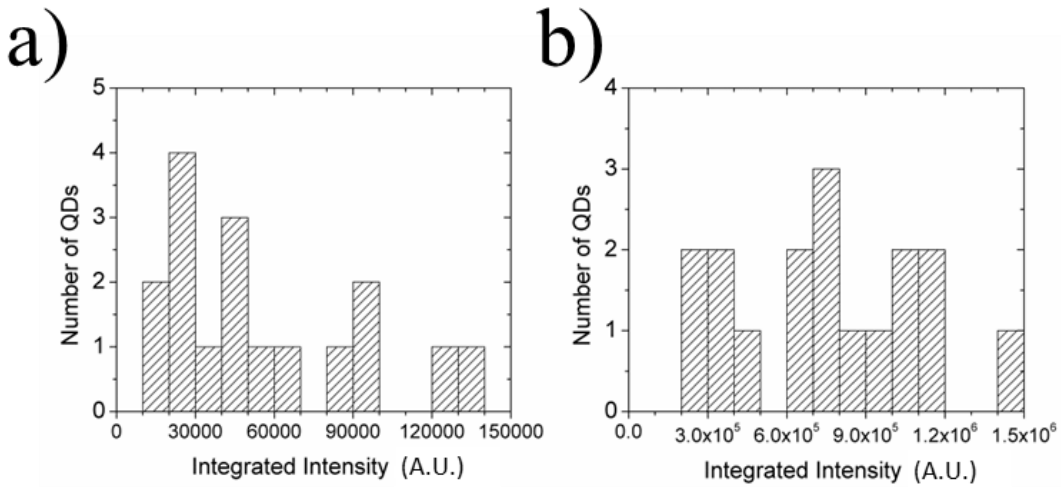

Figure 3-8 Integrated PL Intensity measured from the 17 QDs of 32-nm diameter in the experimental section with an excitation intensity of 1.415 kW/cm^2. The Integrated Intensity is the sum of all the counts in the post-processed streak camera traces. (a) The Integrated intensity for the Al_2O_3 coated QDs. (b) The Integrated intensity after the silver deposition. The data is normalized by the control section intensity.

Inspection of the two histograms shows the PL intensity enhancement is over an order of magnitude. The actual PL enhancement ratio for each dot is shown in Figure 3-9.

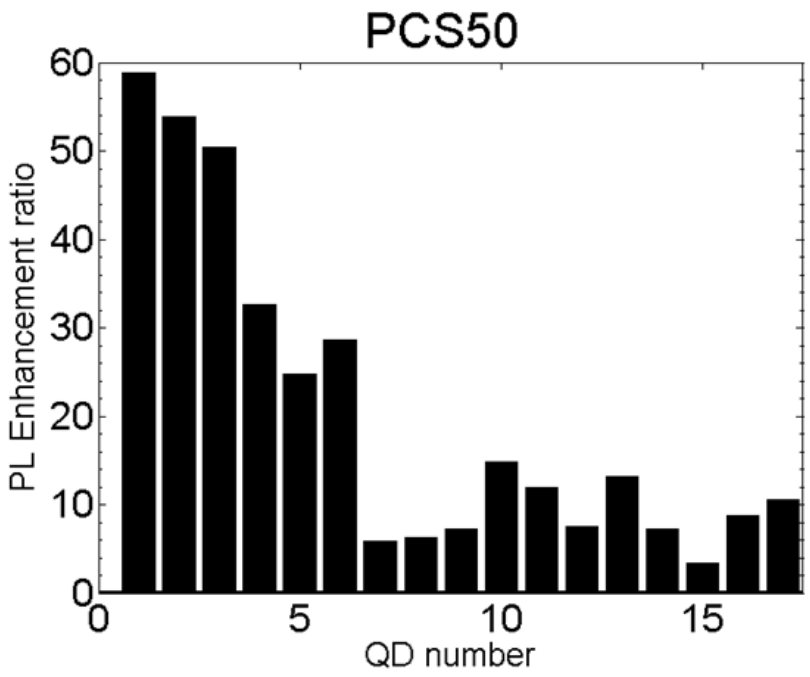

Figure 3-9 Ratio of the Integrated PL Intensity measured from the 17 QDs of 32-nm diameter in the experimental section with an excitation intensity of 1.415 kW/cm^2 taken before and after silver deposition for sample PCS50. The average PL intensity enhancement ratio is ~20. Several QDs had significant PL intensity enhancement.

The average PL enhancement is 20 times, which better than the 7.3 times PL enhancement seen in the previous experiment [66]. Matching the emission wavelength to the cavity resonance wavelength improved the emission enhancement ratio. The improvement in the cavity AQE resulted in more radiation and less metal absorption.

The TRPL data for these QDs was measured using the same APD setup from Chapter 2.4.2. Similarly, the lifetime traces were fit with a bi-exponential decay function and the effective lifetime was calculated as the weighted sum of the two lifetime

components since both weights were significant.

$$\tau_{eff} = W_1 \times \tau_1 + W_2 \times \tau_2 \qquad (3\text{-}1)$$

Using this method, the lifetimes before and after the cavity are shown in the histograms below. The poor radiative efficiency of this sample is the reason for the long initial lifetimes, which also explains why the smaller diameter dots could not be identified using 1.415 kW/cm^2 excitation intensity.

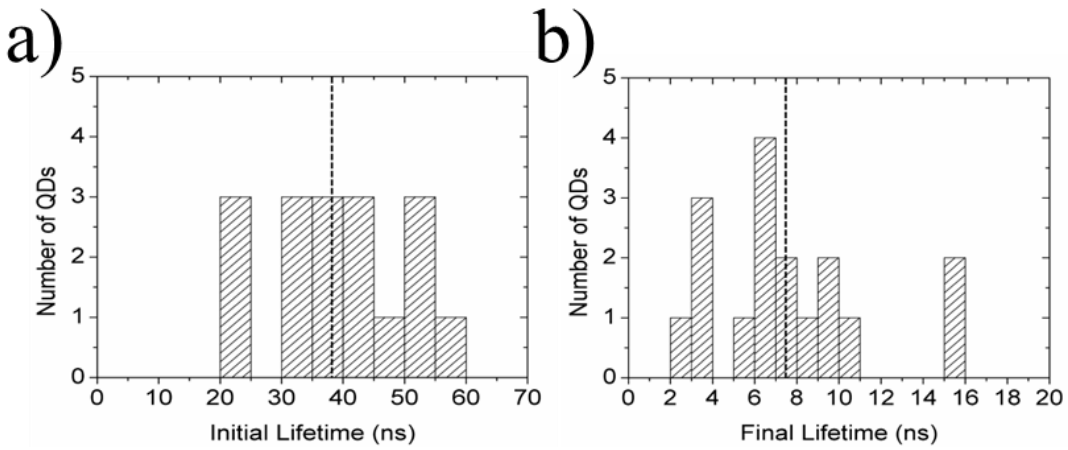

Figure 3-10 TRPL lifetime measured from the 17 QDs of 32-nm diameter in the experimental section with an excitation intensity of 1.415 kW/cm^2. The lifetime is the weighted sum of the bi-exponentially fitted lifetime components. (a) The lifetime for the Al_2O_3 coated QDs. (b) The lifetime after the silver deposition. The dotted line corresponds to the histogram average.

The average effective lifetime of the 17 QDs decreases from ~39ns to 7.5ns. This results in an average lifetime reduction ratio of 5.2 times, which is less than the average of 12

times reduction from the previous experiment. In this experiment, the QDs had more intensity enhancement than lifetime reduction, which is the opposite of what occurred in the first experiment. This can be attributed to the improved cavity AQE at the emission wavelength, resulting in a larger fraction of radiative enhancement with this wavelength-matched cavity. For completeness, the average Purcell factor was 39, which was calculated using equations (2-3) – (2-5), assuming the fill factor ratio is unity at saturation and the collection efficiency ratio is ignored. This is very similar to the previous experiment's average Purcell factor of 46. Thus, for cavities with similar Purcell factor, the cavity AQE will determine the amount of intensity enhancement versus lifetime reduction.

3.5 Quantum Dot Quantum Efficiency Calculations

The spectroscopy experiments measure the strength of the cavity through the lifetime reduction and intensity enhancement ratios, and the experimental Purcell factor can be calculated from this data. However, without a way to measure the QE for the InGaN QDs, the radiative decay rate enhancement cannot be directly measured. The relationship between the decay rates, QE, Purcell factor, and cavity AQE as described in equations (1-10) – (1-14) can be re-written as follows.

$$\Gamma_{tot}^{0} = \Gamma_{rad}^{0} + \Gamma_{NR} \quad (3\text{-}2)$$

$$\Gamma_{tot}^{Ag} = \Gamma_{rad}^{Ag} + \Gamma_{abs}^{Ag} + \Gamma_{NR} \quad (3\text{-}3)$$

$$\Gamma_{tot}^{Ag} = E\eta_0\Gamma_{tot}^{0} + (1-\eta_0)\Gamma_{tot}^{0} \quad (3\text{-}4)$$

$$\eta_0 = \frac{\Gamma_{tot}^{Ag} - \Gamma_{tot}^{0}}{E\Gamma_{tot}^{0} - \Gamma_{tot}^{0}} \quad (3\text{-}5)$$

$$\eta_0 = \left(\frac{\tau_{tot}^{0}}{\tau_{tot}^{Ag}} - 1\right) \Big/ \left(\frac{F_p}{\eta_a} - 1\right) \quad (3\text{-}6)$$

Equations (3-2) and (3-3) are the decay rate for the bare QD and the cavity QD respectively. The decay rate for the cavity QD can be rewritten in terms of the total cavity enhancement E, and the initial QD QE η_0, in equation (3-4). From equation (3-4), solving for the initial QE and substitution of the Purcell factor and AQE are done in equation (3-5) and (3-6), respectively. In order to determine the QD QEs before and after the cavity structure, either the simulated Purcell Factor or cavity AQE must be assumed true. Since the experimental Purcell factor is calculated from the data, the cavity AQE predicted in the simulation is used for the calculation in equation (3-6).

Assuming the cavity AQE of ~0.70 is the true value, the QD QE is calculated before and after the silver cavity and plotted in the histograms below.

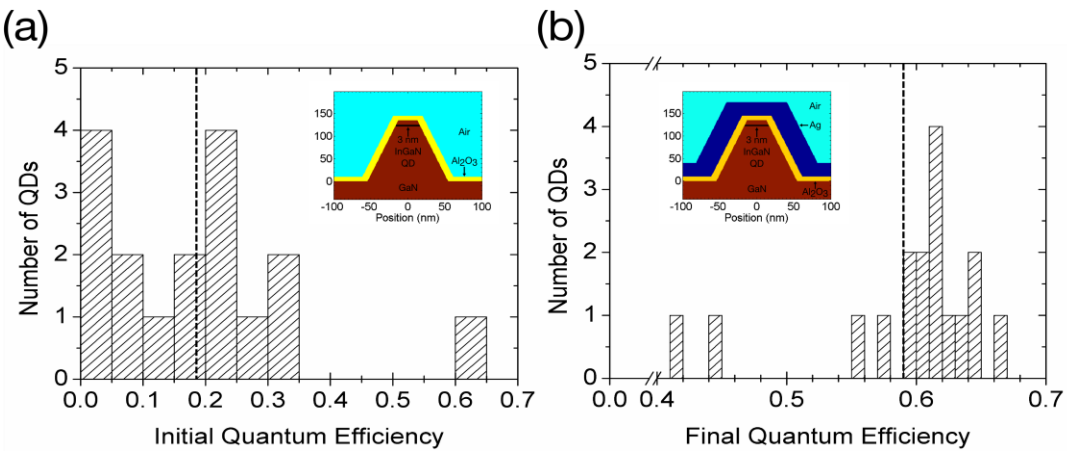

Figure 3-11 The calculated QE of the QDs before and after the silver cavity. (a) The initial QE, with an average of 0.18, as indicated by the dotted line. Each bin is 0.05 in width. (b) The final QE inside the silver cavity, with an average of 0.59. Each bin is 0.01 in width. The insets show the QD schematic for each measurement stage.

The initial QE for this sample is very low, as the average QE for the 17 QDs is only 18%. Except for the one QD, this agrees very well with the low radiative efficiency observation from the experiment. After the cavity deposition, the QE of each QD increases. The upper limit on the final QE is the AQE value of 0.7, which is why no QE is greater than 0.7. As the Purcell factor increases, the final QEs will continue to approach the AQE, with less dot-to-dot variation. Thus, using a high Purcell factor cavity serves as an effective method of homogenizing a group of QDs with different initial quantum efficiencies, which is discussed in more detail in Chapter 4.

3.6 Summary

Angled rotational deposition addressed several of the issues with e-beam deposition on non-flat surfaces. There was a reduction in the number of film discontinuities and improvement in the substrate coating over the previous angled deposition technique. In addition, this technique bridged the gap to coating of vertical pillar structures, expanding the potential nanopillar geometries that we could explore. Plus, it serves as a viable technique of depositing nanopillar LED metal contacts on surface steps [72, 73]. Overall, this technique was critical for improving the fabrication process to generate a better silver film cavity, as precise resonance wavelength and emission wavelength overlap was achieved, resulting in coupling to the high cavity AQE resonance. Improving the cavity AQE increased the average intensity enhancement ratio increased by 2.7 times with a comparable Purcell factor to the previous experiment. It is clear that the QDs are becoming more uniform in QE, as the QE approaches the cavity AQE. With a large enough Purcell factor, homogenous QE emitters can be achieved. This concept will be explored in Chapter 4 with the Open Top Cavity.

Chapter 4

Reducing Dot-Dot variations in Single Photon Sources Using High Purcell factor Plasmonic Cavities

4.1 Introduction

In several quantum-related applications, such as quantum cryptography [56], random number generation, and quantum computing [74, 75], SPSs are a key component. Therefore, the reliable generation of single photons on demand is vital to the devices' success. Traditionally, weak laser pulses have been used as SPS due to the ease of attenuating the laser pulse [76]. However, semiconductor QD based SPS have the advantages of being electrically driven, ultra-compact, scalable, and integration compatible with optoelectronic components. Specifically, III-N QD SPS's have garnered attention due to their ability to operate at room temperature [10, 22], which combined with position control, opens up the opportunity for practical chip-scale SPS.

The problem with strained III-N QDs is that the large piezoelectric field suppresses the oscillator strength compared to the bulk value [77], resulting in slow (<<100 MHz)

and dim SPS. The long QD lifetime limits the modulation rate and data rate for this SPS. In addition, the quantum efficiencies of QD based SPS's can vary considerably from device to device due to the inhomogeneous broadening of the QDs, as in Figure 3-11(a), which contributes to the lifetime variation as well. In order for III-N QD SPS's to be competitive with weak laser pulses based on available telecommunication lasers, these factors must be addressed.

From the previous experiments, the lifetime and QE vary substantially from dot to dot. Figure 4-1 shows the initial lifetime and QE distributions for 19 QDs in Chapter 2.

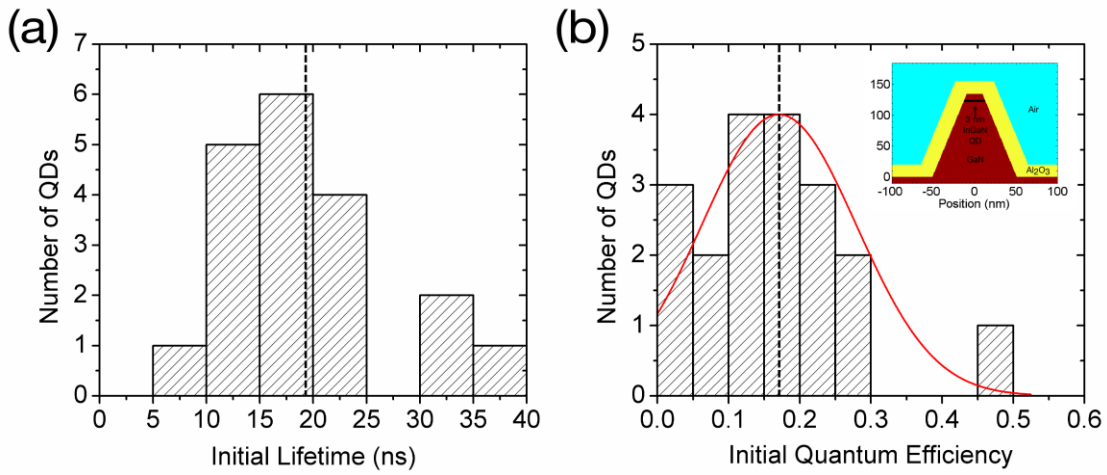

Figure 4-1 (a) The lifetime distribution of the 19 QDs of 28-nm diameter with 20-nm Al_2O_3 coating. The dotted line corresponds to the average lifetime of 19.5 ns. (b) The calculated QE based on the experimental lifetimes and simulated cavity AQE of 0.47. The dotted line corresponds to the average QE of 0.17 with a standard deviation of 0.10. The normal distribution for the QE is shown in red. Inset shows an X-Z cross section of the QD structure measured in the experiment; a 28-nm diameter QD, within a 135-nm tall tapered nanopillar with a 20-nm Al_2O_3 spacer layer [78].

Using the silver film cavity design, the radiative decay rate and the QE have shown significant improvement [66]. The distribution of the QE becomes narrower from a standard deviation of 0.10 before the cavity to a standard deviation of 0.02 after the cavity, and the lifetime becomes shorter.

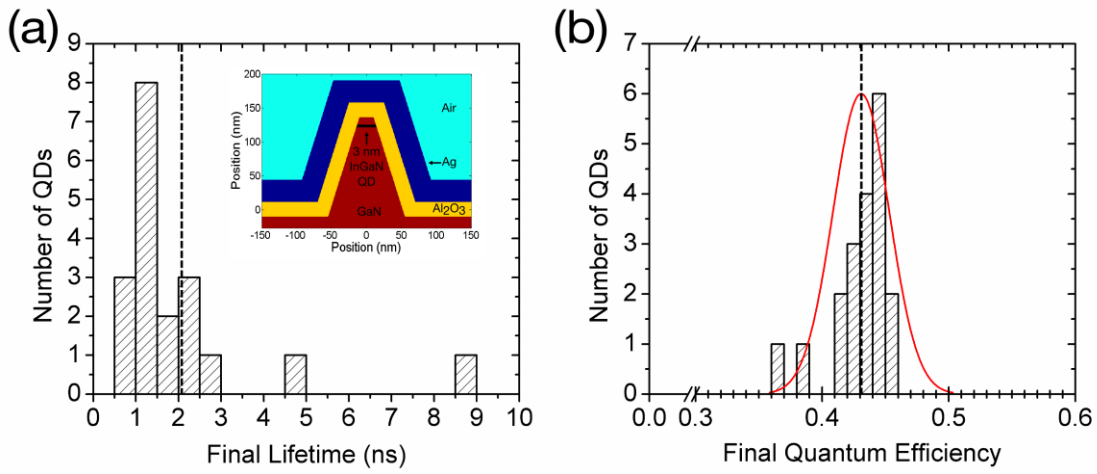

Figure 4-2 (a) The lifetime distribution of the 19 QDs of 28-nm diameter with 20-nm Al_2O_3 coating and the silver cavity. The dotted line corresponds to the average lifetime of 2.05 ns. (b) The calculated QE based on the experimental lifetimes and simulated cavity AQE of 0.47. The dotted line corresponds to the average QE of 0.43 with a standard deviation of 0.02. The normal distribution for the QE is shown in red. Inset shows an X-Z cross section of the QD nanopillar coated in 30-nm of silver [78].

However, the cavity geometry has a practical limit on the magnitude of F_p, which determines how homogeneous the QDs become with the cavity. As F_p is continually increased by reducing the oxide thickness, the cavity AQE will eventually fall below the

initial QD QE and the dots will become dimmer, creating an upper bound for F_p. Another approach to increasing F_p is to use smaller diameter QDs. However, the surface area to volume ratio of smaller QDs creates more non-radiative decay channels, through surface recombination, that suppress QD emission leading to lower QD yield. Thus, the best way to increase the Purcell factor without reducing the cavity AQE or the QE is to change the cavity geometry.

4.2 Open Top Silver Cavity

Inspired by a core-shell nanowire resonator [18], the improved cavity design consists of a vertical nanocylinder encased in a silver film with the top portion of the nanocylinder uncovered. A cross-section schematic of the new geometry is shown in Figure 4-3. A dielectric layer can be inserted between the nanocylinder and silver film to tune the cavity AQE, similarly to the tapered silver film cavity design.

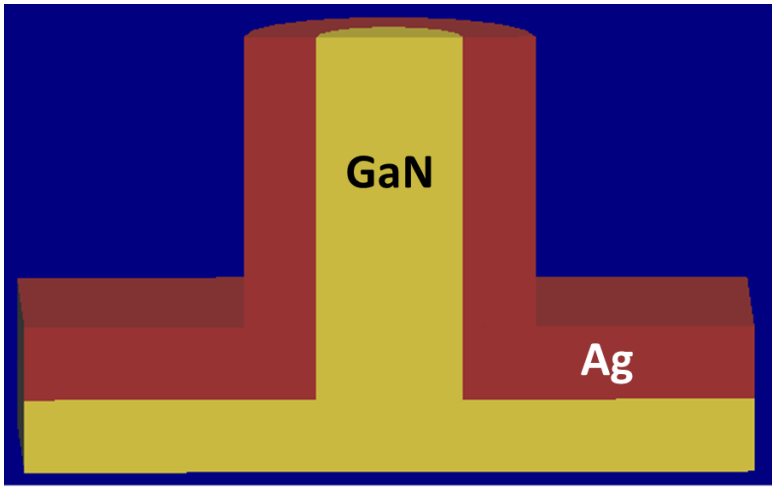

Figure 4-3 Schematic of the Open-Top cavity geometry. The red represents the silver layer, the yellow represents the GaN/InGaN nano-cylinder, and the blue is air. GaN is the substrate.

There are several benefits of the geometry change. First, the change from the tapered pillar to the vertical pillar creates a uniform diameter, reducing the distance from the silver to the QD. The structure is a subwavelength cavity along the vertical direction [79, 80], with one face of the cavity anchored to the substrate, and operates similarly to a zero-mode waveguide [81]. The combination of these two things increases the magnitude of the enhancement to the order of 1000 times. Removing the silver from the top portion of the nanocylinder reduces the metal losses of the structure, increasing the cavity AQE over a silver-capped nanocylinder.

4.2.1 Tuning the Cavity Resonance

Based on the tapered cavity experience, we started with silver film thicknesses in the range of 20nm−60nm. Following the same simulation methodology in Chapter 2.3, the resonance wavelength, enhancement magnitude, and AQE were studied for silver cavities of 20-nm, 30-nm, and 60-nm thicknesses. The silver film is conformal over the entire surface except for the top of the cylinder. Figure 4-4 shows the X-Z cross section of the 60-nm Ag thickness cavity used for simulation. The nanocylinder has similar dimensions to the nanopillar, with a height of 135-nm, a diameter of 25-nm, and a 3-nm thick QW layer located below the 10-nm GaN capping layer. The cavity structure is rotationally symmetric in the X-Y plane. Figure 4.5 shows the radiative decay rate enhancement (Purcell factor) and metal absorption enhancement for each of the silver thicknesses. The sum of the two enhancements is the total enhancement, E, from the structure.

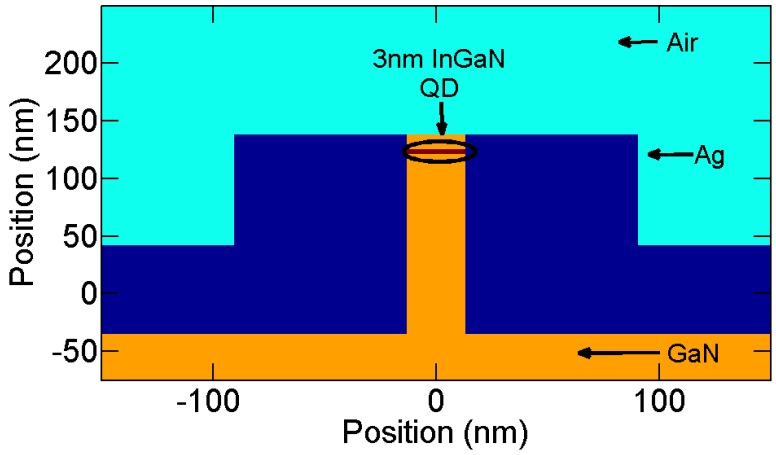

Figure 4-4 An X-Z cross section of the 60-nm thick Open-Top silver cavity coating a 25-nm diameter nanocylinder. The cavity is 360º rotationally symmetric. The QD is located 10-nm below the surface.

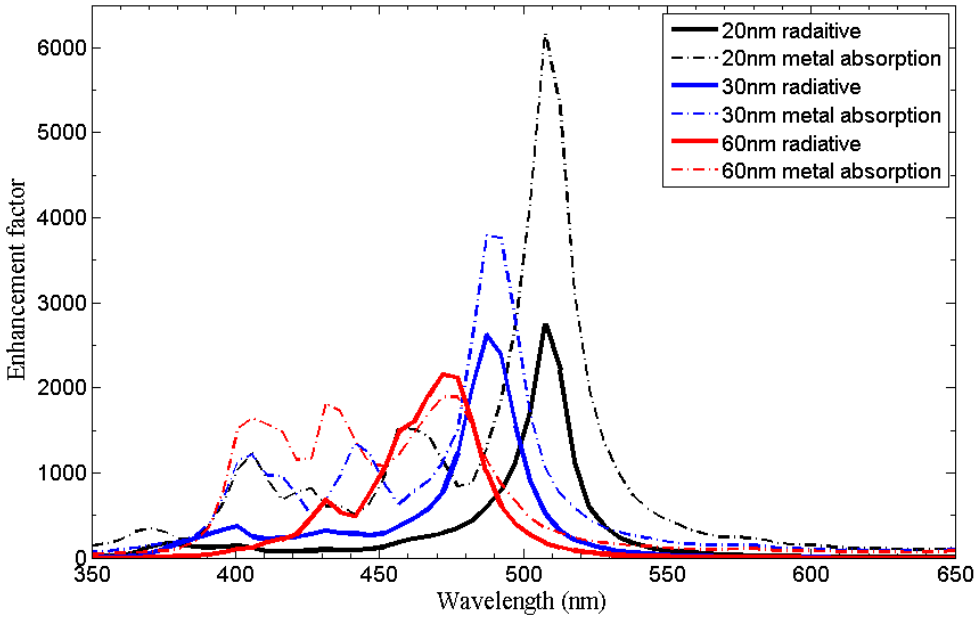

Figure 4-5 An X-Z cross section of the 60-nm thick Open-Top silver cavity coating a 25-nm diameter nanocylinder. The cavity is 360º rotationally symmetric. The QD is located 10-nm below the surface.

Compared to Figure 2-5, the red shift in the radiative enhancement resonance peaks is due to the lack of the Al_2O_3 spacer layer. The metal absorption enhancement is significantly larger than the radiative enhancement for most of the wavelength range, signifying a cavity AQE much less than 0.5. The cavities do however have Purcell factors well above 1000 at the resonance peaks. In order to design a usable open top cavity with a cavity AQE greater than 0.50, the dielectric spacer layer is needed.

4.2.2 Closed Silver Cavity versus Open Silver Cavity

To understand the improvement in the Purcell factor from the closed top pillar to the open top cylinder, four different cavity variations were studied: the closed top pillar from Chapter 2, a closed top cylinder, an open top pillar, and an open top cylinder. The variation in the Purcell factor and cavity AQE with the four shapes allows us to study the effects of open versus closed silver film and tapered versus vertical sidewall.

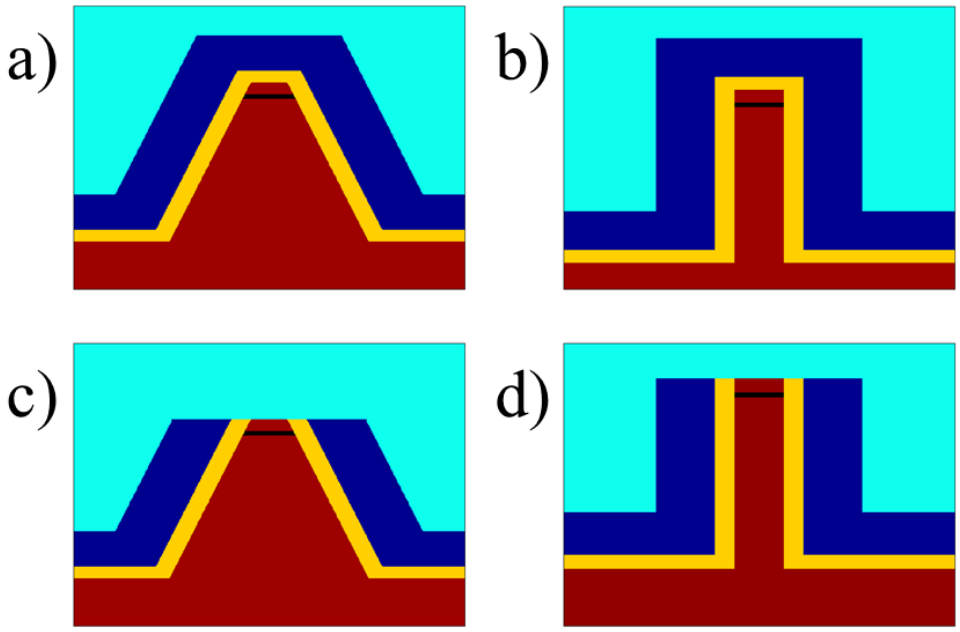

Figure 4-6 X-Z cross section schematics of the four cavity geometries. The diameter of the QD in black is 25-nm, the height of the structure is 135-nm, the Ag (dark blue) thickness is 30-nm, and the Al_2O_3 (yellow) layer is 10-nm. (a) The closed top pillar cavity. (b) The closed top cylinder cavity. (c) The open top pillar cavity. (d) The open top cylinder cavity. The cavity is 360º rotationally symmetric, with the QD is located 10-nm below the surface.

For each of the four structures, the Purcell factor and cavity AQE were simulated with a constant silver thickness of 30-nm versus oxide thicknesses from 0-nm to 20-nm to find the resonance wavelength peak. Although the geometry of the cavity structure and the oxide thickness shift the resonance wavelength peak [28, 71] with each simulation, emission-resonance wavelength matching was assumed true for each case, as the emission wavelength of the InGaN QDs can be tuned with the indium concentration to

match the cavity LSPR wavelength. Therefore, we compared the peak Purcell factor values and the corresponding cavity AQE of each simulation to establish the relationships.

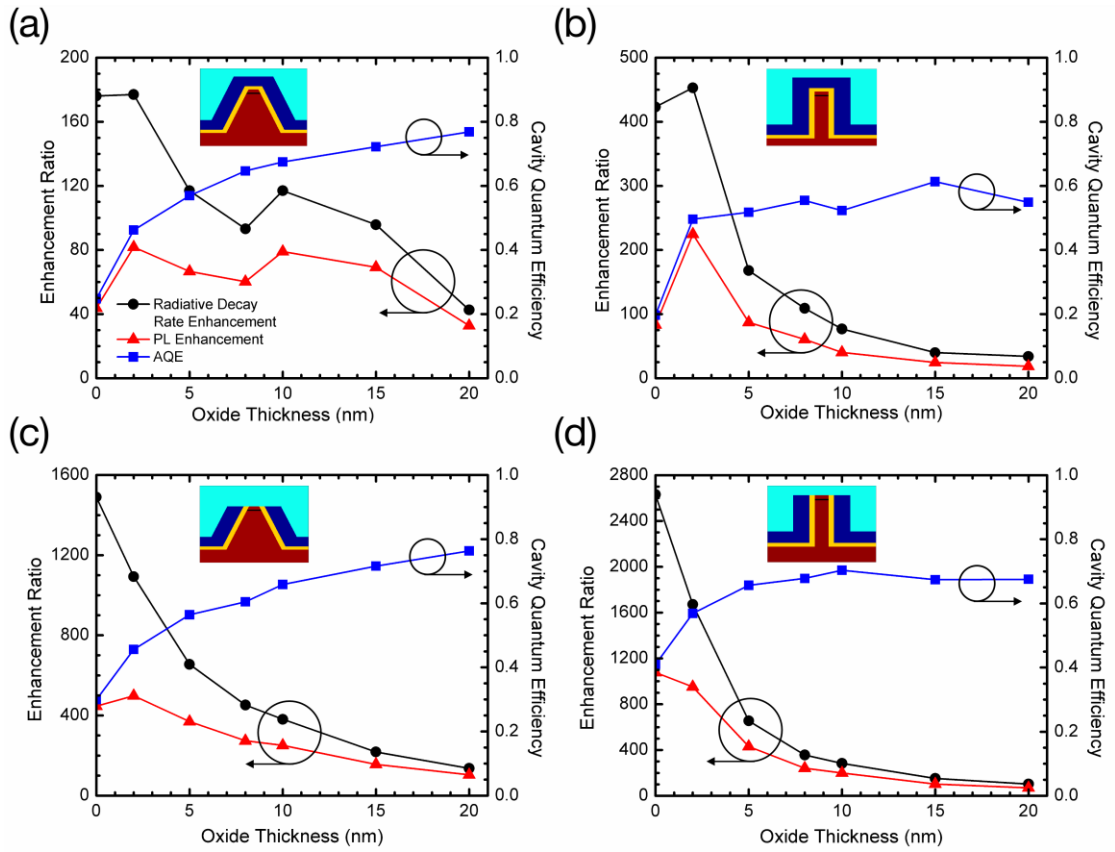

Figure 4-7 The simulated radiative decay rate enhancement and AQE of the lower energy resonance peak for oxide spacer layer thicknesses from 0-nm to 20-nm in the 30-nm Ag film cavity structure. The upper bound on the PL intensity enhancement, which is a product of the radiative decay rate enhancement and the cavity AQE, is shown in red. The inset shows an X-Z cross section of the cavity geometries: (a) Closed Top pyramid, (b) Closed Top cylinder, (c) Open Top pyramid, and (d) Open Top cylinder used in the simulations [78].

Figure 4-7 shows that the cylindrical cavity structures have higher F_p than their tapered pillar counterparts do, which is expected as the zero mode waveguide effect increases the enhancement [81]. Removing the top portion of the metal increases the Purcell factor for both geometries. The open top cylinder cavity has the highest F_p overall. As the oxide thickness is increased for each case, F_p decreases, as the coupling between the QD and the LSPR is reduced with distance. Simultaneously, the cavity AQE increases with Al_2O_3 thickness due to the reduction of metal losses with size. In the cw-pumping limit, the PL emission intensity enhancement ratio from equation (2-1) is proportional to the product of the lifetime enhancement ratio and the emitter final QE. For a large enough Purcell factor, ($F_p \gg 10$), the emitter final QE can be approximated by the cavity AQE, the upper bound of the final emitter QE, as seen in Figure 4-2. Using this approximation, the PL emission intensity enhancement ratio for each oxide thickness is plotted in red. This ratio follows the trend in the Purcell factor, due to the product proportionality, until the cavity AQE drops rapidly when the oxide is removed completely. The open top cylinder cavity has the largest PL intensity enhancement ratio as well. Overall, the open top cylinder cavity offers the best enhancement performance.

4.3 Homogenizing the Quantum Efficiency

To simulate the effect of each of the four cavities on the QD lifetime and QE distributions, the expected final lifetimes and quantum efficiencies were calculated for the original 19 QDs measured in Figure 4-1. Because several oxide thicknesses were examined for each cavity type, a qualifying criterion was necessary for choosing the appropriate oxide spacer thickness. The metric for determining the appropriate oxide thickness was a cavity AQE of at least 70%. Reducing the metal losses in the system is critical to reduce photon losses, so the highest realistic cavity AQE was chosen for the criterion. For the cavity designs with multiple oxide thicknesses corresponding to a cavity AQE greater than 70%, the thickness associated with the highest F_p was chosen. For the closed top cylinder cavity in Figure 4-7(b), in which the cavity AQE does not reach 70%, the oxide thickness corresponding to the highest cavity AQE was chosen. Again, the emission wavelength of the initial InGaN QDs is ignored, as it can be correctly matched for the experiment. The resulting Al_2O_3 spacer thickness chosen for every cavity except the open top cylinder structure was 15-nm. For the open top cylinder, 10-nm of oxide was chosen. These oxide thicknesses correspond to Purcell factors for the four cavities of 96, 40, 218, and 283 respectively in the same order of the cavities in Figure 4-7. The cavity AQEs of these Purcell factors were 72%, 61%, 71.6%, and 70.3%, respectively. Since the

upper bound of the final QE is set to be ~70%, the variation in the F_p values for the different cavities will determine the distribution of the final lifetime and QE. As F_p increases, the distributions will have smaller deviations, illustrating homogenization of the QDs.

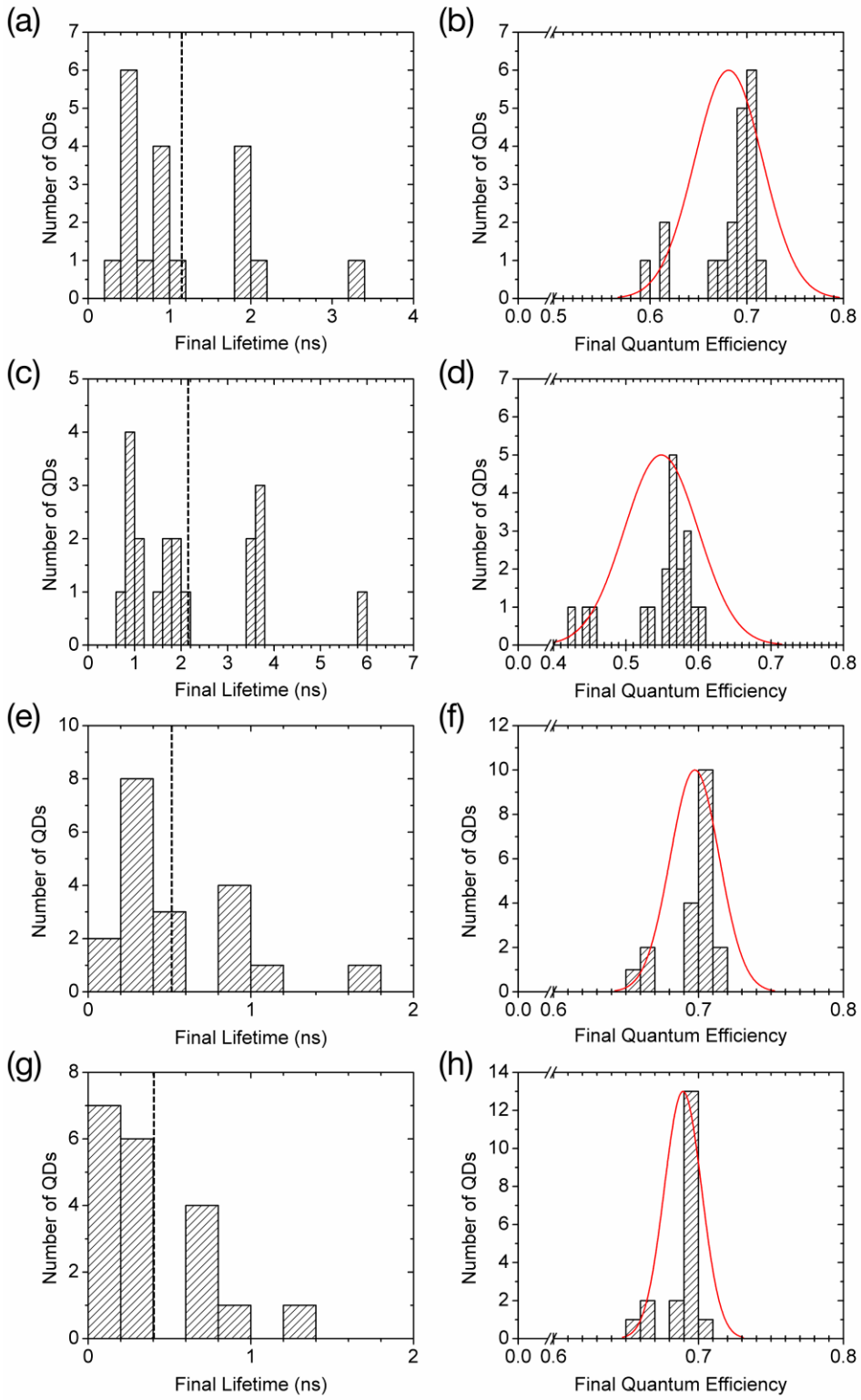

Figure 4-8 Final emitter lifetime distribution and the QE distribution for the 19 InGaN QDs inside of the respective cavities. For the lifetime distributions, the dotted black line indicates the average lifetime. The red curve in the QE distributions shows the normal

distribution of the QEs. (a, b) Closed Top pillar, (c, d) Closed Top cylinder, (e, f) Open Top pillar, and (g, h) Open Top cylinder. The final lifetime average of the four cavity types are 1.16 ns, 2.19 ns, 0.53 ns, and 0.41 ns respectively. As the Purcell factor is increased, the final lifetime average decreases, and the distribution of the QE becomes narrower [78].

Using the above values for F_p and cavity AQE, Figure 4-8 shows the calculated final lifetime and final QE distributions for each cavity type, assuming the distribution of the original 19 QDs as the starting point. The average lifetime of the QDs in the cavities is reduced from 19.5 ns to 1.2 ns, 2.2 ns, 0.53 ns, and 0.41 ns, respectively. The average QE of the QDs improves from 0.170 to 0.681, 0.548, 0.697, and 0.689, respectively. The lifetime reduction increases as F_p increases, since the total lifetime reduction is directly related to the radiative decay rate enhancement. As F_p increases, the standard deviation of the final QEs from the average value shrinks. For the open top cylinder with the Purcell factor of 283 and AQE of 0.7033, the average and standard deviation of the QE distribution are 0.689 and 0.012, respectively. The quantum efficiencies of the QDs are becoming more uniform, which can be observed comparing Figure 4-1(b) and Figure 4-8(h), as standard deviation was reduced by a factor of 8.75 to 1.2%, narrowing the distribution significantly. Thus, each QD is closer to having the same probability to produce a photon when excited. To account for the differences in the lifetimes, the

repetition rate for excitation just needs to be longer than the longest QD lifetime.

Homogenization of the QDs requires a large F_p, and a high AQE is necessary to ensure that the QDs QE improves. With these two factors, an array of QDs each will have the same probability to emit a photon. The open top cylinder cavity is the best of the four options for homogenizing a group of InGaN QDs due to its large (>100) F_p and AQE over 70%. However, up to this point, we have considered perfect metal film thicknesses of 30-nm, in the above calculations. During metal deposition, there can be thickness variations across the sample due to the 90° angle of the cylinders; so, we examined the effect of metal thickness variation on the F_p and cavity AQE. To study this effect, we assumed that the resonance peak wavelength of 487-nm for the 30-nm Ag, 10-nm Al_2O_3 open top cylinder was also the emission wavelength of the InGaN QDs. The structure cross section is in Figure 4-6(d). The nominal simulation of 30-nm Ag for the F_p and cavity AQE is shown in Figure 4-9. As expected, the structure has two resonance peaks, due to the core-shell geometry. The high-energy resonance is located around 390-nm, similarly to the closed top cavity structure, and is not of interest in this experiment. The low energy resonance, at 487-nm, will shift with the metal thickness, resulting in a different F_p and cavity AQE at that wavelength.

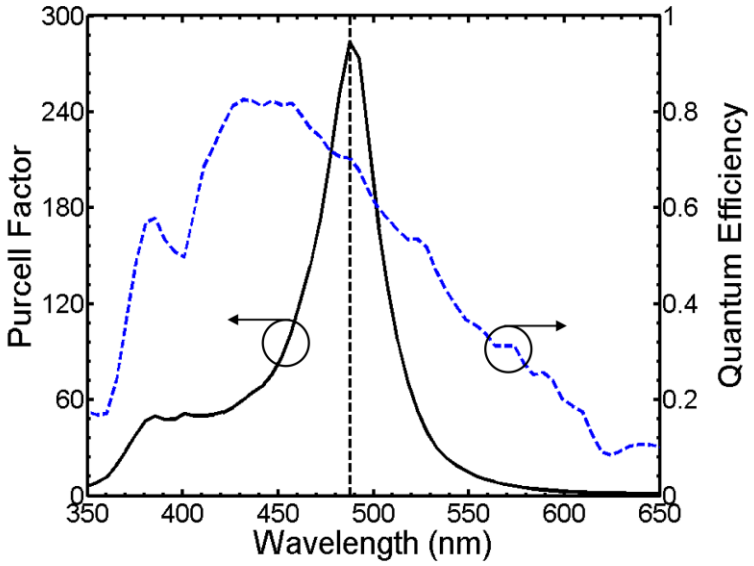

Figure 4-9 Simulated radiative decay rate enhancement (Purcell factor) and cavity AQE for the open top cylinder, consisting of 10-nm thick Al_2O_3 spacer and 30-nm thick silver cavity on a 25-nm diameter QD. The resonance peak is at about 487-nm wavelength and the corresponding AQE is ~70.3% [78].

Then, the metal thickness in the simulation was varied to 30-nm $\pm$ 2-nm from 28-nm−32-nm, where 2-nm was derived from previous deposition experience on vertical sidewalls. For 28-nm and 32-nm of silver, the corresponding Purcell factors at the 487-nm wavelength were 296 and 257, respectively. The magnitude of the variation between these values and the nominal F_p value of 283 is less than 10%.

While the effect of the metal thickness variation on the Purcell factor is small, the effect on the final lifetime distribution and the final QE is more important as it illustrates how homogenous the QDs will become. Figure 4-10 shows the final lifetime and final

QE distributions in Figure 4-8(g, h) with the addition of the metal variations. The red curves correspond to the normal distribution for the 19 QDs, and the dashed blue curves correspond to the normal distribution, evenly weighted among the three metal thicknesses studied of 28-nm, 30-nm, and 32-nm.

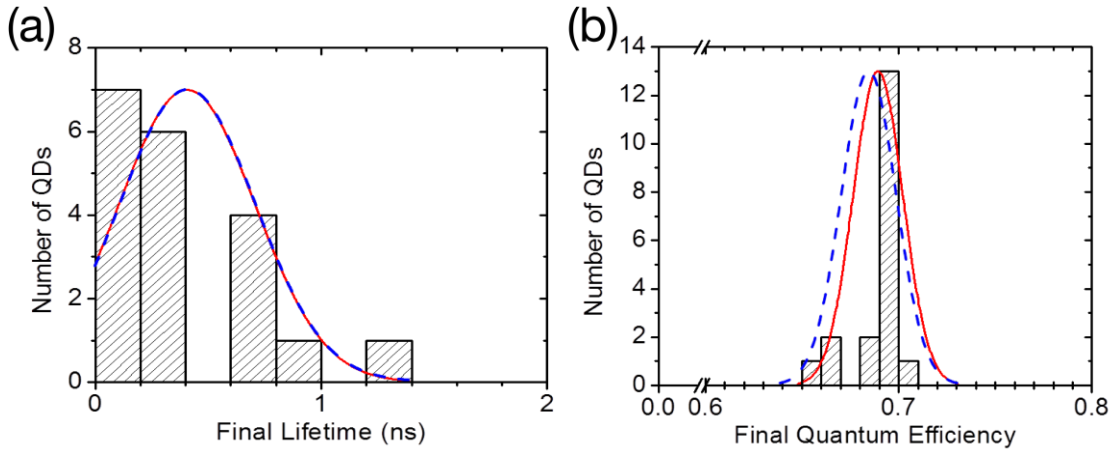

Figure 4-10 (a) The final lifetime distribution of the 19 experimental QDs in this cavity configuration. The normal distribution is in red and the distribution including the metal variation from 28-nm to 32-nm thickness is in blue. The overlap shows the cavity's performance is tolerant to fabrication variation. (b) The final QE and the normal distributions for the nominal thickness of 30-nm Ag in red and the metal thickness variation from in blue. The peak wavelength of 487-nm is used to calculate the metal variation effect on the Purcell factor and QE [78].

The average lifetime for the nominal metal thickness distribution is 410 picoseconds. The change in the average lifetime induced by the fabrication variations is 5 picoseconds, which is less than 2% difference. Similarly, for the final QE there was a 1.3% change in

the average value from 0.6975 to 0.6848, while the standard deviation of the QE remained unchanged at 0.013. The cavity's tolerance to metal deposition fluctuations is due to the magnitude of the Purcell factor. Even with long initial QD lifetimes ($\approx 20ns$), lifetimes on the order of hundreds of picoseconds can be achieved with this cavity, pushing the modulation frequency into the tens of Gigahertz. Thus, the open cylinder cavity is a fabrication stable method for achieving high enhancement and QD homogenization.

4.4 Open Top Silver Cavity Fabrication

Fabrication of the open top cylinder cavity is a multi-step process that involves manipulation of the nanopillar shape and silver film coverage. Using our developed nanopillar fabrication process, the nanopillar is tapered along the sidewall after dry etching. In order to generate a vertical cylinder, an anisotropic wet etch of GaN by a buffered KOH solution, AZ400K, is used. This etching process has been explored and used to fabricate GaN nanowires for LED and laser applications [82]. The wet etch attacks the angled GaN plane at a much higher rate than the vertical or horizontal planes, resulting in a diameter shrinking process as the diameter of the base approaches the top diameter. SEM images comparing the nanopillar array before and after 20 minutes of wet

etching is shown in Figure 4-11.

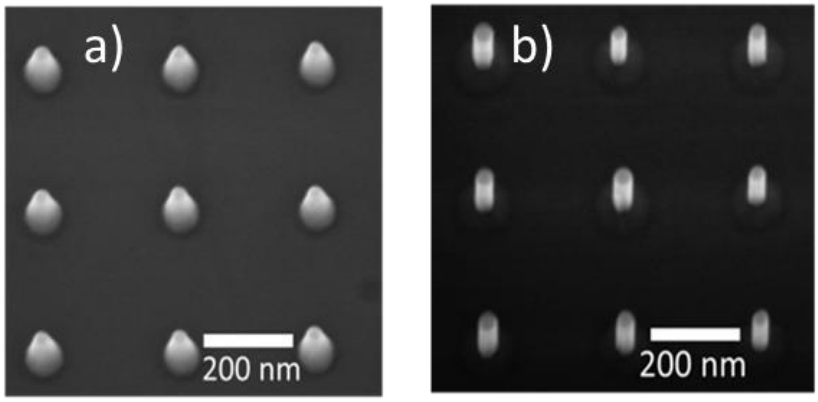

Figure 4-11 SEM images of (a) nanopillar after dry etching GaN and (b) nanocylinder after wet etching of GaN for 20 minutes in AZ400K.

In addition to changing the nanopillar shape, the wet etch removes the plasma-damaged GaN regions from the ICP-RIE etching. This results in nanocylinders that have improved PL intensity and less non-radiative decay due to surface states [25, 83].

After, the wet etching process, the Al_2O_3 spacer layer is deposited using ALD (Oxford ALD), at 250°C. Then, the 30-nm silver layer is deposited to form the cavity structure. We investigated both e-beam evaporation and sputtering techniques for silver deposition, which will be discussed in more detail in section 4.4.1. Next, the sample is planarized and etched back to the top of the silver layer using RIE dry etching. Finally, a silver dry etching recipe is used to remove the top portion of the silver film, exposing the

nanocylinder tip. The schematic of this process is in Figure 4-12.

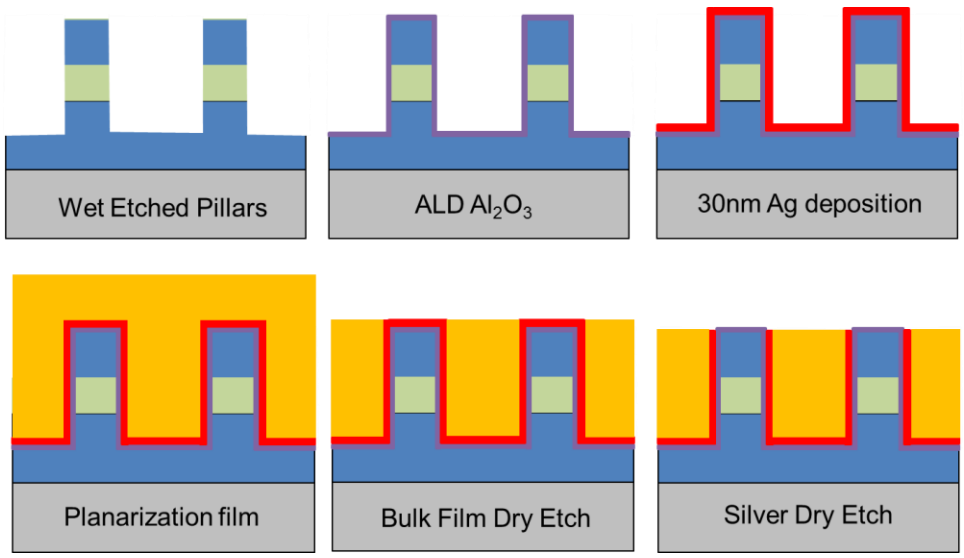

Figure 4-12 The six fabrication steps for the open top silver cavity. The nanopillars are wet etched into nanocylinders. The cylinders are coated with Al_2O_3 and Ag. A planarization film is used make the sample flat for dry etching. The top silver is removed using dry etching [78].

4.4.1 Aluminum Doped Silver Sputtering

Four silver deposition techniques were explored to determine the best approach to create a conformal metal layer without the use of ALD. The four techniques are angled deposition with manual rotation, angled rotational deposition, high voltage silver sputtering, and aluminum and silver co-sputtering. Figure 4-13 shows an SEM comparison of samples from each of the deposition techniques.

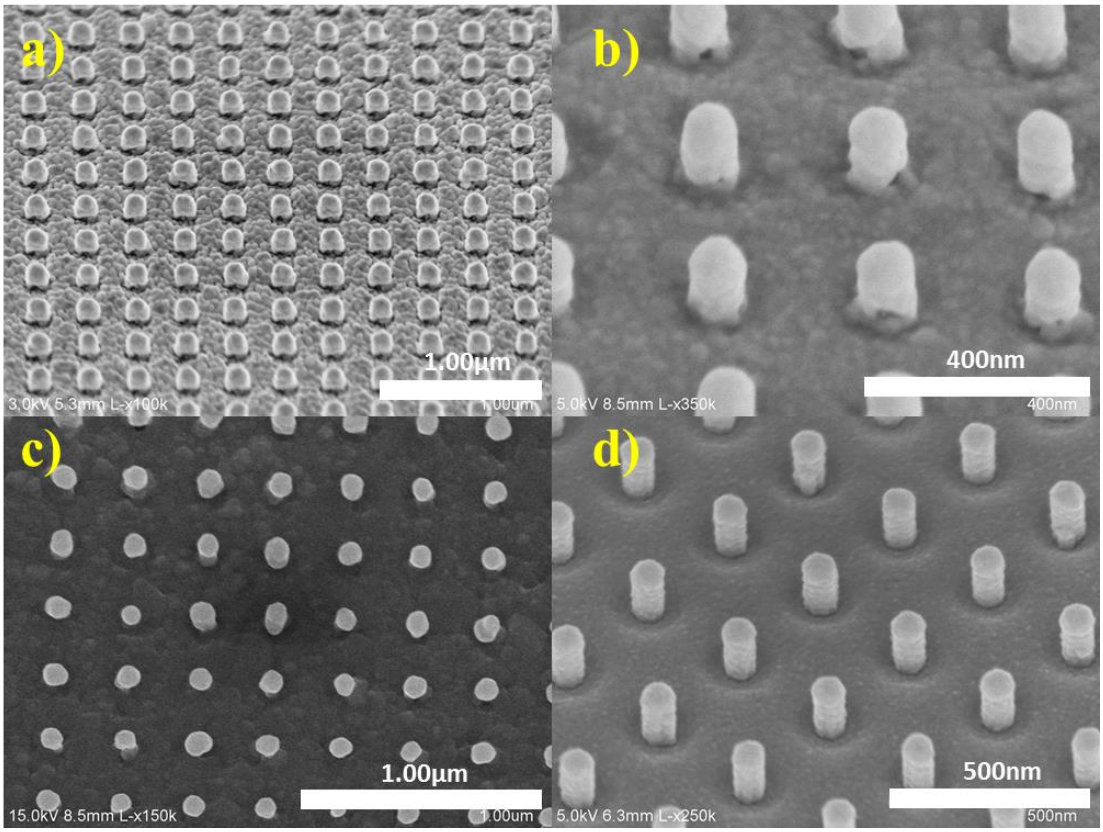

Figure 4-13 SEM images of the silver deposition onto the vertical nanocylinder arrays. (a) Angled e-beam deposition with four manual turns at a mounting angle of ~76°. (b) Rotational Angled e-beam deposition with a speed of 1-2 rps at a mounting angle of ~60°. (c) Sputtered silver at normal incidence. (d) Co-sputtering of silver and aluminum at normal incidence. The aluminum helps smooth the surface roughness [84].

Angled deposition with manual rotation, the first method explored, is the simplest. The sample was mounted in the evaporation chamber on a 76° angled wedge and physically rotated after deposition on one side in a star pattern a total of four times to create a four-sided deposition. Because of the manual rotation, there are gaps in the film coverage due to the shadowing within the array. In addition, the film is very rough and uneven.

Moreover, the coverage on the vertical pillar is rounded and non-conformal. The rotational angled deposition, corrects many of the issues caused by the manual rotations in the previous technique. The substrate roughness is reduced and the gaps in between the pillars are filled with silver. However, as well as this technique works for tapered pillars, the vertical pillars still suffer from some film discontinuities at the bottom of the structure.

To overcome the limitations of evaporation on vertical surfaces, sputtering was tested as a deposition technique. With film sputtering, the deposition rates are lower than evaporation, but there is natural deposition on vertical structures. By increasing the bias voltage during deposition, the ratio between vertical coverage and substrate coverage is increased. At a bias potential of 600V, the ratio was 1:3 for the standard silver sputtering recipe. Unfortunately, this was not a high enough ratio, as the film needs to be conformal in order for the open top cavity to function as intended. Co-sputtering aluminum with silver solved the silver coverage issue. The co-sputtering process reduces the grain size on the surface and improves the film coverage and uniformity over the cylinder surface. The details of the sputtering procedure can be found in Zhang [84]. The incorporation of aluminum into the silver recipe is done at a low fraction such that the optical properties of the silver film are not significantly perturbed [85, 86]. Using this approach, 30-nm of Ag

was deposited on the vertical sidewalls after 66 seconds of sputtering at a rate of 9.37Å/sec. This gave the highest sputtering deposition ratio of ~1:2. Although the ratio was not 1:1, the benefits of this deposition technique in terms of film coverage outweighed the poor conformal approximation. In future work, ALD of silver films would be the best solution for a conformal deposition technique.[7]

4.4.2 Removing the Top Silver

Fabrication of the open top in the silver film requires targeted removal of the silver from the top of the cylindrical structure. Silver films can typically be removed from the surface using either wet etching or dry etching. Because silver covers the entire surface, the sample must be coated in a sacrificial layer that only exposes the intended etch region. With wet etching, the film tends to peel from the edge of the sample lifting off all the layers instead of etching in a traditional manor, since the silver thickness is less than 100-nm. This left dry etching as the alternative etching approach. Dry etch of silver is an RIE process that uses CF_4 and Ar plasma. The CF_4 creates a byproduct with the Ag [87], and the Ar^+ ions physically bombard the sample, removing the byproduct in addition to the other film layers. The two silver etching recipes used at CF_4 and Ar^+ at 9-mTorr and

[7] Cheng Zhang performed Al-doped Ag sputtering.

500 Watts with 4:1.5 and 1:4 sccm flow rates respectively. The recipes were alternated in 1-2min intervals to create silver byproduct and remove silver byproduct. The high power and low pressure are important to help maintain the vertical etching profile without damaging the sidewall or substrate Ag. Due to silver hardness, alternating the recipes gave the best etching results. With a physical based dry etching recipe, the sacrificial layer is important, as the etching chemistry does not discriminate against material composition. While several different materials were considered for the sacrificial layer, only two are worth mentioning: Spin-on-Glass (SOG) and silicon dioxide (SiO_2).

4.4.3 Spin-On-Glass Planarization

SOG is an attractive chemical for its planarization capabilities. SOG is spun onto a sample and cured to remove the solvents from the material, creating a glass like film. Using a photoresist spin process, the surface of the SOG layer is planar across the sample. With a spin speed of 3000 rpm, the resulting SOG thickness after the 1-hr baking at 425°C in Nitrogen ambient is 500-nm.This layer protects the silver layer, and allows for conformal dry etching of the SOG layer down to the top silver interface. Because SOG is a glass like film, it etches with conventional silicon dioxide etching recipes, comprising of fluorocarbons. Once the top surface of the nanocylinder is exposed, the silver etching

recipe is employed until the cylinder is exposed.

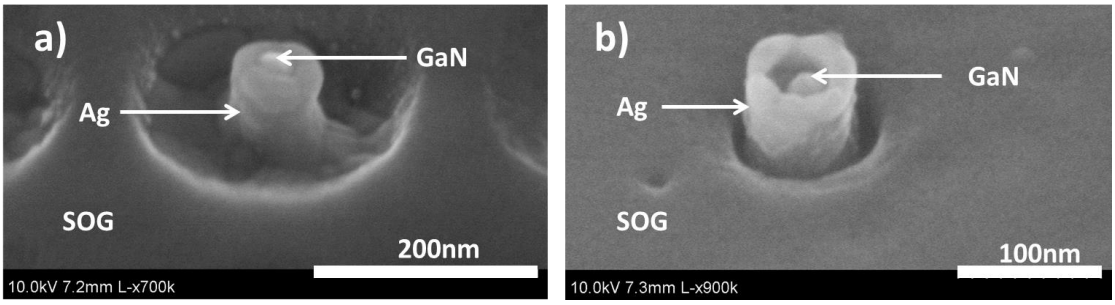

Figure 4-14 SEM images of the open top silver cylinder cavity using SOG planarization. (a) A nanocylinder from a dense array with 300-nm spacing. (b) A nanocylinder from a sparse array with 5-μm spacing between structures.

After the SOG etch back and the silver etching, the top of the nanocylinder can be seen clearly from this process. Most of the silver coated pillar is exposed from the SOG as the silver etch attacks the SOG layer simultaneously at a faster etching rate than the silver film. Because the SOG planarized the sample, this etch very controllable, and due to the high material contrast under SEM, the etch rate can be monitored effectively. While the structure appeared to come out successfully under SEM, it was later discovered during measurement that SOG has undocumented emission around the emission wavelength of the sample (460-nm-500-nm), which interfered with PL intensity measurements for the cavity. This would require redesigning the cavity structure and emission wavelength to overcome, so pure silicon dioxide was explored.

4.4.4 Silicon Dioxide Planarization

Unlike SOG, SiO_2 can be cannot be deposited using a spin process to aid in planar coverage. Plasma Enhanced Chemical Vapor Deposition (PECVD) SiO_2 is not desirable because the film coverage is conformal and not planar. Thus, e-beam evaporation of SiO_2 was the only method to achieve pseudo planar film coverage. Using angled rotational deposition with the sample mounted at an angle of ~60° and a rotation speed of ~1-2 rps, 550-nm of SiO_2 was deposited at a rate of 15Å/sec on top of the silver covered cylinders. With the angled rotational deposition, the film encases the underlying cylinders. This is viewable after etching through the bulk layer in Figure 4-15(a). The etching behavior of the SiO_2 from the SOG was studied in the previous section, so, the transition to etching pure SiO_2 only adjusted the etching rate, since SOG has additional impurities.

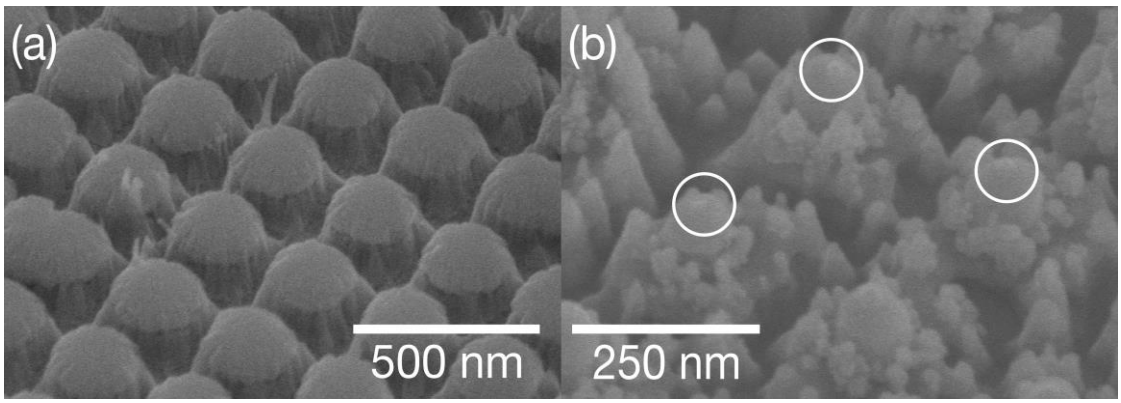

Figure 4-15 SEM images of the open top silver cylinder cavity using SiO_2 planarization.

(a) A nanocylinder dense array with 300-nm spacing coated in SiO_2 that is etched down for 12 minutes and 40 seconds into encasing shells around the nanocylinders. (b) The same array after silver etching. The white circles indicate the nanocylinders in which the tip is exposed through the silver [78].

Etching through the SiO_2 layer for 9.5 minutes caused protective shells to appear around the cylinders. After 12 minutes and 40 seconds of etching, the SiO_2 looks like Figure 4-15(a). Once the shell tops were etched through, the silver etch recipe described above was used to remove the top silver layer. The places where the nanocylinder tops were exposed are highlighted in the white circles in Figure 4-15. The residual SiO_2 was left on the sample, as the methods for removing SiO_2, including dipping the sample in buffered hydrofluoric (BHF) acid, could affect the silver layer. The evaporated SiO_2 does not produce any emission in the wavelength range of interest, so it does not affect the PL emission spectrum. Since this method successfully exposed the nanocylinder top and does not affect the PL spectrum, it was the method used in the experiment to test the open top cavity.

4.5 Experimental Cavity Design

In order to validate the simulated parameters, an open top cavity was fabricated and measured using the spectroscopy setup in Figure 2-14. Several changes to the parameters

in the nominal design were made based on the experimental details below.

4.5.1 Sample Parameter Adjustments

Initially, a 135-nm tall nanocylinder sample was fabricated with diameters ranging from 24-nm to 48-nm in increments of 4-nm in order to verify the emission wavelength of the wafer. For this wafer, the InGaN 3-nm thick active region is located 10-nm below the surface. The indium concentration was high enough such that the wafer gave off red emission under excitation. The nanocylinders were measured at the previously used laser powers of 2000 μW and 5000 μW, which correspond to 283 W/cm^2 and 707 W/cm^2, respectively.

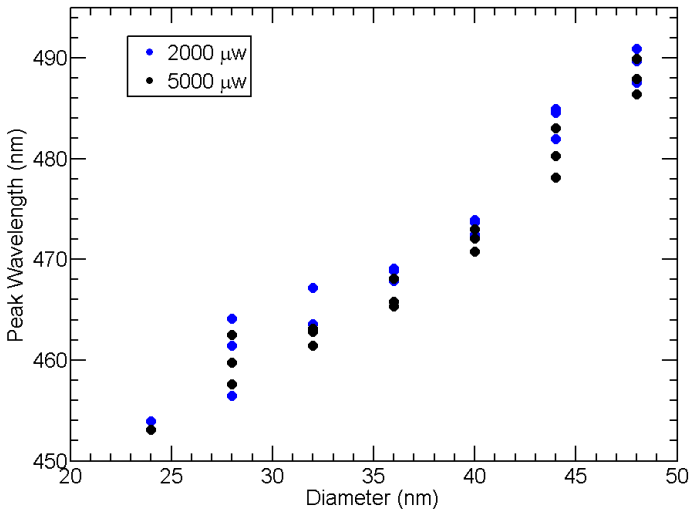

Figure 4-16 Peak emission wavelength versus nanocylinder diameter measured at two laser excitation powers, 2000 μW (283 W/cm^2) and 5000 μW (707 W/cm^2). Up to three

arrays are measured at each diameter for comparison.

The larger diameter nanocylinders (40-nm, 44-nm, and 48-nm) emitted closer to the 480-nm design wavelength, than the smaller desired diameters (24-nm and 28-nm). To account for this, the Al_2O_3 thickness used in the experiment was decreased to 2-nm to blue shift the resonance peak, better matching the emission wavelength. With a 2-nm Al_2O_3 layer, the Purcell factor increases ~6 times, the cavity QE decreases by ~13%, and the resonance wavelength shifted from 487-nm to 477-nm for a 25-nm diameter QD compared to the 10-nm Al_2O_3 layer in Figure 4-9.

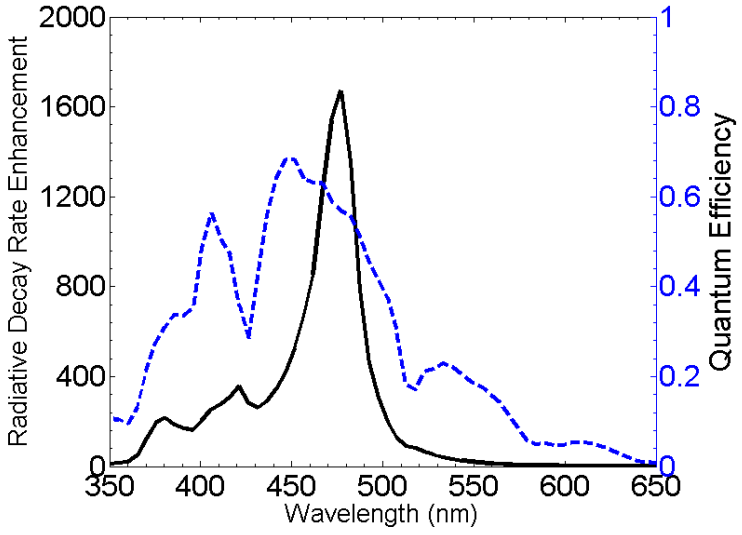

Figure 4-17 Simulated radiative decay rate enhancement (Purcell factor) and cavity AQE for the open top cylinder, consisting of 2-nm thick Al_2O_3 spacer and 30-nm thick silver cavity on a 25-nm diameter QD. The resonance peak is at about 477-nm wavelength and the corresponding AQE is ~57%.

Because the anticipated initial QE for the QDs emitting around 480-nm is low from previous experience in Figure 3-11(a), using a cavity with a AQE of ~50% should still suffice to enhance the QE and the PL intensity. This was the only design change made before fabrication.

4.5.2 Measurement Details and Procedures

For the experiment, the sample was divided into two regions: the control section for intensity calibration and the cavity section. ALD was used to deposit 2-nm of Al_2O_3 across the entire sample.[8]

[8] Tyler Hill helped with the optical measurements

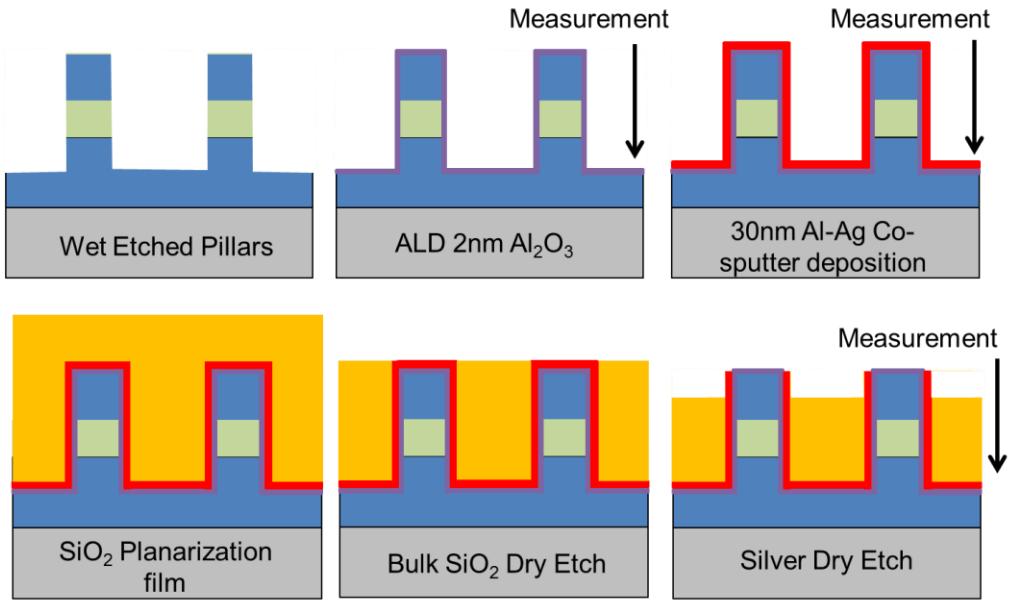

Figure 4-18 The six fabrication steps for the open top silver cavity. The nanopillars are wet etched into nanocylinders. The cylinders are coated with 2-nm of Al_2O_3. 30-nm of aluminum doped Ag is sputtered on the sample. A SiO_2 planarization film is used to protect the silver during dry etching. The top silver is removed using CF_4:Ar^+ dry etching. The measurement arrows indicate the three laser measurement steps for the experiment [78].

The same cylinder diameters from Figure 4-16 were included on this sample. In order to characterize the cavity effect, PL measurements were taken at three fabrication stages, as indicated in Figure 4-18: after oxide deposition, after silver sputtering, and after silver top removal. For the PL measurements, the sample was optically excited from the front (metal cavity) side of the sample with a 390 nm wavelength femtosecond pulse laser focused to a 30-μm diameter spot, with an incidence angle of 55° from normal incidence. The PL signal was collected from the same side as the incident light with a 0.6NA

objective lens and all of the measurements were taken at 10 K. TRPL measurements were taken with the streak camera due to the lifetime time range, and a CCD camera was used for the PL intensity measurements. Due to the low PL intensity from the individual QDs in the sparse arrays, the dense arrays of ~10,000 QDs were used for this experiment.

The sample was fabricated using the Aluminum doped silver and the Silicon dioxide planarization and etch back procedure. To ensure no metal contamination of the control section, it was covered in a 3-μm thick layer of SPR 220 (3.0) photoresist for protection. Using aluminum doped silver sputtering, 30-nm was sputtered on the vertical sidewalls with 66 seconds of sputtering at a rate of 9.37 Å/s, confirmed using SEM and surface profilometry. For the top silver etching, 550-nm of SiO_2 was evaporated using angled rotational deposition with a sample-mounting angle of 60° and a rotational speed of 120 rpm. After dielectric planarization, REI etching using CF_4 and CHF_3 in a 1:1 ratio at 20 mTorr and 150 Watts, resulting in SiO_2 etch rate of 225 Å/min, was used to expose the silver. SEM was used to confirm the etch stopping point, as the silver coating could be seen under the SiO_2 layer. Next, using CF_4 and Ar^+ at 9 mTorr and 500 Watts in two different stoichiometry ratios of 4:1.5 and 1:4, the silver top was etched through. The recipes were alternated, starting with the 4:1.5 sccm ratio, for 1-2 min durations for five etches and nine total minutes of etching. SEM was used after each etching step to

determine if further etching was necessary. SEM images of the sample used during the experiment after the different stages are shown in Figure 4-19. The diameter of the cylinders in the images is 48-nm.

The data from this experiment focuses on the 48-nm diameter nanocylinders. After the silver deposition, the PL intensity from the smaller diameter dense arrays was reduced significantly. In addition, the larger diameter cylinders more consistently survived during the silver etching process. The QD cylinder saturation level was measured at each measurement stage by sweeping the laser intensity three orders of magnitude. From the initial oxide stage, the saturation excitation intensity is derived from the integrated intensity to be 2.12 kW/cm^2, which is indicated by the black line in Figure 4-20.

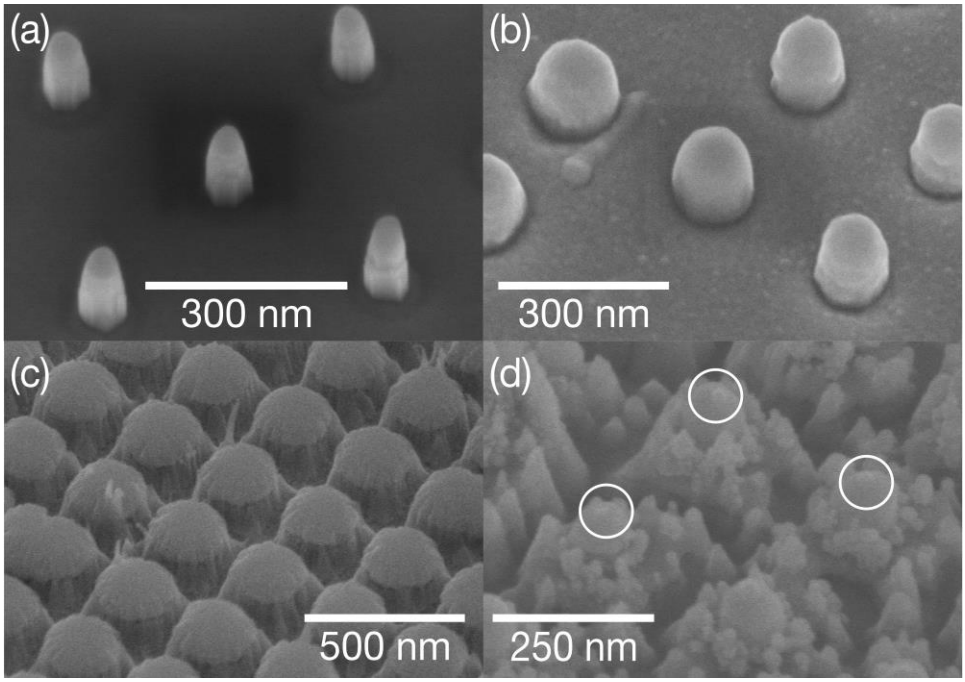

Figure 4-19 The SEM images taken during the open top cavity fabrication process. The

nanocylinders are 135-nm tall and 48-nm in diameter. (a) The nanocylinder dense array after wet etching and Al_2O_3 deposition. (b) Al-doped Ag deposition for 66 seconds. (c) Intermediate image during SiO_2 etch back showing the formation of protective shells around the underlying silver coated cylinders. (d) Cylinders after silver dry etching. The white circles highlight where the cylinder tip has been exposed from top etching. Due to the Ar^+ etching, the SiO_2 is etched simultaneously. The remaining SiO_2 is what covers the substrate surface [78].

The control arrays, which were measured to ensure intensity calibration between the measurement days, are not plotted, as they remained unchanged during the fabrication. From the saturation measurements, the effect of the closed silver film cavity on the dense array enhances the PL intensity collected by a factor of 1.71. When the top Ag film is etched, the intensity enhancement improves by a factor of 1.59 for a total PL intensity change with the open top cavity of 2.72 times.

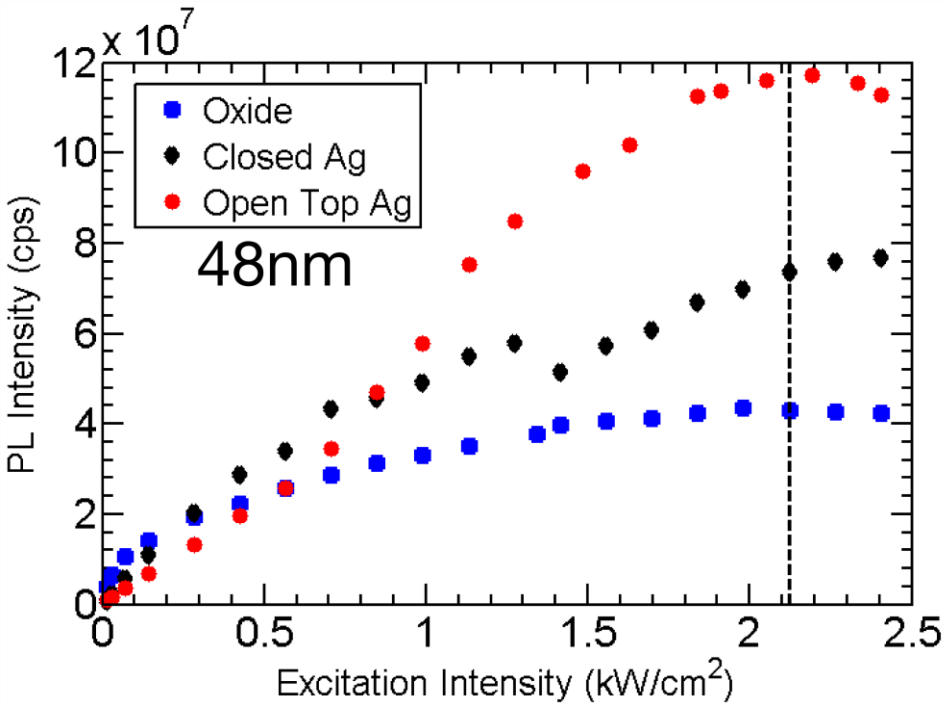

Figure 4-20 Saturation curves for the 48-nm diameter dense array measured at the three stages of measurements: oxide, closed silver, and open top silver. The intensity is enhanced due to the metal film cavity. The dotted black line corresponds to the oxide saturation Intensity of 2.12 kW/cm^2. The consistency of the intensity values was verified between measurement days using a control dense array [78].

Between 1 kW/cm^2 and 1.50 kW/cm^2, the sample experienced an irreversible 'burning effect' in the PL intensity. The effect caused a drop off in the measured intensity, which can be seen clearly in Figure 4-20 for the closed Ag intensity line. The source of this effect is unknown, but it was irreversible, as re-measurement of the lower excitation powers during this stage yielded lower PL intensity. Thus, it is possible that the intensity change is due to laser annealing of the aluminum doped silver film. Due to the burning, which lowered the PL intensity, the PL enhancement measured is a lower bound of the

true enhancement for the oxide to closed Ag stage. This also implies that total intensity enhancement at the open top stage would be higher as well. However, the PL enhancement ratio between the closed Ag stage and the open top stage at saturation is not affected as both measurements were made after the burning occurred for the closed Ag stage.

For the PL Intensity measurements and the TRPL lifetime measurements, the excitation intensity of 2.12 kW/cm^2 was used to make the stage comparisons at saturation. The saturation regime was used again to ensure that the QD cylinders were occupied with carriers and to rule out PL intensity changes from excitation enhancement. The PL intensity measurements of the closed Ag and open top Ag stages were normalized by 35% to account for the increases in the control arrays peak intensity between the oxide and silver measurement days. In Figure 4-21(a), the peak PL intensity of the 48 nm diameter dense array increased by a factor of 1.72 times from 9.75×10^4 counts per second (cps) to 1.71×10^5 cps with the addition of the closed silver film. The peak intensity value was further improved by 37% up to 2.34×10^5 cps with the open top cavity. By removing the top section of the silver film, the metal losses by the silver film were reduced. The emission spectrum broadened, which is due to the stronger enhancement and improved QE of the open top cavity. In addition, there is a blue shift in the peak emission, similarly

to what we noticed our previous experiment [66]. This is 11 nm blue shift is most likely due to further screening of the piezoelectric field by the enhanced excitation field in the cavity structure.

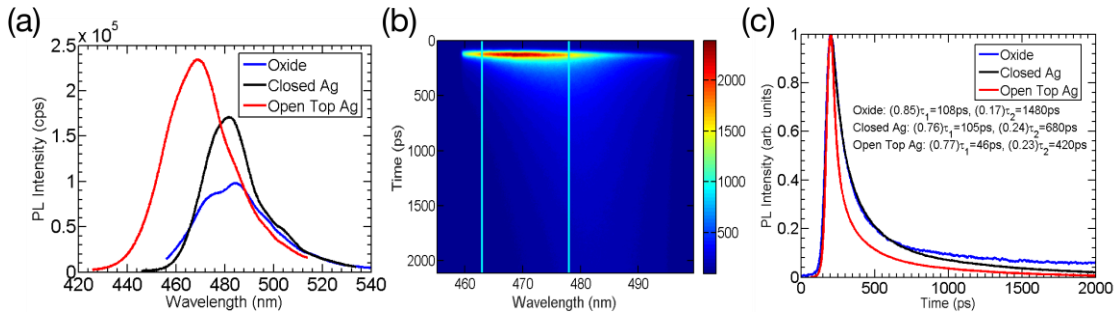

Figure 4-21 PL measurements for the 48-nm diameter dense array. (a) Integrated intensity of the 48 nm diameter dense array at the saturation intensity of 2.12 kW/cm^2 measured at the three stages of the experiment. Closed Ag and Open Top Ag values are normalized by a 35% correction, to account for the variation seen on the control arrays. The open top Ag intensity is the largest and broadest showing the improved QE across the spectrum. (b) The streak camera PL Intensity plotted versus time and wavelength for the Open Top Ag stage at the saturation intensity. The two lines signify the wavelength range used for the lifetime calculation. (c) The time resolved lifetime of the dense array for the three measurement stages, showing the open top has the shortest lifetime. The bi-exponential fitting lifetimes and the weighting of each component in parenthesis are included [78].

Figure 4-21(b) shows the streak camera trace taken for the open top cavity on the 48-nm diameter dense array. The streak camera was used to capture the lifetimes on the picosecond time scale, as the APD resolution is limited to a few hundred picoseconds. The vertical lines on the plot indicate the full width half maximum (FWHM) used for

calculating the lifetime. The lifetime within the FWHM is calculated by summing the counts along the wavelength at each time delay and fitting the resulting trace with a bi-exponential function. The resulting lifetimes for the three fabrication stages are shown in Figure 4-21(c). The initial oxide stage has lifetimes of 108 ps and 1480 ps with weightings of 0.85 and 0.17, respectively. After the closed silver deposition, the lifetimes became 105 ps and 680 ps with weightings of 0.76 and 0.24, respectively. The longer lifetime component was the main component affected here, as the short lifetime remained effectively unchanged in time and weight. At the final stage of fabrication, the lifetime of the dense array becomes shorter, with the open top cavity stage having the shortest lifetimes of τ_1=46 ps and τ_2=420 ps with weights of 0.77 and 0.23, respectively. The weights of the two components at each stage remained constant. Because this is a dense array, it is hard to deduce the source of the two lifetime components as this is an average of thousands of QDs' lifetimes. Comparing the initial (oxide) and final (open top) stages, the short and long lifetime components were reduced by a factor of 2.35 and 3.52, respectively.

With the PL intensity ratios and the TRPL lifetime ratios, the Purcell factor can be calculated. Operating at saturation, the f ratio in equation (2-4) is unity. Since the TRPL lifetimes are much shorter than the laser repetition time of 12.5 ns, the calculated R ratio

is also unity. Neglecting the collection efficiency ratio, F_p can be calculated directly as the product of the PL intensity ratio and the lifetime reduction ratio measured from the experiment. Since the TRPL lifetimes were bi-exponentially fitted, the effective lifetime τ_{eff} was calculated for each stage by the weighted sum of the lifetime components from Figure 4-21(c). The effective lifetimes of the oxide, closed Ag, and open top Ag stages are 343 ps, 243 ps, and 132 ps, respectively. Thus, the experimental Purcell factors for the closed top Ag and open top Ag cavities are 2.43 and 6.24. The lifetime reduction and PL intensity enhancement, while pumping above saturation, indicate improvement in the QE of the QDs inside the open top cavity.

4.5.3 Experimental Discrepancies in the Purcell factor

Several factors contribute to the small magnitude of the Purcell factors for the experimental open top cavity. First, the measured nanocylinders were larger in diameter. This directly affects the expected QE and F_p for the closed Ag stage and the open top Ag cavity. The expected Purcell factor is an order of magnitude smaller with the larger 48-nm diameter compared to the 25-nm diameter in Figure 4-17.

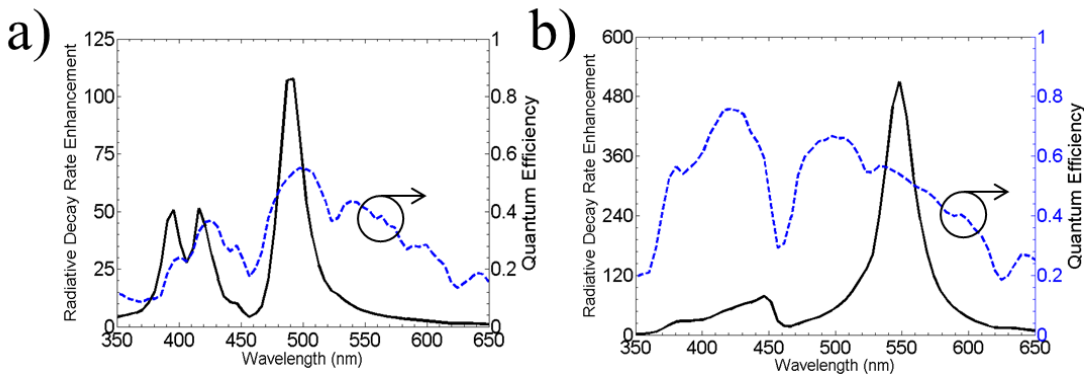

Figure 4-22 Simulated radiative decay rate enhancement or Purcell factor and cavity AQE for the (a) closed top Ag cavity formed from silver sputtering on the nanocylinder and (b) the open top cylinder cavity. This cavity consisting of 2-nm thick Al_2O_3 spacer and 30-nm thick silver cavity on a 48-nm diameter QD. The magnitude of the Purcell factor is an order of magnitude smaller than the expected F_p for a 25-nm diameter nanocylinder in Figure 4-17.

In addition, the simulations use Johnson and Christy silver [64]. While the Al-doped silver improved the film sidewall coverage and reduced the grain size compared to the pure film, the doped film has greater losses than the pure silver [84, 85]. In the emission window of our sample, the imaginary component of the dielectric constant for the dope silver is three times as large as the empirical Johnson and Christy data values for silver [64, 85]. Moreover, there is a red shift in the LSPR wavelength of the structure due to the red-shifted real part of the permittivity for the Al-doped Ag. The wavelength mismatch due to this contributes to the reduced enhancement. Lastly, there could be some light scattering off the remaining SiO_2 nanostructures on the sample surface. This could refract

the PL emission outside of the collection cone for our setup, resulting in a lower measured PL intensity enhancement ratio and subsequently a lower Purcell factor since the experimental F_p is calculated using that ratio. All of these factors play a role in reducing the experimental F_p calculated for this experiment. Future adjustments for many of these variables should improve the measured results.

4.6 Summary

The open top cavity design lays the framework for QD homogenization. By taking advantage of the zero-mode cavity generated from removing the top silver surface [81], large Purcell factors (>1000x) can be generated for relatively large diameter QD nanocylinders (~25-nm) with good cavity AQE (>0.50). For QDs formed with poor QE, this method will alleviate that issue with conventional post processing, creating a uniform array of QD emitters, assuming similar emission wavelengths dot to dot. Simultaneously, the magnitude of the Purcell factor is large enough that the reduced QD lifetime could be on the order of the dephasing time of the emission, pushing the envelope for indistinguishable SPSs by solving the 'photon gun' issue [56]. Fabrication of a uniform array of indistinguishable QDs with electrical injection compatibility is a critical step for SPS integration into devices. Hence, we demonstrated the fabrication procedure for the

open top cavity on a dense array of nanocylinders, showing that it is possible to create an open top cavity using conventional film deposition and etching techniques. While the experimental demonstration of this cavity structure has plenty of room for improvement due to the current fabrication limitations in conformal silver deposition, the emerging study of silver ALD may soon solve this issue [88]. Thus, realization of a pure silver open top cavity will be achievable with the development of the silver deposition technology.

Chapter 5

Parabolic Nano-Lenses for Enhanced Light Extraction from Quantum Dot and LED Nano Structures

5.1 Introduction

Controlling the extraction and directionality of the emission from nanoscale light sources is important in the engineering of LEDs and SPSs. With the introduction of the semiconductor LED, light generation efficiency has improved significantly across the visible spectrum, making LEDs an alternative lighting device to replace existing lighting infrastructure [89]. However, light extraction from semiconductor LEDs is limited by the high index contrast between the air and the semiconductor. Several approaches have been explored to improve the photon extraction efficiency from LEDs, including surface roughening [90], anti-reflection coatings [53], cavity layers [91], and using nanopillar [92] or nanowire [93, 94] LED structures. Surface roughening applies texture to the planar exit surface, increasing the photon acceptance angle at the expense of a random exit distribution. Anti-reflection coatings use a graded index to lower the index contrast at the

air interface, but cannot overcome large angle light rays. External cavities can re-direct emission towards a collection direction, but increase fabrication complexity and can introduce new loss mechanisms into the system. Using nanopillar LEDs, the light extraction efficiency is improved over the planar LED counterparts, as the structure size is typically on the order of the emission wavelength and there is less light trapping by total internal reflection [23, 72, 95].

Control over the emission direction can be achieved with reflectors and/or lenses to guide the light towards the collection direction. However, this does not consider the angular spread or distribution of the emission. For applications that require control over the emission angle for coupling such as waveguides or fibers, directional lighting, or quantum mechanical applications, the angle of the emission is critical to device operation. Modification of the angular spread can be achieved by changing the emitter geometry such as tapering a nanowire or by integrating optics into the system. Due to the diameter-dependent emission wavelength with the top-down fabricated InGaN/GaN nanopillars, the latter is the preferred method to preserve the emission wavelength. This has been demonstrated before by integrating parabolic nano lenses in either reflection [52, 53, 96] or transmission [50, 51] mode to concentrate emission, reducing the angular emission spread. With reduced angular spread and improved emission extraction, the

external QE of these devices will be improved, leading to sources that are more efficient, have reduced energy consumption, and increased brightness output at a given input power level. In this chapter, two lens designs will be presented: a reflection based parabolic lens for a SPS and a transmission based parabolic lens for multi-color LED emission collimation.

5.1.1 Figure of Merit

In order to characterize and compare the effect of the lenses on the light extraction and the emission angular spread, we need to define a figure of merit (FOM). The FOM is the fraction of the total light emission from all directions that travels in the direction of interest within the angular range of interest. This measures the light collected by the collection optics. It comprises of two terms: the light extraction efficiency (LEE) and the photon collection efficiency (PCE). It is calculated for each wavelength.

$$FOM = LEE \times PCE \qquad (5\text{-}1)$$

The LEE is the fraction of the total emission that is travelling in a designated direction. Assuming a cube around a 3-D structure, this is the emission into one of the six faces of the cube. If there are no losses in the system, the sum of the emission into each side should be unity. An example of the LEE calculation is shown in Figure 5-1. The structure

is a 40-nm diameter nanocylinder with the InGaN QD located 10-nm below the surface. The pillar structure is 135-nm tall.

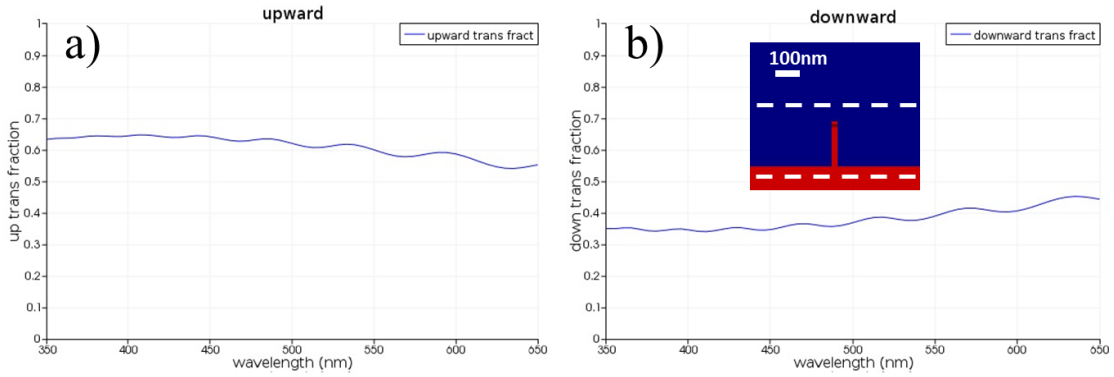

Figure 5-1 Simulated transmission fractions or LEEs for the air direction and substrate direction. The inset shows the structure that is a 40-nm diameter nanocylinder with the QD located 10-nm below the surface. (a) The LEE for the air direction showing ~65% of the total emission is transmitted towards the air. (b) The LEE for the substrate direction. Only ~35% of the emission travels into the substrate.

Using transmission fraction calculations, the percentage of the emission transmitted in the air direction and substrate directions for the nanocylinder emitter per wavelength is calculated to be about 65% upward and about 35% into the substrate.

The PCE is the fraction of the emission through one of the cube faces that is within a designated angular emission cone in the far field. Using a transmission monitors above the structure, the far field projection into air of the emission can be calculated per each wavelength.

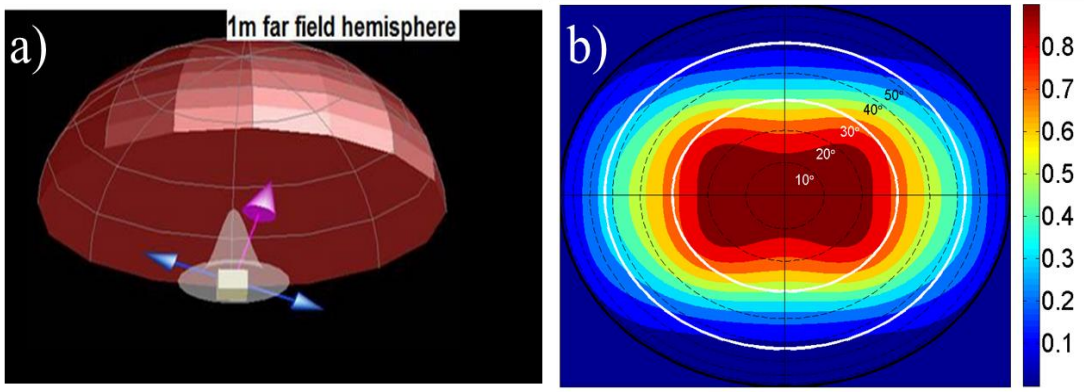

Figure 5-2 (a) Far field projection schematic [69]. The planar monitor is used to project the near field emission onto the far field hemisphere 1-m away from the structure. (b) The far field distribution for the structure in Figure 5-1 at the emission wavelength of 411-nm. The white circles correspond to a 0.5 NA (30°) and a 0.8 NA (53.1°). For the total emission travelling upward, 40% is concentrated within the 30° cone and 80% is within the 53.1° cone.

Figure 5-2 shows a far field projection example for the emission wavelength of 411-nm. Within a numerical aperture of 0.5, which corresponds to a collection half cone angle of 30°, is 40% of the far field emission. Thus, at the wavelength 411-nm the FOM for the example structure using a 0.5NA is 0.26. So, 26% of the total emission from the example at 411-nm is collected with a 0.5NA lens. For our typically explored geometries, such as the tapered nanopillar or nanocylinder, the FOM is even lower, at about 13%. In order to maximize the FOM for 0.5NA, the emission needs to be concentrated into a smaller collection angle, and the emission travelling towards the substrate needs to be redirected

towards the collection direction. This is done with a reflector structure and a collimating nano lens.

5.2 Integrated Parabolic Nano Lens Reflector

For a SPS, lost photons from absorption or emission away from the collection direction are detrimental to device operation. For the InGaN/GaN nanopillar SPS, about 13% of the sample emission is collected, following the calculation in section 5.1.1. This means that the reliability of collecting an emitted single from the device is only 13%, assuming no other loss channels. Subsequently, this would increase the number of bits required to send information by a factor of eight, to ensure that the detector records each bit. In order to improve photon extraction, a parabolic reflector and an out coupler nano lens are integrated around the nanopillar geometry. With the appropriate lens parameters, the FOM for 411-nm wavelength is increased to 68.5%, due to improvements in the LEE and the PCE.

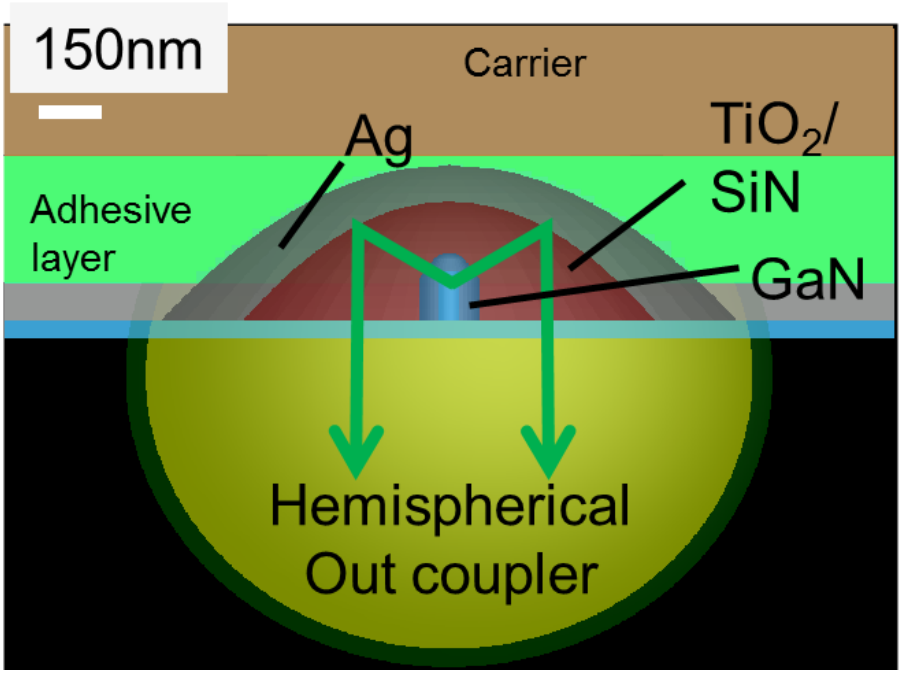

Figure 5-3 Schematic of the parabolic reflector and hemispherical out coupler lens surrounding the InGaN/GaN nanopillar. Emission toward carrier is reflected back collimated towards the out coupler. The QD is located at the focal point of the parabolic reflector.

When designing the lensing system, the parabolic reflector and the out coupler are optimized to the emission wavelength of 411-nm. The wavelength was chosen because the samples from Chapter 2 emit around that wavelength and exhibit strong photon antibunching, making them a good SPS candidate. At this wavelength, silver is a better reflector than gold [64], so silver is used as the reflector material. Figure 5-3 shows a schematic of the integrated lens design. The final device uses substrate directed emission that is coupled out with a hemispherical lens. In order to integrate the lenses to with the SPS, the lenses should be index matched to the GaN nanopillar material to reduce

internal reflections. Titanium dioxide (TiO_2) is a good candidate because it is a high index dielectric that can be e-beam evaporated in the LNF cleanroom facility. With the emission wavelength and lens index chosen, the dimensions of the parabolic reflector were determined. The parabolic equation is

$$4 * f * y = x^2 \qquad (5\text{-}2)$$

where f is the focal length, y is the height, and x is the radius. For a parabolic shape, rays originating from the focal point will be collimated upon reflection off the parabola. Therefore, light that originates from the focal point when reflected off the parabola will be collimated. Hence, the parabolic lens reflector must have the QD emitter located at the focus point. To reduce plasmonic interactions between the QD and the reflector, which can cause additional photon loss channels, the reflector must be sufficiently far enough away from the emitter. As for the out coupling lens, a hemisphere was chosen to emulate the performance of a solid immersion lens (SIL) [97, 98]. From ray optics, the optical rays originating from a source located on the flat surface of the hemispherical SIL (hSIL) will always be perpendicular to the curved face of the lens, as shown in Figure 5-4(a). This greatly reduces the chance for internal reflection, as the rays should be within the critical angle to exit the system. For rays that are generated further away from the lens surface as shown in Figure 5-4(b), Snell's law shows that the rays will be bent up toward

the desired collection direction as they bend away from the normal.

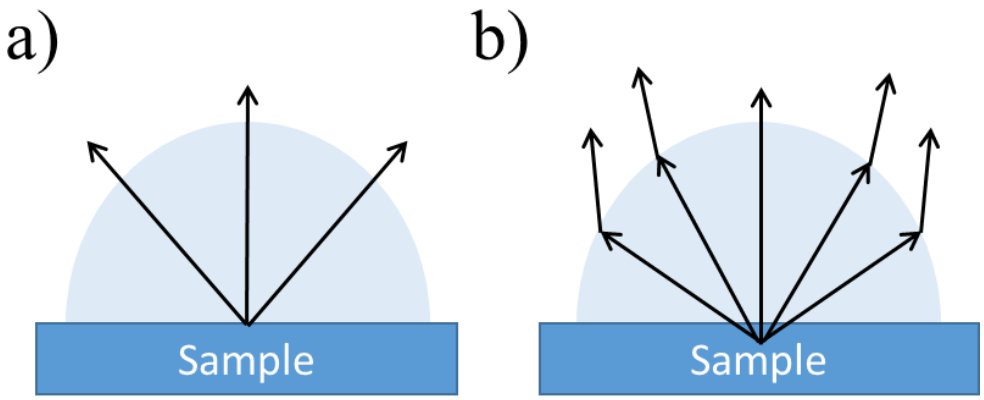

Figure 5-4 (a) Hemispherical Solid Immersion Lens with the source located at the lens interface. Rays are perpendicular to the lens exiting the system. (b) Hemispherical Solid Immersion Lens with the source located below the lens interface. Optical rays are no longer perpendicular to the lens and refract towards the collection plane.

Due to the nanopillar height, the QD source is located below the hSIL interface, so the rays should be bent towards the center axis. Therefore, the combination of the parabolic reflector and hSIL should maximize single photon out coupling and collimation.

5.2.1 Parabolic Reflector Design

The design of the reflector required an appropriate lens diameter, focal length, and height such that the metal losses from the reflector and the plasmonic interaction between the silver reflector and QD were both minimized. In order to ensure that the curved silver

structure would be a good reflector and not transmit radiation through it, the minimum silver thickness was determined to be 120-nm thick. Films thinner than 120-nm allowed more than 1% of the light to transmit through the film. To determine the parabola's distance to the QD dipole, the thickness of the parabolic dielectric was varied from 100-nm to 200-nm. A radially oscillating dipole was used in the simulation [66]. For thinner dielectric layers, the metallic losses started to affect the system. From the initial testing, the dipole needs to be at least 200-nm away from the silver layer to ensure over 98% transmission.

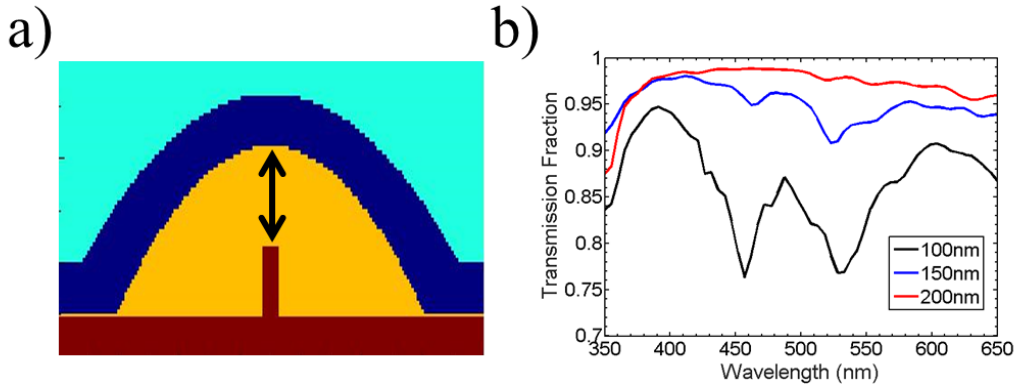

Figure 5-5 (a) Parabolic reflector testing schematic. The black arrow indicates the dielectric thickness that is varied. (b) The transmission fraction of the emission into the substrate versus the oxide thickness indicated by the black arrow in (a). When the reflector is closer to the QD cylinder, there are more losses and less emission transmission is recorded in the substrate.

For the final design, the distance from the top of the metal parabola to the QD dipole

was 310-nm, which is also the focal length of the parabola. The base of the parabola is 1020-nm wide and the height is 210-nm. The metal parabola base is 100-nm above the dipole location. The QD dipole is located 30-nm below the top planar surface. The schematics for testing the reflector with and without the hSIL concentrator are shown in Figure 5-6. The hSIL radius is 500-nm. The LEE and PCE were simulated and the resulting FOM was calculated for both structures to compare the effect of adding the hSIL. Because the system is index matched, the index of refraction schematic appears as a planar layer. The yellow star represents the approximate location of the QD dipole used in the simulations.

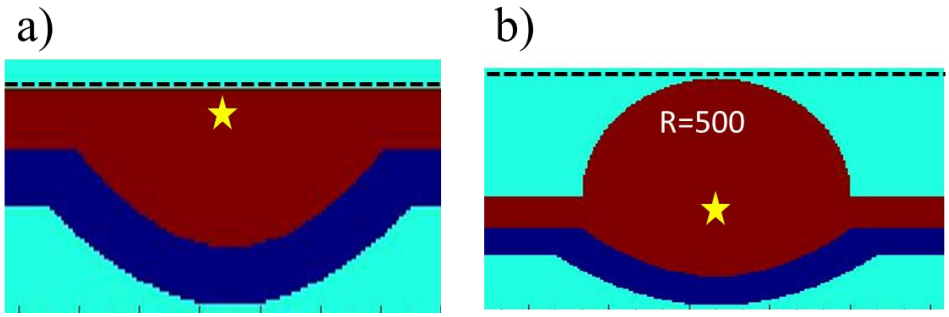

Figure 5-6 Simulation cross sections for testing the LEE and PCE for the parabolic reflector and hSIL. The yellow star indicates the QD dipole location and the dotted black line indicates the monitor location. (a) Parabolic reflector testing schematic. The focal length is 310-nm. (b) The parabolic reflector with the hSIL collimator lens. The radius of the hemisphere is 500-nm.

The resulting LEE versus wavelength plot for the two structures is shown in Figure

5-7. The planar substrate with the parabolic reflector has over 70% of the light transmission into the air across most of the visible spectrum. Since the QD dipole is located relatively close to the air-GaN interface, there is minimal light trapping of the emission in the substrate into the in-plane directions. After adding the hSIL, the LEE increases by ~10% in a narrow bandwidth around the emission wavelength of 411-nm from 78% to 87%.

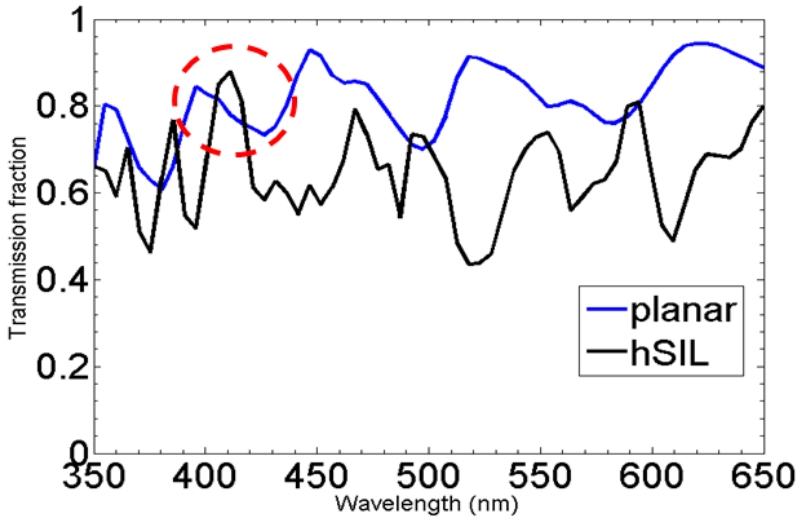

Figure 5-7 Simulated LEE for the parabolic reflector (blue) and hSIL with the parabolic reflector (black). At the emission wavelength of 411-nm, 78% of the emission is directed towards the air. This increases to 87% with the addition of the hSIL lens. The red circle indicates this region.

In addition to improving the LEE, the hSIL increased the PCE by 7% from 71% to 78% with the hSIL. Initially, the far field distribution is along the axis of the E-field oscillation

for the dipole emitter. After the hSIL, the far field distribution is distributed more evenly azimuthally. Though the far field distribution for the hSIL is broader within the 30° cone, there is less emission outside of the 30° cone, since the PCE is larger. With the improvement in the LEE and PCE, the product, the FOM, is improved by 12.5% from 0.56 to 0.685. This means the ~70% of all photons emitted from the QD in this configuration are within a 30° cone above the structure.

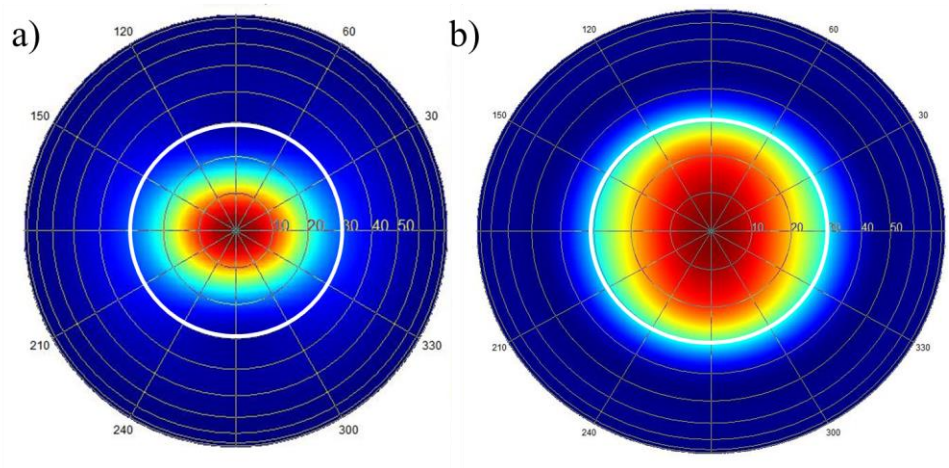

Figure 5-8 Far field distributions at a wavelength of 411-nm. (a) Parabolic reflector with the planar GaN interface. The PCE is 71%. (b) The parabolic reflector with the hSIL collimator lens. The PCE is 78% and the far field is re-shaped.

Compared to 13% for the bare nanocylinder structure, the integrated lens structure gives a 5.2 times improvement in FOM. This alone would reduce the required bits necessary to transmit by a factor of four, quadrupling the data rate. Since the LEE for this integrated

structure is almost 90%, there is a little room for improvement with an anti-reflective coating. More focus would be needed on optimizing the hSIL structure in order to raise the PCE, however. Fabrication of this double-sided lens device is detailed in part, in the future work section.

5.3 Parabolic Lenses for Enhanced LED Emission Extraction

For the conventional LED structure, one of the biggest issues is light extraction. The high index of the refraction in a planar film LED limits the light extraction due to total internal reflection. To help alleviate this issue, micro- and nano- pillar LEDs have been explored due to their increased light extraction [25, 72, 95].

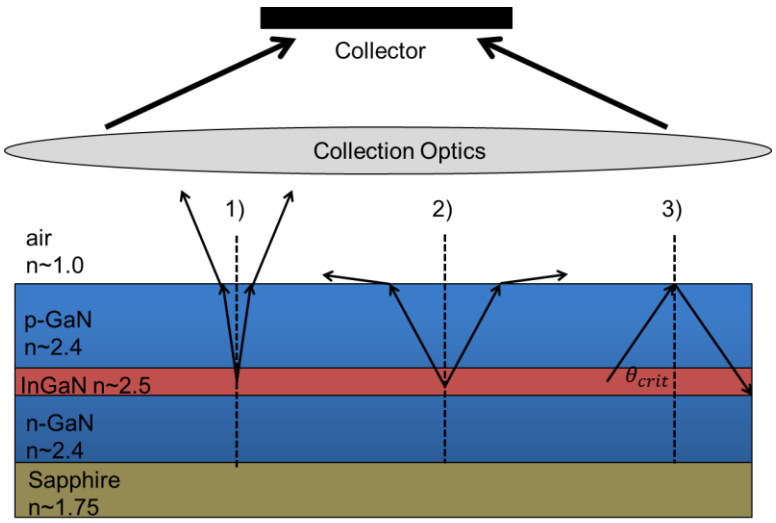

Figure 5-9 Schematic of a typical single quantum well InGaN/GaN LED structure. Due to the high index of refraction, light rays from case #2 and case #3 do not make it to the collector.

However, even with improved light extraction, the micropillar LED still has room for improvement in the LEE and the PCE. Figure 5-10(a) shows the schematic of our nanopillar LED. At this diameter of 40-nm, the emission wavelength is 492-nm, and the LEE for the nanopillar into the air is only about 30%.

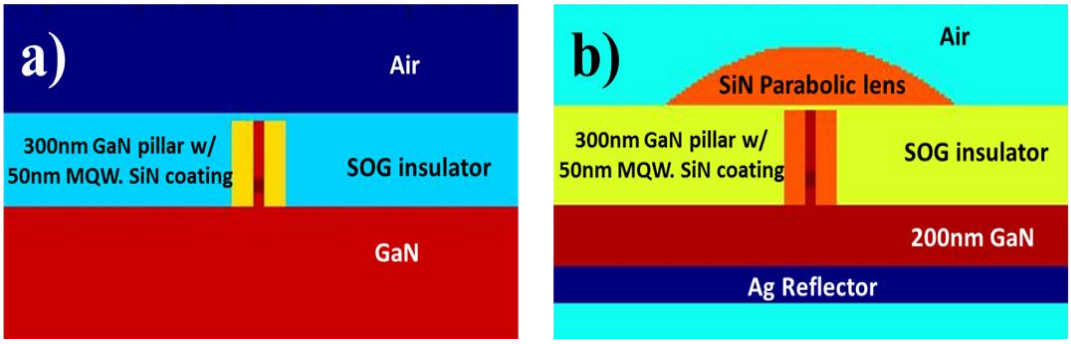

Figure 5-10 Cross section schematics of a nanopillar LED structures. (a) Nanopillar in isolating SiN and spin on glass layers [95]. (b) Same LED structure with an Ag reflector located 200-nm below the nanopillar and a parabolic lens on top of the LED. The parabolic lens has a height of 200-nm and a base diameter of 500-nm.

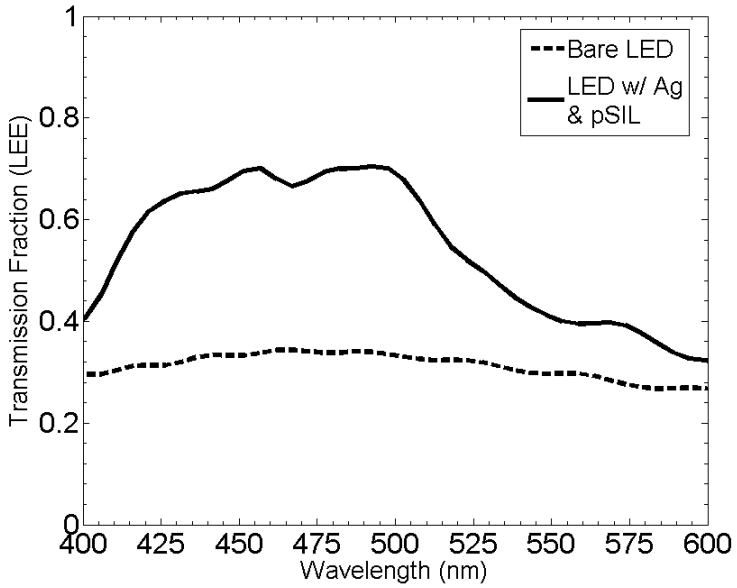

Figure 5-11 The Light Extraction Efficiency for the two LED structures in Figure 5-10. With the Ag reflector and the parabolic out coupler lens, the LEE is doubled at the emission wavelength of 492-nm.

The low LEE is due to light loss into the substrate and radial directions. With a metal reflector, most of this emission can be redirected upwards towards the air. Moreover, with the addition of the parabolic lens, the emission can be highly concentrated. Figure 5-10(b) shows the schematic for the LED structure with the Ag reflector and parabolic lens. The colors in the image are just to distinguish different materials. The silver reflector is located 200-nm below the substrate surface, which minimizes the plasmonic losses without allowing too much room for light to be reflected outside of the lens diameter. The parabolic lens parameters were optimized at an emission wavelength of 492-nm to

maximize the amount of emission within a 30° half-angle cone, corresponding to a 0.5NA lens. The resulting parabola dimensions are a height of 200-nm and a base diameter of 1-μm, which corresponds to a focal length of 313-nm.

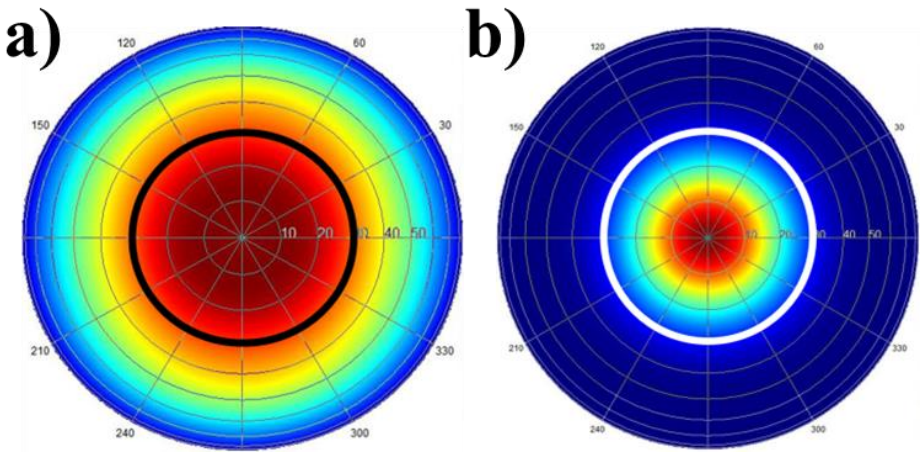

Figure 5-12 Far field emission patterns at 492-nm. The circle indicates 0.5NA. (a) Nanopillar in isolating SiN and spin on glass layers. The PCE for 0.5NA is only 30%. (b) Nanopillar structure with an Ag reflector and parabolic lens. The PCE for 0.5NA is 87%. The parabolic lens has a height of 200-nm and a base diameter of 1-μm.

With the reflector and the lens, the LEE was doubled to 70%. Simultaneously, the PCE was improved greatly from 30% to 87%, as the lens highly concentrated this wavelength. The FOM improvement is approximately six fold, from 10.3% to 61.3% of the total emission within the collection aperture of 0.5NA. Optically pumping the two LED structures would show a six times increase in the blue LED's PL emission.

Integrating the lens and reflector results in significant improvement of the photon extraction of a nanopillar LED, improving the compatibility with conventional optics and expanding the toolbox necessary for microdisplays.

5.3.1 Parabolic Lens Fabrication using Resist Reflow

The parabolic collimator lens for the nanopillar LED structure is fabricated using a resist reflow procedure. While other methods of fabricating spherical or parabolic shapes have been investigated, such as spinning polystyrene beads as a curved masking layer for etching [99], they lack position control due to the spin distribution process. Using photoresist and lithography allows for precise position and dimension control of the resist shape. The process of changing the photoresist shape during lithography has been explored greatly using optical lithography and e-beam lithography photoresists [52, 98, 100, 101]. Photoresists have a curing temperature used after lithography exposure such that the resist is hardened for future processing. By exceeding that curing temperature and raising the temperature towards the glass transition temperature (T_g), the resist enters into a softer state. When the surface tension of the resist is broken in this soft state, the top surface of the resist flows down the sidewall, rounding the resist shape. With sufficient baking time, all of the photoresist corners round. A parabolic shape can be achieved in the

photoresist layer, which subsequently acts as a parabolic etching mask, by adjusting the baking temperature and duration. The parabolic shape is then transferred into the underlying dielectric layer during dry etching with the correct etching chemistry.

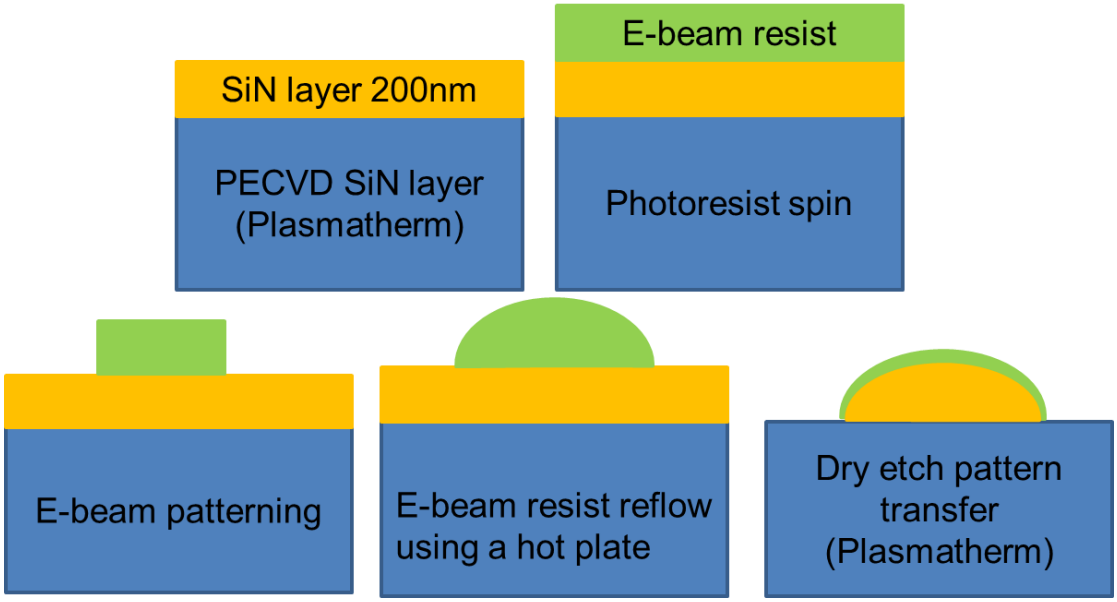

Figure 5-13 Fabrication details for the Silicon Nitride parabolic lens. Using e-beam and PMMA reflow, the PMMA acts as a parabolic etching mask for the underlying SiN. After dry etching, the SiN has a parabolic shape.

The fabrication schematic for the parabolic lens fabrication is shown in Figure 5-13. For the fabrication test, a piece of silicon substrate was used in place of the LED array. To transfer this process to the LED array, the silicon nitride (SiN) layer would need to be planarized before lithography to ensure a flat surface. Initially, a 200-nm thick SiN layer was deposited using the Plasmatherm. The index of refraction and film thickness for the

SiN film were confirmed, using the Wollam ellipsometer, to be 2.0 and 200-nm respectively. These values were used in the simulations previously described.

After dielectric deposition, PMMA 950k A4 was spun at 4000 rpms for 45 seconds to create a 200-nm thick resist layer. The PMMA was patterned with e-beam lithography on the JEOL JBX-6300FS tool using the LED nanopillar spacing.[9] The PMMA cylinders were 1-μm in diameter with 1.5-μm pitch. For the 1-μm diameter nanopillars, this corresponds to one lens per pillar. For the smaller nanopillars (40-nm-200-nm) with smaller pitch (300-nm), several pillars share a single lens structure. The resist was developed for 4 minutes using the standard development process to ensure residual PMMA was removed from in between adjacent structures. Under SEM inspection, the PMMA cylinders were 1-μm in diameter with a 1.6-μm pitch.

With the resist in place, the PMMA was reflowed. The T_g for PMMA is between 85°C to 165°C depending on the concentration and composition. The appropriate reflow temperature for our PMMA was determined to be 140°C. The reflow recipe used was a two-step process. The sample was heated to 115°C for 5 minutes on a hotplate; then, it was transferred to a 140°C hotplate for 15 minutes. The before and after reflow SEMs are shown in Figure 5-14. An important note here is that patterns exposed to the SEM did not

[9] E-beam operation performed by Jingyang Sui.

reflow the same as unexposed patterns, as the e-beam energy of the SEM changes the characteristics of the PMMA similarly to e-beam lithography. Therefore, the SEM exposure was limited to small corners of the lens array to confirm parabolic formation.

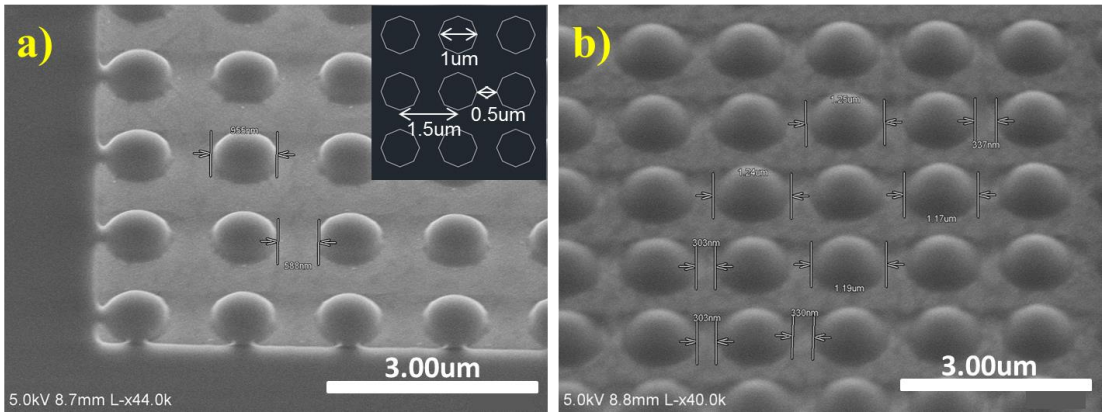

Figure 5-14 SEM images of the PMMA array. (a) Resist cylinders with 1um diameter and 1.6um pitch in an ordered array. (b) Resist parabolas after reflow heat process with a diameter of 1.2um. The resist is baked at 140°C on a hotplate for 15 minutes. The diameter increases as the resist reflows.

The diameter of the cylinders increased from 1-µm to 1.2-µm during the 20 minute baking process, which was indication that the reflow was working. The SEM image in Figure 5-14(b) was taken on an array previously unexposed to SEM energy. To characterize the resulting resist shape, atomic force microscopy (AFM) was performed using the ICON AFM in the tapping mode. From the AFM scan across a 7-µm-by-7-µm area, the PMMA reshaping was confirmed. The height of the final parabola at its center

was still 200-nm.

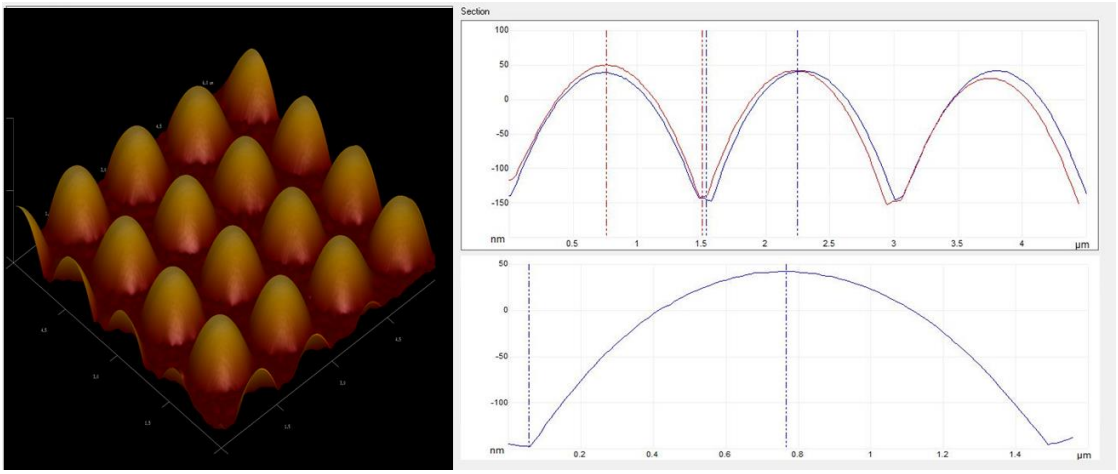

Figure 5-15 AFM scan of a 7-µm-by-7-µm section of PMMA parabolic structures. Scan shows a height of 200-nm, with a base diameter of ~1.4-µm. The bottom right scan is a zoom scan of the center parabola.

The AFM scan revealed that the diameter was in fact 1.4-um across the base instead of 1.2-um. Using a parabolic fitting, the focal length of the PMMA parabola was 682-nm, which is significantly larger than the desired focal length of 313-nm. However, it is important for the PMMA to be larger than the design parabola, because the dry etching induces some lateral shrinking of the parabola since the plasma etching is isotropic, resulting in a smaller parabola diameter through pattern transfer.

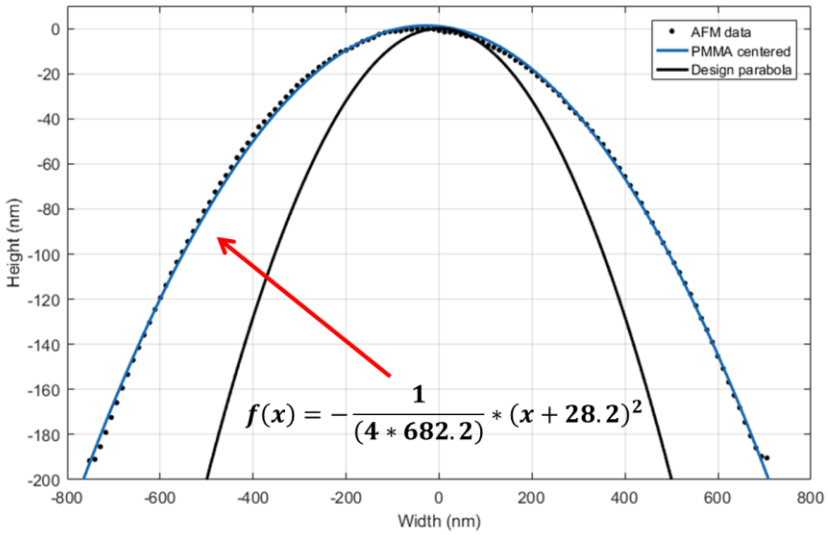

Figure 5-16 Parabolic fitting of the zoomed AFM scan on the PMMA parabolic shape. The resulting parabola has a focal length of 682-nm. The design parabola with a focal length of 313-nm is also plotted for reference.

Dry etching of the parabolic resist shape into the underlying SiN requires a 1:1 etching ratio for the PMMA and SiN. Using an established SiN etching recipe on the Plasmatherm REI etching tool, O_2 gas was added to the recipe until the PMMA etch rate was the same as the SiN etch rate. The final etching rate for both materials was between 140-nm to 160-nm per minute. The etching was done at 200 mTorr with 250 Watts of RF power. The etching chemistry was $O_2/CHF_3/CF_4/Ar^+/SF_6$ at 4.8/20/33/65/7 sccm flow rates. Due to etching rate drifts with chamber temperature, the recipe was used in 30-second intervals. The pattern transfer procedure is as follows. First, heat the empty chamber with an oxide etch recipe. Next, etch the sample for 30 seconds with a 5-minute

cool down after the SiN etch. Then, dummy templates of SiN and PMMA were checked for etching rate confirmation, and the SiN etch was repeated. The SiN etch was run three times for a total of 1.5 minutes of etching. After pattern transfer etching, the sample was run through a resist descum process in O_2 plasma for 1 minute to remove any residual PMMA from the surface. The SEM image of the SiN lenses in Figure 5-17(a) shows the reduced bottom diameter of 1.2-um, which was confirmed by AFM. From the parabolic fitting in Figure 5-17(b), the SiN lens has a focal length of 465-nm. Lateral etching of the SiN and PMMA reduces the diameter of the SiN lens. Reducing the reflow baking time, such that the initial PMMA diameter is decreased should help to shrink the SiN lens focal length and diameter to the design parabola's parameters.

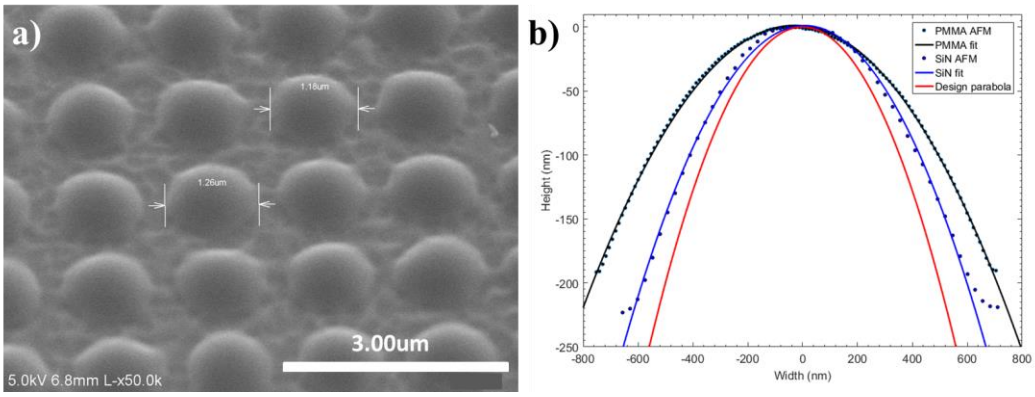

Figure 5-17 SEM image and AFM trace of the SiN nanolens array. (a) SEM image of an array of SiN nanolenses. After dry etching, the base diameter is 1.2um. (b) Parabolic fitting of the AFM scan across a single SiN lens (blue). The focal length is 465-nm and the height is 200-nm. The PMMA parabola (black) and the design parabola (red) are shown for comparison.

This section details the fabrication procedure for creating SiN parabolic out coupling lenses. Completing the reflector and lens structure integration requires laser removal of the sapphire substrate. With the sapphire removed, the GaN can be dry etched to a 200-nm thickness, and the silver reflector can be deposited on the GaN. The sample would have to be transferred to a carrier to complete the reflector deposition, as it would be too thin to handle otherwise. This reflector deposition procedure is a work in progress and is a subject for future work. Otherwise, we have successfully demonstrated the fabrication of parabolic SiN lenses using photoresist reflow and dry etching.

5.3.2 Collimator Lens for Electrically Injected Multi-Color LED Pixel

The integration of an array of full-spectrum light emitters on a compact chip-scale device is desirable for many applications, such as micro-displays, visible light communication, and biosensors. With the diameter dependent strain relationship in the InGaN/GaN thin film QWs, multiple emission colors with good color control can be achieved using different diameter nanopillars [25, 95]. The simultaneous blue, green, and red color emissions from a single standard InGaN QW and InGaN MQWs have been demonstrated with a wavelength tuning range exceeding 180-nm, using this local strain

engineering approach [25, 95]. Figure 5-18(a) shows the electroluminescence (EL) spectra from three pixels, each containing an array of a particular diameter nanopillar within the multi-color LED device.[10] For blue and green, color pixels are made up of an array of pillars in 1-μm-by-1μm area, whereas for red, a single 1um pillar is used. A major benefit of this approach is that the fabrication procedure is identical across the nanopillar diameters for the nanopillar LED, allowing them to be manufactured simultaneously on a single chip, reducing the cost and complexity of the device. Nevertheless, similarly to conventional planar LED devices, the nanopillar LED suffers from a spread emission pattern. Integrating a condenser lens array with the multi-color LED pixels to reduce the far field emission pattern spread furthers the possibility of realizing an ultracompact multi-color light source.

[10] LED fabrication and measurements performed by Dr. Kunook Chung.

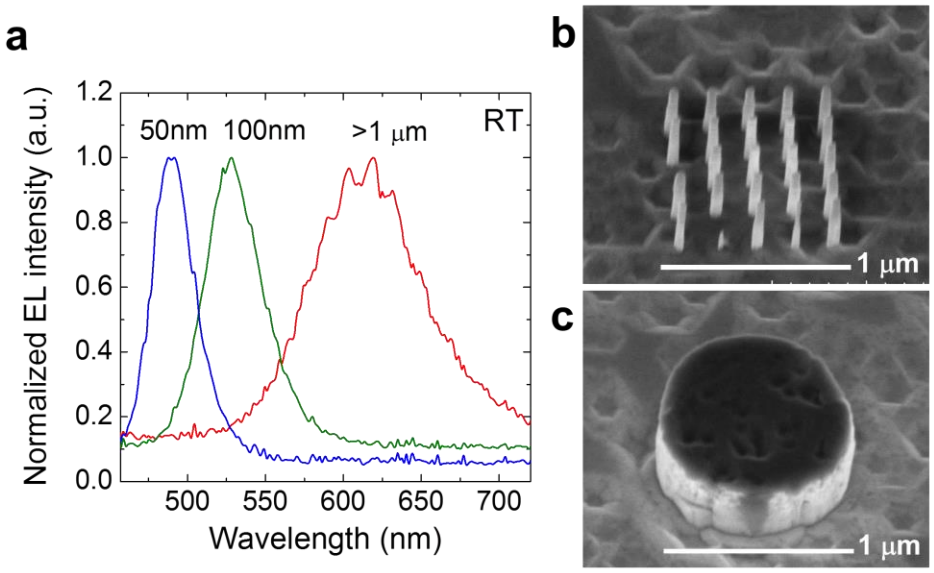

Figure 5-18 (a) Room temperature EL spectra of nanopillar LEDs with various diameters. Micron-size LED pixels possessing (b) an array of 50-nm nanopillars (upper image) and (c) a single 1-μm nanopillar (bottom image).

Following a similar approach to section 5.3, a parabolic lens was designed and simulated for the multi-color LED device. The lens needs to condense the far field emission across the spectra in Figure 5-18. The multi-color LED posed new challenges in the lens design, given the device geometry and emission wavelength bandwidth. The first challenge is that the addition of the gold electrical top contacts for the LED, affect the far field emission pattern. The lens dimensions used for the blue emission in Figure 5-10(b) did not work well to focus the light with the contact layer in place. The second challenge is that the substrate cannot be thinned to 200-nm reliably for the electrically injected LED structure. This results in the reflector placement being much further away from the

emission source, which can reduce the amount of backwards emission redirected towards the lens. In this case, the Ag reflector was placed after 1-μm of GaN substrate. Lastly, the lenses must accommodate larger pillar sizes and longer emission wavelengths. This issue was resolved by using different lens sizes for the different emission wavelengths and extending the lens height. As the wavelength increases, the lens size must increase to ensure it can bend the light. Like the nanopillar fabrication process, different diameter SiN lenses can be fabricated simultaneously, as the procedure is identical across lens diameters. Thus, multiple sizes were considered to ensure each color was optimized within the 0.5NA zone.

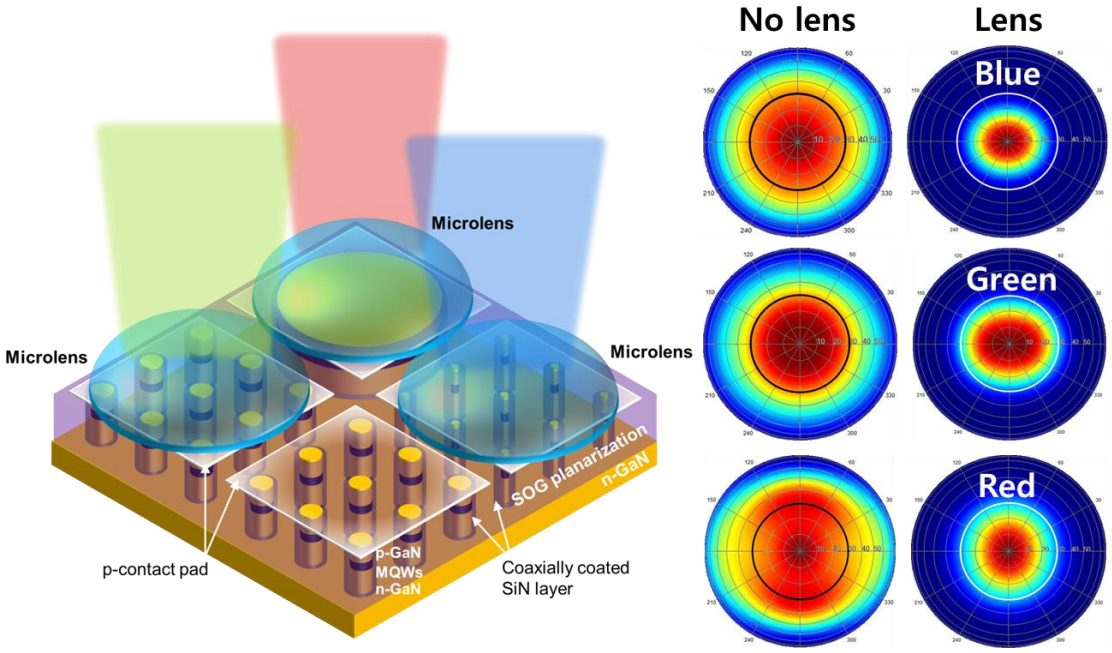

Figure 5-19 Schematic of the nanopillar LED structure with the parabolic condenser lenses and a backside reflector. A comparison of the far field angular distribution of the

emission patterns for the three colors with and without the parabolic lens structures. The circles indicate the 0.5NA area of the far field patterns. Without a condenser lens, the percentages of the emission within the 0.5NA zone are 31%, 36%, and 27% for blue green, and red, respectively. The lenses condense the emission pattern significantly, to 95%, 83%, and 75% within the 0.5NA zone for blue, green, and red, respectively

The condenser lenses were designed around maximizing the PCE within the 0.5NA zone for the central emission wavelength of each color. The blue wavelength pillars have a diameter of ~40-nm and center wavelength of 495-nm, the green wavelength pillars have a diameter of ~100-nm and center emission wavelength of 540-nm, and the red wavelength pillars are ~≥1-μm in diameter with a central wavelength of 625-nm. The schematic of the color pixel arrays is shown in Figure 5-19. Without the lens and the back reflector, the far field emission patterns are very broad, with 31%, 36%, and 27% of the total emission for the blue, green, and red, respectively within the 0.5NA zone. The lenses used for the blue pixel have a base diameter of 1-μm and a height of 500-nm. The green and red pixels share the same lens size, which is a base diameter of 1.2-μm and a height of 500-nm. Lenses with diameters larger than 1.2-um did not improve the PCE within 0.5NA of the red pixel. Since the red wavelength nanopillar's diameter is larger than the emission wavelength, there is wave guiding within the nanopillar. Therefore, the lens diameter only needs to be larger than the nanopillar diameter when wave guiding occurs.

With the lenses and the Ag back reflector, the PCE for 0.5NA was improved to 95% for blue, 83% for green, and 75% for red. The comparison of the far field emission patterns before and after the addition of the condenser is in Figure 5-19. This configuration shows almost a three times improvement in the light focusing over the bare LED for each color. Hence, we have established a foundation for an ultracompact micro display system, comprising of chip-scale, multi-color collimated light sources using InGaN QW strain engineering and parabolic dielectric lenses. Combining the integrated lens structure with the electrically injected nanopillar LED on chip is future work.

5.4 Summary

We have demonstrated integrable methods of improving the light extraction efficiency and collimating the emitted photons, improving ability to utilize the every photon. Overcoming the light trapping effects due to the material index and structure geometry is a critical piece of the puzzle for creating commercial semiconductor based SPS. With the parabolic reflector and hSIL out coupler, 70% of the photons emitted from the SPS are collected within a conventional 0.5NA angle compared to just 13% without. The 0.5NA zone makes coupling the SPS to a waveguide or fiber easier. With a higher NA system, the collect percentage approaches 87% of the total photons. For the LEDs,

the integrated parabolic lenses improve the PCE across the visible spectrum by 2.7 times to ≥75%. Using conventional fabrication techniques, the lens production process can be made scalable across a wafer-sized area. The significance of this result is that the amount of collimation that can be achieved with an integrated lens highlights the promising future of InGaN based multi-color microdisplays.

Chapter 6

Conclusions and Future Work

6.1 Conclusions

III-nitride QDs offer many promising qualities for practical SPSs. However, closing the speed gap between III-nitride QDs and III-arsenic QDs is critical for their consideration in actual devices. Using silver film cavities, this thesis has demonstrated Purcell factors large enough to close the gap between the two material systems.

State of the art at the beginning of the project

- The shortest lifetime recorded in GaAs QDs is **60ps** due to a lifetime reduction of **~145x** with a photonic crystal cavity [14]. III-nitride QD lifetimes are limited to 10-100 ns due to the QCSE. Limited enhancement is demonstrated with a metallic cavity of less than an order of magnitude, with emitter lifetimes on the order of ~1ns [7].

What I have advanced at the end of this project

- With an open top silver cavity, the effective lifetime for InGaN QDs was reduced to **132ps** bringing III-N QD SPSs within III-arsenic modulation speeds [78]. In addition, our optimized self-aligning silver film cavity has advanced the demonstrable enhancement capabilities of a metallic cavity to above an order of magnitude, with an average (max) Purcell factor of **~46 (135)**, PL intensity enhancement of **~7.3x (59)**, and TRPL lifetime reduction of **~12.8x (23)** [66]. These large enhancement values are favorable for creating homogeneous III-Nitride SPSs for practical applications.

In this thesis, several novel plasmonic cavity and lens and reflector designs have been demonstrated to enhance the optical properties of InGaN emitters across the visible spectrum. The two bullet points show a comparison between published values at the start of this work and our improvements on these values with this work. Only integrated structures designed for device integration are considered, to make a fair comparison to this work. This excludes dimers, nano tips, or other enhancement structures that are not stand-alone with the emitter. In addition, the results are filtered for measurements that account for excitation enhancement or saturation pumping, as this can skew intensity enhancement results, and is accounted for in this thesis. Improvements to the cavity

designs were made for interaction with InGaN QDs to surpass the original enhancement values. The previous limitations of the silver cavity have been surpassed with this work, solving the issue of speed in III-nitride SPSs.

To summarize what was demonstrated in this thesis, first, we demonstrated enhancement of single photon emission using a silver film plasmonic cavity. The cavity design uses the QD pillar structure to shape the cavity. Both the QD lifetime reduction and intensity were enhanced an order of magnitude using this cavity structure, due to coupling with the localized surface plasmon resonance of the structure. Here, an average Purcell factor of 46 was demonstrated. This structure surpassed the documented experimental enhancement from a silver film cavity structure [7] and reduced InGaN QD SPS lifetimes to the order of 1 ns.

Second, we demonstrated overlapping the resonance wavelength of the cavity structure with the emission wavelength of the QD can lead to enhancement of the QD internal QE. With a Purcell factor of 39, which is similar to the first experiment, intensity enhancements up to ~60 times were shown in the cavity structure. A formulism for calculating the QE changes due to the cavity was established and used to predict how homogenous the QDs became in the resonance-matched cavity. This established the groundwork for creating uniform InGaN SPSs through the use of a silver film cavity.

Third, the open top cavity was designed based on a zero-mode waveguide structure. With a small cylinder diameter (25-nm), Purcell factors >1000 were predicted with this structure, reducing the lifetime of the QDs into the picosecond time regime, with our shortest recorded lifetime of 46ps. In addition, the high cavity AQE (>70%), due to the removed top silver in conjunction with the large Purcell factor, allows for homogenization of the QE of an array of QDs within the same cavity geometry. This serves as a foundation for making indistinguishable SPS in wavelength and internal QE, with ultra-short lifetimes comparable to III-arsenic SPSs.

Lastly, using parabolic lenses and reflectors, we demonstrated enhanced photon collection and collimation within 0.5NA. For our SPS, with a parabolic reflector focal length matched to the QD, and a hSIL collimator, we predict a six-fold increase in the number for photons in the 0.5NA zone. Upwards of 90% of all photons generated are sent towards the collection direction. This design eases coupling to waveguide structures for quantum communication devices and significantly reduces the number of lost single photons. Similarly, using parabolic lenses matched to our multi-color LED pixels, there is a 2.7 times improvement in the collimation, with at least >75% of the emission across the visible spectrum into the 0.5NA zone. We also show a method to fabricate these parabolic lenses using a wafer scalable resist reflow and dry etching procedure. These micro lenses

coupled to the multi-color LED are an excellent building block for ultracompact microdisplays.

6.2 Future Work

Based on the research conducted in this thesis, there are future studies that build on the foundations established in this work. A few of the interesting studies for continuation will be explained below.

6.2.1 Alternating Layered Open Top Silver Cavity

In Chapter 4, we proposed an open-top silver cavity with a Purcell factor >1000. Fabrication issues were main limitation in the realization of the cavity structure, as the silver deposition technique most desirable for vertical cylinder coverage, ALD, is still under development. While ALD silver would improve the experimental results of the open top cavity, it would also allow an extension of the cavity idea into a multi-layered structure. With meta materials, alternating dielectric and metal layers allow for LDOS modification. Taking the open top cavity design and inserting dielectric layers in between the silver layers can benefit from the changes in the LDOS to improve the Purcell factor of the system. In addition, the reduction in the metal fill factor improves the cavity AQE

of the system. Moreover, the additional cavity layers act as a multi shell structure, increasing the number of intermediate resonance wavelengths, broadening the width of the main resonance.

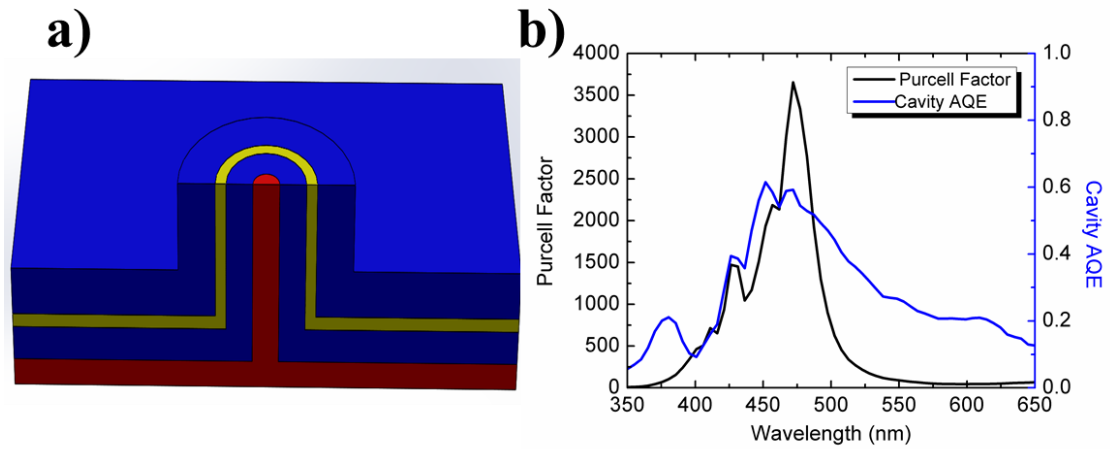

Figure 6-1 (a) 3-D Schematic of the multi-layered open top silver cavity. The GaN nanocylinder is encased in a silver/aluminum oxide/silver layered film with the top section removed from the nanopillar. (b) The Purcell factor and cavity AQE for the cavity structure. The cavity AQE is >50% over the resonance peak bandwidth. A maximum F_p of 3500 is expected, with a FWHM of 50-nm of bandwidth.

The resulting structure produces an ultra-high F_p of 3500 with a resonance FWHM bandwidth of 50-nm. With the developing ALD technology of silver with the existing Al_2O_3 ALD technology in conjunction with our developed silver etch back procedure, this structure could be realized.

6.2.2 Integrated Parabolic Reflector Fabrication

In Chapter 5, we proposed an integrated parabolic reflector and hSIL out coupling lens for our InGaN/GaN QD nanopillar structures. In order to realize this device, the parabolic reflector needs to be index matched and integrated with the nanopillar structure. Taking advantage of rotational angled deposition and the nanopillar natural taper angle, a deposition-mounting angle exists such that the dielectric deposited on the side of the nanopillar could create the desired parabolic shape. The deposition ratio of sidewall to substrate surface versus the nanopillar taper and evaporation chamber mounting angle is shown in Figure 6-2. This assumes that the sample is rotating as well.

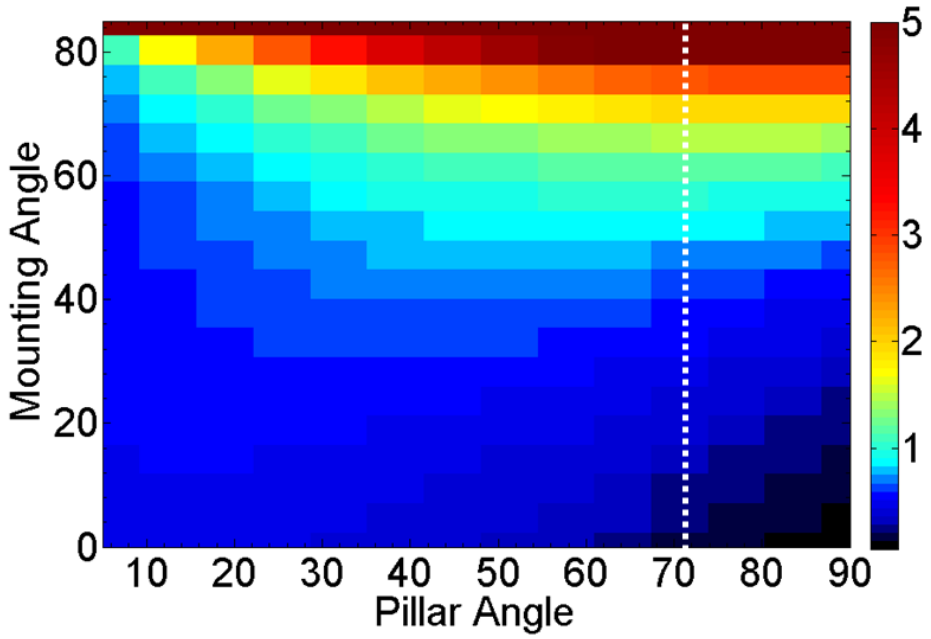

Figure 6-2 The sidewall to substrate deposition ratio for the pillar taper angle versus the sample mounting angle within the evaporation chamber. For our nanopillar taper of 72°,

which is indicated by the dotted white line, mounting angles greater than 70° can achieve deposition ratios greater than 2.

For a 72° nanopillar taper, with mounting angles greater than 70°, we theoretically can achieve deposition ratios greater than 2, which are required to deposit a parabola with a radius of 500-nm and a height of 200-nm. Using TiO_2, which is the closest index matched dielectric material found in our cleanroom that can be e-beam evaporated, angled rotational deposition was employed at a mounting angle of 75° with 1-2 revolutions per second of rotation.

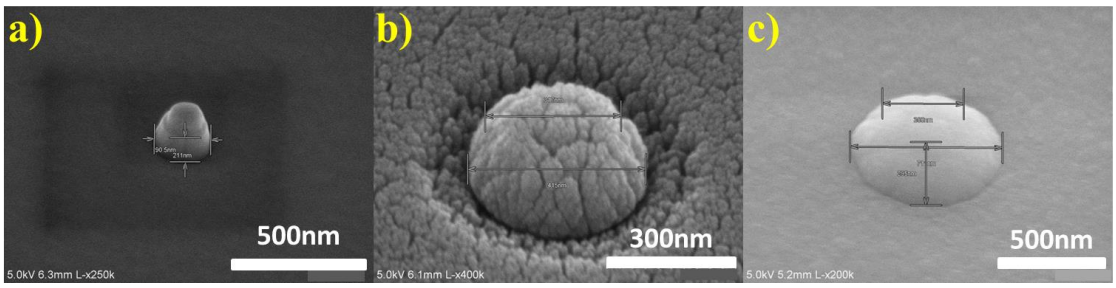

Figure 6-3 SEM images of the parabolic lens integrated with the nanopillar structure. (a) The 211-nm diameter nanopillar structure with Nickel from dry etching still located on top of the pillar. (b) The nanopillar after deposition of 200-nm of TiO_2 using angled rotational deposition with a mounting angle of 75° and 1-2 rps. The TiO_2 base diameter is 415-nm. (c) Post Si_3N_4 PECVD deposition of 400-nm. Nanopillar is located under the curved structure. The diameter of the base is 711-nm.

The nanopillar is covered in TiO_2 film with a high sidewall to top surface coverage

ratio. The diameter of the base is increased to 400-nm. Then, SiN deposition is use to fill the voids from angled deposition and grow the base of the lens structure. After PECVD for 400-nm, the diameter of the base of the lens in the SiN is 711-nm. This process needs to be refined in order to create the parabolic structure surrounding the nanopillar. The TiO_2 sidewall to substrate deposition ratio needs to be increased and the voids in the material reduced. The deposition ratio limit is a material property [102-105], so other dielectrics may need to be investigated to solve this issue. Combined with a resist reflow process for the hSIL lens after substrate thinning, the parabolic reflector, with these improvements to its fabrication would complete the 0.5NA-focused SPS.

Bibliography

[1] A. J. Shields, "Semiconductor quantum light sources," *Nature Photonics,* vol. 1, no. 4, pp. 215-223, Apr 2007.

[2] I. Buluta, S. Ashhab, and F. Nori, "Natural and artificial atoms for quantum computation," (in English), *Reports on Progress in Physics,* Review vol. 74, no. 10, p. 16, Oct 2011, Art. no. 104401.

[3] B. Lounis and W. E. Moerner, "Single photons on demand from a single molecule at room temperature," (in English), *Nature*, Article vol. 407, no. 6803, pp. 491-493, Sep 2000.

[4] X. Brokmann, L. Coolen, M. Dahan, and J. P. Hermier, "Measurement of the radiative and nonradiative decay rates of single CdSe nanocrystals through a controlled modification of their spontaneous emission," *Physical Review Letters,* vol. 93, no. 10, p. 107403, Sep 2004, Art. no. 107403.

[5] M. De Vittorio *et al.*, "Recent advances on single photon sources based on single colloidal nanocrystals," (in English), *Opto-Electronics Review,* Article vol. 18, no. 1, pp. 1-9, Mar 2010.

[6] F. Jelezko and J. Wrachtrup, "Single defect centres in diamond: A review," (in English), *Physica Status Solidi a-Applications and Materials Science,* Review vol. 203, no. 13, pp. 3207-3225, Oct 2006.

[7] J. T. Choy *et al.*, "Enhanced single-photon emission from a diamond-silver aperture," *Nature Photonics*, vol. 5, no. 12, pp. 738-743, Dec 2011.

[8] A. F. Jarjour, R. A. Oliver, and R. A. Taylor, "Nitride-based quantum dots for single photon source applications," (in English), *Physica Status Solidi a-Applications and Materials Science,* Article vol. 206, no. 11, pp. 2510-2523, Nov 2009.

[9] P. Michler *et al.*, "A quantum dot single-photon turnstile device," (in English), *Science,* Article vol. 290, no. 5500, pp. 2282-2285, Dec 2000.

[10] M. J. Holmes, K. Choi, S. Kako, M. Arita, and Y. Arakawa, "Room-Temperature

Triggered Single Photon Emission from a III-Nitride Site-Controlled Nanowire Quantum Dot," (in English), *Nano Letters,* Article vol. 14, no. 2, pp. 982-986, Feb 2014.

[11] S. Kako, C. Santori, K. Hoshino, S. Gotzinger, Y. Yamamoto, and Y. Arakawa, "A gallium-nitride single-photon source operating at 200K," *Nature Materials,* vol. 5, no. 11, pp. 887-892, Nov 2006.

[12] G. Brassard and C. H. Bennett, "QUANTUM CRYPTOGRAPHY," *Lecture Notes in Computer Science,* vol. 325, pp. 79-90, 1988.

[13] V. Rao and S. Hughes, "Single quantum dot spontaneous emission in a finite-size photonic crystal waveguide: Proposal for an efficient "On chip" single photon gun," *Physical Review Letters,* vol. 99, no. 19, p. 193901, Nov 2007, Art. no. 193901.

[14] K. Hennessy *et al.*, "Quantum nature of a strongly coupled single quantum dot-cavity system," (in English), *Nature,* Article vol. 445, no. 7130, pp. 896-899, Feb 2007.

[15] A. Tandaechanurat, S. Ishida, D. Guimard, M. Nomura, S. Iwamoto, and Y. Arakawa, "Lasing oscillation in a three-dimensional photonic crystal nanocavity with a complete bandgap," (in English), *Nature Photonics,* Article vol. 5, no. 2, pp. 91-94, Feb 2011.

[16] A. V. Akimov *et al.*, "Generation of single optical plasmons in metallic nanowires coupled to quantum dots," (in English), *Nature,* Article vol. 450, no. 7168, pp. 402-406, Nov 2007.

[17] K. J. Russell, T. L. Liu, S. Y. Cui, and E. L. Hu, "Large spontaneous emission enhancement in plasmonic nanocavities," (in English), *Nature Photonics,* Article vol. 6, no. 7, pp. 459-462, Jul 2012.

[18] C. E. Hofmann, F. J. G. de Abajo, and H. A. Atwater, "Enhancing the Radiative Rate in III-V Semiconductor Plasmonic Core-Shell Nanowire Resonators," (in English), *Nano Letters,* Article vol. 11, no. 2, pp. 372-376, Feb 2011.

[19] D. J. P. Ellis, A. J. Bennett, S. J. Dewhurst, C. A. Nicoll, D. A. Ritchie, and A. J. Shields, "Cavity-enhanced radiative emission rate in a single-photon-emitting diode operating at 0.5 GHz," (in English), *New Journal of Physics,* Article vol. 10, p. 8, Apr 2008, Art. no. 043035.

[20] K. J. Vahala, "Optical microcavities," (in English), *Nature,* Review vol. 424, no. 6950, pp. 839-846, Aug 2003.

[21] L. Zhang, C. H. Teng, T. A. Hill, L. K. Lee, P. C. Ku, and H. Deng, "Single photon emission from site-controlled InGaN/GaN quantum dots," (in English),

Applied Physics Letters, Article vol. 103, no. 19, p. 5, Nov 2013, Art. no. 192114.

[22] S. Deshpande, T. Frost, A. Hazari, and P. Bhattacharya, "Electrically pumped single-photon emission at room temperature from a single InGaN/GaN quantum dot," *Applied Physics Letters,* vol. 105, no. 14, p. 141109, 2014.

[23] L. Zhang, L. K. Lee, C. H. Teng, T. A. Hill, P. C. Ku, and H. Deng, "How much better are InGaN/GaN nanodisks than quantum wells-Oscillator strength enhancement and changes in optical properties," (in English), *Applied Physics Letters,* Article vol. 104, no. 5, p. 5, Feb 2014, Art. no. 051116.

[24] L. Zhang, T. A. Hill, C.-H. Teng, B. Demory, P.-C. Ku, and H. Deng, "Carrier dynamics in site- and structure-controlled InGaN/GaN quantum dots," *Physical Review B,* vol. 90, no. 24, p. 245311, 12/30/ 2014.

[25] C.-H. Teng, L. Zhang, H. Deng, and P.-C. Ku, "Strain-induced red-green-blue wavelength tuning in InGaN quantum wells," *Applied Physics Letters,* vol. 108, no. 7, p. 071104, 2016.

[26] C.-H. Teng, L. Zhang, T. A. Hill, B. Demory, H. Deng, and P.-C. Ku, "Elliptical quantum dots as on-demand single photons sources with deterministic polarization states," *Applied Physics Letters,* vol. 107, no. 19, p. 191105, 2015.

[27] S. A. Maier and SpringerLink, *Plasmonics: fundamentals and applications* (no. xxiv, 223 p.). New York: Springer, 2007, pp. xxiv, 223 p.

[28] J. J. Mock, M. Barbic, D. R. Smith, D. A. Schultz, and S. Schultz, "Shape effects in plasmon resonance of individual colloidal silver nanoparticles," *Journal of Chemical Physics,* vol. 116, no. 15, pp. 6755-6759, Apr 2002.

[29] J. J. Mock, D. R. Smith, and S. Schultz, "Local refractive index dependence of plasmon resonance spectra from individual nanoparticles," (in English), *Nano Letters,* Article vol. 3, no. 4, pp. 485-491, Apr 2003.

[30] C. Y. A. Ni, S. W. Chang, S. L. Chuang, and P. J. Schuck, "Quality Factor of a Nanobowtie Antenna," (in English), *Journal of Lightwave Technology,* Article vol. 29, no. 20, pp. 3107-3114, Oct 2011.

[31] A. Mohammadi, F. Kaminski, V. Sandoghdar, and M. Agio, "Fluorescence Enhancement with the Optical (Bi-) Conical Antenna," (in English), *Journal of Physical Chemistry C,* Article vol. 114, no. 16, pp. 7372-7377, Apr 2010.

[32] P. Anger, P. Bharadwaj, and L. Novotny, "Enhancement and quenching of single-molecule fluorescence," (in English), *Physical Review Letters,* Article vol. 96, no. 11, p. 4, Mar 2006, Art. no. 113002.

[33] P. Bharadwaj and L. Novotny, "Spectral dependence of single molecule fluorescence enhancement," (in English), *Optics Express,* Article vol. 15, no. 21,

pp. 14266-14274, Oct 2007.

[34] G. W. Lu, T. Y. Zhang, W. Q. Li, L. Hou, J. Liu, and Q. H. Gong, "Single-Molecule Spontaneous Emission in the Vicinity of an Individual Gold Nanorod," (in English), *Journal of Physical Chemistry C,* Article vol. 115, no. 32, pp. 15822-15828, Aug 2011.

[35] G. D. Dice, S. Mujumdar, and A. Y. Elezzabi, "Plasmonically enhanced diffusive and subdiffusive metal nanoparticle-dye random laser," (in English), *Applied Physics Letters,* Article vol. 86, no. 13, p. 3, Mar 2005, Art. no. 131105.

[36] H. Kuwata, H. Tamaru, K. Esumi, and K. Miyano, "Resonant light scattering from metal nanoparticles: Practical analysis beyond Rayleigh approximation," (in English), *Applied Physics Letters,* Article vol. 83, no. 22, pp. 4625-4627, Dec 2003.

[37] C. F. Bohren, D. R. Huffman, and l. Wiley online, "- Absorption and scattering of light by small particles," 1998.

[38] P. Nordlander, "Plasmon hybridization in metallic nanostructures," in *Conference on Plasmonics - Metallic Nanostructures and Their Optical Properties II,* Denver, CO, 2004, vol. 5512, pp. 1-9, BELLINGHAM: Spie-Int Soc Optical Engineering, 2004.

[39] E. Prodan, C. Radloff, N. J. Halas, and P. Nordlander, "A hybridization model for the plasmon response of complex nanostructures," (in English), *Science,* Article vol. 302, no. 5644, pp. 419-422, Oct 2003.

[40] E. M. Purcell, "SPONTANEOUS EMISSION PROBABILITIES AT RADIO FREQUENCIES," *Physical Review,* vol. 69, no. 11-1, pp. 681-681, 1946.

[41] X. M. Lu, M. Rycenga, S. E. Skrabalak, B. Wiley, and Y. N. Xia, "Chemical Synthesis of Novel Plasmonic Nanoparticles," in *Annual Review of Physical Chemistry*, vol. 60(Annual Review of Physical Chemistry, Palo Alto: Annual Reviews, 2009, pp. 167-192.

[42] M. H. Chowdhury, J. Pond, S. K. Gray, and J. R. Lakowicz, "Systematic computational study of the effect of silver nanoparticle dimers on the coupled emission from nearby fluorophores," (in English), *Journal of Physical Chemistry C,* Article vol. 112, no. 30, pp. 11236-11249, Jul 2008.

[43] J. W. Liaw, J. H. Chen, C. S. Chen, and M. K. Kuo, "Purcell effect of nanoshell dimer on single molecule's fluorescence," (in English), *Optics Express,* Article vol. 17, no. 16, pp. 13532-13540, Aug 2009.

[44] E. B. Urena *et al.,* "Excitation Enhancement of a Quantum Dot Coupled to a Plasmonic Antenna," (in English), *Advanced Materials,* Article vol. 24, no. 44, pp.

OP314-+, Nov 2012.

[45] T. H. Taminiau, F. D. Stefani, F. B. Segerink, and N. F. Van Hulst, "Optical antennas direct single-molecule emission," (in English), *Nature Photonics,* Article vol. 2, no. 4, pp. 234-237, Apr 2008.

[46] T. H. Taminiau, F. D. Stefani, and N. F. van Hulst, "Single emitters coupled to plasmonic nano-antennas: angular emission and collection efficiency," (in English), *New Journal of Physics,* Article vol. 10, p. 16, Oct 2008, Art. no. 105005.

[47] S. Kuhn, G. Mori, M. Agio, and V. Sandoghdar, "Modification of single molecule fluorescence close to a nanostructure: radiation pattern, spontaneous emission and quenching," (in English), *Molecular Physics,* Review vol. 106, no. 7, pp. 893-908, 2008.

[48] S. Zhao, K. Wang, F. Chen, D. Wu, and S. Liu, "Lens design of LED searchlight of high brightness and distant spot," (in English), *Journal of the Optical Society of America a-Optics Image Science and Vision,* Article vol. 28, no. 5, pp. 815-820, May 2011.

[49] H. Murat, D. Cuypers, and H. De Smet, "Design of new collection systems for multi LED light engines - art. no. 619604," in *Conference on Photonics in Multimedia*, Strasbourg, FRANCE, 2006, vol. 6196, pp. 19604-19604, BELLINGHAM: Spie-Int Soc Optical Engineering, 2006.

[50] V. Devaraj, J. Baek, Y. Jang, H. Jeong, and D. Lee, "Design for an efficient single photon source based on a single quantum dot embedded in a parabolic solid immersion lens," (in English), *Optics Express,* Article vol. 24, no. 8, pp. 8045-8053, Apr 2016.

[51] M. Gschrey *et al.*, "Highly indistinguishable photons from deterministic quantum-dot microlenses utilizing three-dimensional in situ electron-beam lithography," (in English), *Nature Communications,* Article vol. 6, p. 8, Jul 2015, Art. no. 7662.

[52] S. Tanriseven, P. Maaskant, and B. Corbett, "Broadband quantum dot micro-light-emitting diodes with parabolic sidewalls," (in English), *Applied Physics Letters,* Article vol. 92, no. 12, p. 3, Mar 2008, Art. no. 123501.

[53] P. P. Maaskant *et al.*, "High-Speed Substrate-Emitting Micro-Light-Emitting Diodes for Applications Requiring High Radiance," (in English), *Applied Physics Express,* Article vol. 6, no. 2, p. 3, Feb 2013, Art. no. 022102.

[54] G. S. Kino, "Applications and theory of the solid immersion lens," in *Conference on Optical Pulse and Beam Propagation*, San Jose, Ca, 1999, vol. 3609, pp. 56-66,

BELLINGHAM: Spie-Int Soc Optical Engineering, 1999.

[55] M. A. Nielsen and I. L. Chuang, *Quantum computation and quantum information*. Cambridge university press, 2010.

[56] N. Gisin, G. G. Ribordy, W. Tittel, and H. Zbinden, "Quantum cryptography," (in English), *Reviews of Modern Physics,* Review vol. 74, no. 1, pp. 145-195, Jan 2002.

[57] C. H. Bennett, G. Brassard, and J. M. Robert, "PRIVACY AMPLIFICATION BY PUBLIC DISCUSSION," (in English), *Siam Journal on Computing,* Article vol. 17, no. 2, pp. 210-229, Apr 1988.

[58] S. Buckley, K. Rivoire, and J. Vuckovic, "Engineered quantum dot single-photon sources," (in English), *Reports on Progress in Physics,* Review vol. 75, no. 12, p. 27, Dec 2012, Art. no. 126503.

[59] E. Knill, R. Laflamme, and G. J. Milburn, "A scheme for efficient quantum computation with linear optics," (in English), *Nature,* Article vol. 409, no. 6816, pp. 46-52, Jan 2001.

[60] A. Kiraz, M. Atatüre, and A. Imamoğlu, "Quantum-dot single-photon sources: Prospects for applications in linear optics quantum-information processing," *Physical Review A,* vol. 69, no. 3, p. 032305, 03/10/ 2004.

[61] C. Santori, D. Fattal, J. Vuckovic, G. S. Solomon, and Y. Yamamoto, "Indistinguishable photons from a single-photon device," (in English), *Nature,* Article vol. 419, no. 6907, pp. 594-597, Oct 2002.

[62] D. Englund *et al.*, "Controlling the spontaneous emission rate of single quantum dots in a two-dimensional photonic crystal," (in English), *Physical Review Letters,* Article vol. 95, no. 1, p. 4, Jul 2005, Art. no. 013904.

[63] T. B. Hoang, G. M. Akselrod, C. Argyropoulos, J. Huang, D. R. Smith, and M. H. Mikkelsen, "Ultrafast spontaneous emission source using plasmonic nanoantennas," *Nature communications,* vol. 6, 2015.

[64] P. B. Johnson and R. W. Christy, "OPTICAL CONSTANTS OF NOBLE METALS," *Physical Review B,* vol. 6, no. 12, pp. 4370-4379, 1972.

[65] L. K. Lee and P. C. Ku, "Fabrication of site-controlled InGaN quantum dots using reactive-ion etching," (in English), *Physica Status Solidi C: Current Topics in Solid State Physics, Vol 9, No 3-4,* Proceedings Paper vol. 9, no. 3-4, pp. 609-612, 2012.

[66] B. Demory, T. A. Hill, C.-H. Teng, L. Zhang, H. Deng, and P.-C. Ku, "Plasmonic Enhancement of Single Photon Emission from a Site-Controlled Quantum Dot," *ACS Photonics,* vol. 2, no. 8, pp. 1065-1070, 2015/08/19 2015.

[67] N. F. Yu, A. Belyanin, J. M. Bao, and F. Capasso, "Controlled modification of erbium lifetime by near-field coupling to metallic films," *New Journal of Physics*, vol. 11, Jan 2009, Art. no. 015003.

[68] I. Gontijo, M. Boroditsky, E. Yablonovitch, S. Keller, U. K. Mishra, and S. P. DenBaars, "Coupling of InGaN quantum-well photoluminescence to silver surface plasmons," *Physical Review B*, vol. 60, no. 16, pp. 11564-11567, Oct 1999.

[69] "Lumerical Solutions, Inc. http://www.lumerical.com/tcad-products/fdtd/," ed.

[70] A. Sihvola, "Character of surface plasmons in layered spherical structures," (in English), *Progress in Electromagnetics Research-Pier*, Article vol. 62, pp. 317-331, 2006.

[71] E. Prodan and P. Nordlander, "Structural tunability of the plasmon resonances in metallic nanoshells," (in English), *Nano Letters*, Article vol. 3, no. 4, pp. 543-547, Apr 2003.

[72] C.-H. Teng *et al.*, "Monolithically integrated multi-color InGaN/GaN nanopillar light emitting diodes," in *2015 73rd Annual Device Research Conference (DRC)*, 2015, pp. 161-161: IEEE.

[73] C.-H. Teng *et al.*, "Monolithically integrated multi-color (Blue and Green) light-emitting diode chips," in *2015 Conference on Lasers and Electro-Optics (CLEO)*, 2015, pp. 1-2: IEEE.

[74] P. Kok, W. J. Munro, K. Nemoto, T. C. Ralph, J. P. Dowling, and G. J. Milburn, "Linear optical quantum computing with photonic qubits," (in English), *Reviews of Modern Physics*, Review vol. 79, no. 1, pp. 135-174, Jan-Mar 2007.

[75] J. L. O'Brien, "Optical quantum computing," *Science*, vol. 318, no. 5856, pp. 1567-1570, 2007.

[76] N. Gisin and R. Thew, "Quantum communication," *Nature photonics*, vol. 1, no. 3, pp. 165-171, 2007.

[77] T. Takeuchi *et al.*, "Quantum-confined Stark effect due to piezoelectric fields in GaInN strained quantum wells," *Japanese Journal of Applied Physics*, vol. 36, no. 4A, p. L382, 1997.

[78] B. Demory *et al.*, "Reducing the Dot-to-Dot Variation of InGaN Quantum Dots Using an Open Top Silver Cavity."

[79] M. T. Hill *et al.*, "Lasing in metallic- Coated nanocavities," (in English), *Nature Photonics*, Article vol. 1, no. 10, pp. 589-594, Oct 2007.

[80] M. P. Nezhad *et al.*, "Room-temperature subwavelength metallo-dielectric lasers," (in English), *Nature Photonics*, Article vol. 4, no. 6, pp. 395-399, Jun 2010.

[81] M. J. Levene, J. Korlach, S. W. Turner, M. Foquet, H. G. Craighead, and W. W. Webb, "Zero-mode waveguides for single-molecule analysis at high concentrations," (in English), *Science,* Article vol. 299, no. 5607, pp. 682-686, Jan 2003.

[82] Q. M. Li *et al.,* "Optical performance of top-down fabricated InGaN/GaN nanorod light emitting diode arrays," *Optics Express,* vol. 19, no. 25, pp. 25528-25534, Dec 2011.

[83] D. A. Stocker, E. F. Schubert, and J. M. Redwing, "Crystallographic wet chemical etching of GaN," (in English), *Applied Physics Letters,* Article vol. 73, no. 18, pp. 2654-2656, Nov 1998.

[84] C. Zhang *et al.,* "An Ultrathin, Smooth, and Low-Loss Al-Doped Ag Film and Its Application as a Transparent Electrode in Organic Photovoltaics," *Advanced Materials,* vol. 26, no. 32, pp. 5696-5701, 2014.

[85] D. Gu, C. Zhang, Y.-K. Wu, and L. J. Guo, "Ultrasmooth and thermally stable silver-based thin films with subnanometer roughness by aluminum doping," *ACS nano,* vol. 8, no. 10, pp. 10343-10351, 2014.

[86] D. Zhao, C. Zhang, H. Kim, and L. J. Guo, "High-Performance Ta2O5/Al-Doped Ag Electrode for Resonant Light Harvesting in Efficient Organic Solar Cells," *Advanced Energy Materials,* vol. 5, no. 17, 2015.

[87] S. D. Park, Y. J. Lee, S. G. Kim, H. H. Choe, M. P. Hong, and G. Y. Yeom, "Etch characteristics of silver by inductively coupled fluorine-based plasmas," (in English), *Thin Solid Films,* Article vol. 445, no. 1, pp. 138-143, Nov 2003.

[88] M. Kariniemi *et al.,* "Plasma-enhanced atomic layer deposition of silver thin films," *Chemistry of Materials,* vol. 23, no. 11, pp. 2901-2907, 2011.

[89] E. Matioli *et al.,* "High-brightness polarized light-emitting diodes," (in English), *Light-Science & Applications,* Article vol. 1, p. 7, Aug 2012, Art. no. e22.

[90] W. J. Dong, C. J. Yoo, H. W. Cho, K. B. Kim, M. Kim, and J. L. Lee, "Flexible a-Si:H Solar Cells with Spontaneously Formed Parabolic Nanostructures on a Hexagonal-Pyramid Reflector," (in English), *Small,* Article vol. 11, no. 16, pp. 1947-1953, Apr 2015.

[91] J. J. Wierer, Jr., A. David, and M. M. Megens, "III-nitride photonic-crystal light-emitting diodes with high extraction efficiency," *Nature Photonics,* vol. 3, no. 3, pp. 163-169, Mar 2009.

[92] A. Lundskog *et al.,* "Direct generation of linearly polarized photon emission with designated orientations from site-controlled InGaN quantum dots," (in English), *Light-Science & Applications,* Article vol. 3, p. 7, Jan 2014, Art. no. e139.

[93] D. van Dam *et al.*, "Directional and Polarized Emission from Nanowire Arrays," (in English), *Nano Letters,* Article vol. 15, no. 7, pp. 4557-4563, Jul 2015.

[94] C. P. T. Svensson *et al.*, "Monolithic GaAs/InGaP nanowire light emitting diodes on silicon," (in English), *Nanotechnology,* Article vol. 19, no. 30, p. 6, Jul 2008, Art. no. 305201.

[95] K. Chung, J. Sui, B. Demory, and P.-C. Ku, "Monolithically Integrated Red, Green, and Blue LED Pixels for Micro-Displays," presented at the Microoptics Conference, Berkeley, CA, 2016.

[96] D. T. Schoen, T. Coenen, F. J. G. de Abajo, M. L. Brongersma, and A. Polman, "The Planar Parabolic Optical Antenna," (in English), *Nano Letters,* Article vol. 13, no. 1, pp. 188-193, Jan 2013.

[97] K. A. Serrels *et al.*, "Solid immersion lens applications for nanophotonic devices," (in English), *Journal of Nanophotonics,* Review vol. 2, p. 29, 2008, Art. no. 021854.

[98] D. A. Fletcher *et al.*, "Microfabricated silicon solid immersion lens," (in English), *Journal of Microelectromechanical Systems,* Article vol. 10, no. 3, pp. 450-459, Sep 2001.

[99] Y. K. Ee, R. A. Arif, N. Tansu, P. Kumnorkaew, and J. F. Gilchrist, "Enhancement of light extraction efficiency of InGaN quantum wells light emitting diodes using SiO(2)/polystyrene microlens arrays," (in English), *Applied Physics Letters,* Article vol. 91, no. 22, p. 3, Nov 2007, Art. no. 221107.

[100] A. Schleunitz and H. Schift, "Fabrication of 3D nanoimprint stamps with continuous reliefs using dose-modulated electron beam lithography and thermal reflow," (in English), *Journal of Micromechanics and Microengineering,* Article vol. 20, no. 9, p. 6, Sep 2010, Art. no. 095002.

[101] S. K. Lee, K. C. Lee, and S. S. Lee, "A simple method for microlens fabrication by the modified LIGA process," (in English), *Journal of Micromechanics and Microengineering*, Article vol. 12, no. 3, pp. 334-340, May 2002, Art. no. Pii s0960-1317(02)32920-6.

[102] J. M. Nieuwenhuizen and H. B. Haanstra, "MICROFRACTOGRAPHY OF THIN FILMS," (in English), *Philips Technical Review,* Article vol. 27, no. 3-4, pp. 87-+, 1966.

[103] R. N. Tait, T. Smy, and M. J. Brett, "MODELING AND CHARACTERIZATION OF COLUMNAR GROWTH IN EVAPORATED-FILMS," (in English), *Thin Solid Films,* Article vol. 226, no. 2, pp. 196-201, Apr 1993.

[104] B. Tanto, G. Ten Eyck, and T. M. Lu, "A model for column angle evolution during

oblique angle deposition," (in English), *Journal of Applied Physics*, Article vol. 108, no. 2, p. 3, Jul 2010, Art. no. 026107.

[105] H. Zhu, W. Cao, G. K. Larsen, R. Toole, and Y. P. Zhao, "Tilting angle of nanocolumnar films fabricated by oblique angle deposition," (in English), *Journal of Vacuum Science & Technology B*, Article vol. 30, no. 3, p. 4, May-Jun 2012, Art. no. 030606.